

Local electronic properties and adsorption conformations of molecular nanostructures at surfaces

THÈSE N° 6748 (2015)

PRÉSENTÉE LE 25 AOÛT 2015

À LA FACULTÉ DES SCIENCES DE BASE
LABORATOIRE DE SCIENCE À L'ÉCHELLE NANOMÉTRIQUE
PROGRAMME DOCTORAL EN PHYSIQUE

ÉCOLE POLYTECHNIQUE FÉDÉRALE DE LAUSANNE

POUR L'OBTENTION DU GRADE DE DOCTEUR ÈS SCIENCES

PAR

Ivan PENTEGOV

acceptée sur proposition du jury:

Prof. C. Hébert, présidente du jury
Prof. K. Kern, directeur de thèse
Prof. J.-F. Lutz, rapporteur
Prof. P. Wahl, rapporteur
Prof. J.-Ph. Ansermet, rapporteur



ÉCOLE POLYTECHNIQUE
FÉDÉRALE DE LAUSANNE

Suisse
2015

An experiment is a question which science poses to Nature,
and a measurement is the recording of Nature's answer.

— Max Planck

To my family...

Abstract

Nanoscale science is an emerging field of our time and opens a broad horizon for applications in almost every area of human activity, from medicine to energy storage. As usual, there are numerous challenges in the way of progress, which slow down the development and application of new ideas. Therefore the versatile investigation of nanostructures is of current importance for the realization of future technologies.

The central aim of this thesis was to advance the field of molecular nanoscience on several crucial fronts. For that, the scanning tunneling microscopy (STM) was chosen as the principal experimental technique. It provides an unprecedented resolution at the atomic scale and can be used to reveal topographical or electronic properties of single molecules or atoms on conducting surfaces. Moreover, it gives a certain freedom to manipulate the object of interest at the nanoscale by the apex of the scanning tip.

The introduction to this thesis gives a brief overview about the history of nanotechnology and its current status. In the first chapter the theory of the tunneling effect and the working principle of the STM are presented and the experimental set-up is described. The second chapter is devoted to shot noise measurements with the STM. At first, the theory of shot noise is presented from the view point of the scattering approach. The challenges that arise on the way towards noise detection are discussed from two different sides: current and voltage amplification. Several test measurements are suggested for the approval of the amplification circuitry. Afterwards, the data obtained on the copper and gold quantum point contact are shown.

The third chapter presents an investigation of a purely organic radical with spin system $1/2$ by means of STM. This molecule was previously studied on the Au(111) surface in the work of Steffen Kahle and Young-Hui Zhang [1]. In this thesis, its adsorption on Pd(111) and cobalt islands on Cu(111) is explored. The obtained data reveals electronic transport where molecular orbitals and vibration excitations are involved.

The final chapter presents an STM investigation of the sequence controlled polymers - the oligo-triazole amide trimers, which were successfully deposited on the Cu(100) surface by

means of the electrospray ion-beam deposition technique. The molecules show a large variety of adsorption conformations which are correlated with the sequence of monomers in the molecular backbone. Each chapter contains a summary and outlook, where possible improvements are discussed and future experiments suggested.

Key words : *Scanning tunneling microscopy, shot noise, quantum point contact, organic nanostructures, magnetic impurities, Kondo effect, sequence controlled polymers, electrospray ion-beam deposition.*

Résumé

La nanoscience qui représente la science à l'échelle nanométrique est un domaine de recherche actuellement en plein extension. Elle ouvre un large horizon d'applications dans presque toutes les activités de développement allant de la médecine au stockage d'énergie. Mais, comme dans tous les domaines, il y a des difficultés qui surgissent ralentissant le progrès et l'application des nouvelles idées. Ainsi, l'étude précise des nanostructures est actuellement très importante pour l'accomplissement des futures applications technologiques.

L'objectif fondamental de cette thèse de doctorat est la recherche scientifique dans la nanotechnologie moléculaire. Dans cette thèse la microscopie à effet tunnel (STM de l'anglais Scanning Tunneling Microscopy) a été choisie comme technique expérimentale principale. Ce microscope a une résolution atomique et peut être utilisé pour mettre en évidence les propriétés topographiques et électroniques d'une seule molécule ou un seul atome déposé sur une surface supportrice. En outre, il offre la possibilité d'étudier l'objet nanométrique et de contrôler ces propriétés.

L'introduction de ce manuscrit raconte brièvement l'histoire de la nanotechnologie jusqu'à son état actuel. Dans le premier chapitre sont présentés la théorie de l'effet tunnel, le principe de fonctionnement du STM et l'équipement expérimental. Le deuxième chapitre est consacré aux mesures du bruit électronique appelé « shot noise » par le STM. Dans un premier temps, la théorie de bruit est présentée dans le cadre de la diffusion électronique. Les difficultés de détection du bruit sont discutées à partir de deux points de vue différents : l'amplification du courant et l'amplification de la tension. Plusieurs mesures tests sont proposées pour obtenir une amplification escomptée dans le circuit. Ensuite, sont présentées les données obtenues en contact de point quantique sur le cuivre et l'or.

Le troisième chapitre présente l'étude effectuée sur un radical organique pur de spin 1/2. Cette molécule, qui a été déjà étudié au préalable sur une surface de Au(111) par Steffen Kahle et Young-Hui Zhang [1], est étudié ici sur les surfaces de Pd(111) et de Co/Cu(111). Les résultats obtenus montre la complexité du transport électronique dans ces systèmes, vue la complexité de la structure des orbitales moléculaires et les excitations vibrationnelles correspondantes. Le

dernier chapitre décrit l'étude des polymères à séquence contrôlée, notamment les trimères de oligo-triazole amide. Ces derniers ont été déposés avec succès sur la surface de Cu(100) par la technique de dépôt par faisceau d'ions électrospray. Les molécules présentent une diversité de possibilités de conformation d'adsorption qui sont en relation avec la séquence des monomères dans le squelette moléculaire. Chaque chapitre contient un résumé et aussi les perspectives, où des possibles améliorations et futures expériences sont suggérées.

Zusammenfassung

Nanowissenschaften ist ein aufkommendes Feld in unserer Zeit, welches in fast jedem Bereich menschlicher Aktivität Anwendung findet - von Medizin hinzu Energiespeicherung. Wie üblich gibt es gewisse Herausforderungen auf dem Weg des Fortschritts, welche die Entwicklung und Anwendung neuer Ideen verlangsamt. Diesbezüglich ist die heutige, vielseitige Untersuchung von Nanostrukturen sehr bedeutend um zukünftige Technologien zu ermöglichen.

Das Hauptziel dieser Arbeit war es die Nanowissenschaften auf mehreren wichtigen Ebenen voranzubringen. Dazu wurde das Rastertunnelelektronenmikroskop (RTM) als vorrangige experimentelle Technik verwendet. Diese Technik ermöglicht beispiellose Auflösung auf der atomaren Skala und kann dazu benutzt werden, topographische und elektronische Eigenschaften von Einzelmolekülen oder -atomen auf der Oberfläche aufzulösen. Darüberhinaus ermöglicht das RTM gezielt Objekte auf der Nanoskala durch den Apex der Spitze zu manipulieren.

Die Einführung dieser Arbeit erzählt in Kürze die Geschichte der Nanotechnologie und den aktuellen Status. Im ersten Kapitel wird die Theorie des Tunneleffektes, das Arbeitsprinzip des RTMs und der experimentelle Aufbau beschrieben. Das zweite Kapitel ist den Schrotrauschmessungen im RTM gewidmet. Als erstes wird die Theorie des Schrotrauschen mit Hilfe des Streuungsansatz vorgestellt. Die Herausforderungen, welche auf dem Weg der Rauschmessung auftauchen, werden von zwei verschiedenen Seiten diskutiert: Strom- und Spannungsverstärkung. Verschiedene Testmessungen werden für die Annahme der Verstärkung des Stromkreises vorgeschlagen. Im Anschluss werden die Daten, welche auf Kupfer und Gold Quantenpunktkontakten aufgenommen wurden, gezeigt.

Das dritte Kapitel zeigt die Untersuchung, welche an reinen organischen Radikalen mit Spin $1/2$ vorgenommen wurde. Dieses Molekül wurde bereits auf der Au(111) Oberfläche in den Doktorarbeiten von Steffen Kahle und Yong-Hui Zhang [1] untersucht. In dieser Arbeit wird die Adsorption auf der Pd(111) Oberfläche und auf Kobaltinseln auf Cu(111) erforscht. Die erhaltenen Daten zeigen einen elektronischen Transport bei dem die Molekülorbitale oder Vibrationsanregungen eine Rolle spielen.

Das letzte Kapitel handelt von den sequenzkontrollierten Polymeren - den Oligo-Triazole Amide Trimeren, welche erfolgreich auf der Cu(100) Oberfläche durch Elektronenspray Ionenstrahldeposition aufgebracht wurden. Die Moleküle zeigen große Unterschiede in den Adsorptionsgeometrien welche mit den Sequenzen der Monomere im molekularen Hauptstrang korreliert sind. Jedes Kapitel beinhaltet eine Zusammenfassung und einen Ausblick, welcher mögliche Verbesserungen und zukünftige Experimente diskutiert.

Stichwörter : *Rastertunnelmikroskopie, Schrotrauschen, Quantenpunktkontakt, organische Nanostrukturen, Kondo Effekt, Polymerforschung.*

Contents

Abstract (English/Français/Deutsch)	1
List of figures	9
List of abbreviations	11
Introduction	13
1 Experimental and theoretical foundations	19
1.1 Scanning tunneling microscopy	19
1.1.1 History	19
1.1.2 Theory of the tunneling effect	20
1.1.3 Working principle	22
1.1.4 Scanning tunneling spectroscopy	22
1.2 Experimental Set-up	24
2 Quantum noise	27
2.1 Introduction	27
2.2 Theoretical background	29
2.3 Results	34
2.3.1 Test measurements of thermal noise on a resistor using a current amplifier	34
2.3.2 Test measurements of shot noise on a diode using a current amplifier . .	37
2.3.3 Thermal noise amplification combined with the STM electronics	38
2.3.4 Shot noise measurement in a weak tunneling regime with the STM by current amplification	40
2.3.5 Test measurement of thermal noise on a resistor using a voltage amplifier	42
2.3.6 Shot noise measurement at a quantum point contact with the STM by voltage amplification	43
2.4 Conclusions	46
2.4.1 Discussion of the results	46
2.4.2 Design of the new STM Head	49

Contents

3	Pure organic molecule with spin system 1/2	51
3.1	Introduction	51
3.2	Theoretical background	52
3.2.1	Kondo model	52
3.2.2	Signatures of the Kondo effect in scanning tunneling spectroscopy	54
3.2.3	Overview / Motivation	55
3.3	Results	56
3.3.1	Experimental approach / Sample preparation	56
3.3.2	NMTD on Pd(111)	56
3.3.3	NMTD on Co Islands on Cu(111)	58
3.4	Conclusions	64
3.4.1	Discussion of the results	64
3.4.2	Outlook: NMTD chains on Cu(111)	66
4	STM imaging of sequence controlled polymers	69
4.1	Introduction	69
4.2	Background	70
4.2.1	Oligo triazole amides (OTA)	70
4.2.2	Electrospray ion beam deposition	70
4.3	Results and discussion	73
4.3.1	Mass spectrometry of OTA trimers	73
4.3.2	STM topography of OTA trimers	74
4.3.3	Analysis of the STM topographies	76
4.4	Conclusions	80
4.4.1	Summary	80
4.4.2	Outlook: OTA hexamers	82
5	Summary and perspectives	87
5.1	Quantum noise	87
5.2	Organic molecule with spin system 1/2: probing of quantum criticality	88
5.3	Sequence controlled polymers: the way towards molecular logic	89
	Bibliography	98
	Acknowledgments	99
	Curriculum Vitae	101

List of Figures

1.1	Schematic illustration of the tunneling effect	21
1.2	STM working principle	22
1.3	CAD drawing of the low temperature ultra high vacuum STM	25
2.1	Schematic representation of a ballistic conductor	30
2.2	Quantum noise spectral density according to the Landauer-Buttiker formalism	35
2.3	Thermal noise measurements on a metal film resistor	36
2.4	Shot noise measurement on a diode	38
2.5	Set-up of noise measurement combined with STM circuit	39
2.6	Test measurement of thermal noise within the STM	40
2.7	Current dependence on the tip-sample distance for Cu(111) quantum point contact	41
2.8	A single Cu atom on Cu(111) surface	41
2.9	Shot noise measurement in weak tunneling regime on Cu(111)	42
2.10	Shot noise measurement in weak tunneling regime on Cu(111) after background correction	43
2.11	Thermal noise measurements on a metal film resistor by cross-correlated voltage amplification	44
2.12	Comparison of a single channel noise measurement from one amplifier and cross-correlation mode with two amplifiers in parallel	44
2.13	Set-up of noise measurement combined with STM circuit through the switch mechanism	45
2.14	Voltage divider with an external controller	45
2.15	Shot noise spectra recorded on a gold quantum point contact by voltage amplification	47
2.16	Comparison of the experimental data with the corresponding theory for a gold quantum point contact	47
2.17	Transfer function of the STM insert	48
2.18	Admittance measurement through the STM	49
2.19	CAD drawing of the new STM-Head	50

List of Figures

3.1	Different regimes of the Kondo effect	53
3.2	Kondo resonance appearance in STS	55
3.3	Chemical structure of the NMTD molecule	57
3.4	Constant current STM topography for NMTD on Pd(111)	58
3.5	Different adsorption conformations of NMTD. Constant current STM topography and typical dI/dV spectra	59
3.6	Profile comparison of different adsorption conformations	60
3.7	dI/dV spectra taken on the two molecules in ± 50 mV range	60
3.8	Spectra from the dI/dV map on a NMTD molecule	61
3.9	Intensity distribution of the central and left Lorentzian from the dI/dV map	61
3.10	Cobalt islands on Cu(111). Constant current STM topography and typical dI/dV spectra	62
3.11	NMTD molecules on cobalt islands on Cu(111). STM topography and dI/dV spectra	63
3.12	dI/dV spectra in the range of ± 300 mV	63
3.13	Estimation of the Pd(111) workfunction	64
3.14	Energy levels comparison for Pd(111) surface and NMTD molecule in vacuum	65
3.15	dI/dV spectra on similar molecules from other references	67
3.16	Chains of the NMTD molecule on Cu(111)	67
4.1	Chemical structure of the oligotriazole amide (OTA) trimers	71
4.2	Schematic of the electrospray ion beam deposition apparatus	73
4.3	Mass spectrometry of the three OTA oligomers	74
4.4	STM constant current topography of the «011» oligomer deposited on Cu(100)	75
4.5	STM topography of the «111» oligomer	75
4.6	Second conformation of the three oligomers	76
4.7	Manipulation of the oligomer by the STM tip	77
4.8	Axis definition through an oligomer of the second conformation	77
4.9	Analysis of the STM data 1	78
4.10	Analysis of the STM data 2	79
4.11	Possible lamellae types of OTA folding	81
4.12	A chain of polyethylene-like polymer before and after crystallization from Ref. [2]	82
4.13	Chemical formula of a hexamer and its possible vacuum conformation	83
4.14	Time-of-Flight mass spectrum of the hexamer	83
4.15	STM constant current topography of the hexamer	84
4.16	STM topography of OTA, scanning with a functionalized tip	85
5.1	Schematic phase diagram for the two impurity Kondo system	88

List of abbreviations

AC	Alternating Current
AFM	Antiferromagnetic
DC	Direct Current
DFT	Density Functional Theory
ES-IBD	Electrospray Ion Beam Deposition
FFT	Fast Fourier Transform
FM	Ferromagnetic
HOMO	Highest Occupied Molecular Orbital
HV	High Vacuum
WHM	Half Width at Half Maximum
LUMO	Lowest Occupied Molecular Orbital
LDOS	Local Density of States
MS	Mass Spectrometry
NMTD	2'-Nitronitroxide-5'-Methyl-[1,1';4,1'']Terphenyl-4,4'- Dicarbonitrile
OTA	Oligotriazole Amides
QPC	Quantum Point Contact
RF	Radio Frequency
SCP	Sequence Controlled Polymers
SOMO	Singly Occupied Molecular Orbital
STM	Scanning Tunneling Microscopy
STS	Scanning Tunneling Spectroscopy
TOF	Time-of-flight
UHV	Ultra High Vacuum

Introduction

"When we get to the very, very small world – say circuits of seven atoms – we have a lot of new things that would happen that represent completely new opportunities" - this statement, made by Richard Feynman in 1959 during his lecture at the CalTech, is usually considered as the commencement of nanotechnology. [3] Nowadays, after more than 50 years of history, nanotechnology is a rapidly progressing field that unites the main natural sciences: physics, chemistry and biology. The original idea of connecting two expressions: "nano" and "technology" was introduced by Norio Taniguchi from the Tokyo University of Science. [4] With this new term, he described a processing method based on ion sputtering for the design of nanometer-size semiconductor structures. However, later it became clear that standard semiconductor technologies will meet certain limitations at the nanoscale and one has to search for a new basis of electronics. The recent complementary metal–oxide–semiconductor (CMOS) technology reached a minimum half-pitch of 20 nm (a single pitch corresponds approximately to the distance between two different elements in a memory array). The international technology roadmap for semiconductors (ITRS) describes this achievement as a possible end point in the scaling down of the chip processing technology. Further decrease seems to be impossible due to the certain fundamental reasons, as, for instance, the tunneling effect that can occur between source and drain of a transistor and results in a leakage current. In addition, the performance of semiconductor devices usually suffers from many factors such as varying temperature or external ionizing radiation.

In 1974, Arieh Aviram and Mark Ratner suggested the use of a single molecule as an electronic device, a rectifier. [5] This gave birth to the emerging field of molecular electronics. More than two decades passed until the first successful measurements of charge transport through a single molecule were conducted in a mechanically controlled break junction [6] and STM [7]. At the same time, Eric Drexler developed the concept of molecular nanoengineering [8] and proposed a great future of molecular machines, in his words "power-driven mechanical systems" at the nanoscale.

The main goal of nanotechnology, to some extent, is close to fulfilling the dream of medieval alchemists: be able to design new materials with necessary properties. The national nanotech-

Introduction

nology initiative (NNI), founded by the US government in 2000 with the focus on the nanoscale research and development aims to achieve "the future in which the ability to understand and control matter at the nanoscale leads to a revolution in technology and industry that benefits society". [9]

The fabrication of nanostructures is a complicated procedure and can be carried out by many different methods. Usually, one distinguishes between two main directions: the top-down and the bottom-up approaches. The first is based on lithography patterning and mechanical printing techniques and allows one to create sub-micro structures from macroscopic wafers. The big advantage of the top-down is its convenience for large scale production: once created, the stamp can be used many times for patterning. However, the industrial lithography techniques have reached a resolution plateau of 10 nm and further decrease seems to be rather difficult. The obstacle here is not only the Rayleigh limit, but also the resist polymer, whose size can not be reduced to arbitrary small dimensions. In contrast, the bottom-up approach utilizes the idea of using single atoms and molecules as "LEGO" bricks for construction of complicated assemblies. This way is, to some extent, inspired by nature - processes such as self-assembly and self-organization are known to be responsible for the creation of ordered supramolecular structures at the nanoscale. The bottom-up approach incorporates a large number of methods from chemical vapor deposition (CVD) to supercritical fluid synthesis. However, the only one technique up to now, which successfully fulfills the description of the "Feynman machine" [10] - the instrument that can allow selective controlling and manipulation of single atoms or molecules - is the scanning probe microscopy.

Ideally, the new molecular approach in electronics would not only lower the dimensions of circuitry, but also increase the performance of microprocessors. At present, there is a large zoo of promising experimental data that demonstrates constitutive future applications of single molecules: from quantum magnets [11] to single-molecule optical transistors [12, 13]. Even DNA molecules were proved to be a potential basis for carrying out functions of a logic gate. Several years ago, Park et al. [14] were first to demonstrate a logic operator on the basis of the DNA replication as an output signal. They synthesized the DNA primers with a certain mismatch in sequence, so that their replication by the polymerase enzyme became possible only in the presence of the certain metal ions. However, there is still no large-scale integration method, that will allow to pass the output signal from one DNA logic operator to the input of another one. Besides these developments, a substantial progress was achieved towards realization of nonvolatile memory, based on molecular switches - organic compounds that can be reversibly driven in two or even more stable states. [15] The switching occurs between different conformations, charge or even spin states and can be enforced by external stimuli, such as a voltage pulse, temperature gradient or light excitation. [16] Jumping from one state into the other (from "0" into "1"), the molecule changes its electrical or optical properties that

can be read out by various methods. Single molecule memory is just a first step in the field of molecular logic. This emerging topic has as its aim the creation of molecular circuits that will enable multiple-valued boolean operations within organic compounds. Recently, Borghetti et al. [17] showed a possibility of "NAND" logic operator, based on molecular memristors - molecules, that possess two stable states with low and high resistance as a function of voltage applied.

The theoretical methods for calculations of electronic transport through single molecules, such as the non equilibrium Green's function techniques, are also advancing rapidly and deliver good agreement with experimental results. [18] However, despite all of these scientific achievements, the conversion from the semiconductor to molecular technology is still not realized on the industrial scale - the nanotechnology "boom" is postponed year after year. This is also apparent in funding volumes provided by the governmental agencies on "nano" topics [9], which have not increased drastically, as it was the case in the early 2000's.

The application of molecular electronics faces many challenges that hinder the mass development of organic circuits. The most complicated among these are the reliable synthesis of complex structures with sufficient robustness, and the deep understanding of the interface between organic molecule and metal electrodes. [19] Furthermore, there is still a great need for fabrication methods that give reproducible contact formation. [20, 21] Hence, exploring the coupling between single molecules and metal electrodes has a crucial importance for the future electronic components. The solution to these problems can be approached from many different perspectives.

The goal of this thesis is to advance molecular nanoscience at several crucial fronts by scanning tunneling microscopy (STM). The low temperature STM was selected as the main experimental approach, since it is a perfect instrument for visualizing the spatial configuration of organic adsorbates on metallic surfaces. Moreover, it allows one to probe the electronic properties or even manipulate the molecule of interest. This technique is introduced in the beginning of the thesis, where the experimental set-up is also described. Although the spatial resolution of the STM has reached the atomic limit, new challenges are rising towards achieving high time-scale resolution. The frequency-dependent component of the tunneling current signal can provide significant information on many intricate physical phenomena, such as electron spin relaxation times [22, 23], statistics of quasiparticles [24] or correlation effects [25]. In order to extract the necessary data one has to look carefully at the noise intensity, since it is in close relation with the mentioned processes.

The second chapter presents a study on quantum shot noise and discusses the possibility of its implementation in an STM. The motivation behind this is the understanding of conductance channel formation in a molecular-metal junction. Being caught between metallic electrodes,

Introduction

a single molecule behaves like a ballistic conductor. According to the Landauer theory [26], transport through this junction occurs via established transmission channels, whose composition cannot be evaluated by a simple I/V characteristic. It was earlier proven that the shot noise measurement can provide insight into the transmission channel composition of a ballistic conductor. [27] This is possible because the shot noise spectral density S at a quantum point contact is directly coupled to the combination of these channels τ_n [28]:

$$S_I \sim 2e \sum_{n=1}^N \tau_n(1 - \tau_n) \quad (1)$$

Moreover, if the transport is performed through a molecular radical with an unpaired electron, the arising Kondo effect can lead to the two-particle scattering processes. The latter phenomenon can be revealed by the shot noise measurement, since its spectral density is also dependent on the charge transferred at a single tunneling event. The STM technique, when upgraded with a shot noise detection, should allow one to understand the basic principles of the metal-molecular junction conductance. The main obstacles that occur on the way towards shot noise and STM complementation, and possible methods for their solution are discussed thoroughly in this thesis.

The third chapter is devoted to the interaction of a single organic radical with the Fermi sea of electrons in magnetic metals. The latter phenomenon called the Kondo effect is essential for molecular spintronics, especially concerning its application in integrated circuits, where a molecular magnet is brought in contact to the metallic leads. The experimental data demonstrate intricate transport behavior, when the molecular orbital can be split due to the Coulomb interaction, and the Kondo resonance varies its form because of different coupling between the molecular radical and the surface.

The fourth chapter is dedicated to sequence controlled polymers (SCP). They were recently proposed as the new "holy grail" of the polymer science [29] due to their possible application in data storage or as a new type of highly organized materials. In this thesis, the SCP's adsorption conformations on metal surfaces were investigated by means of low temperature STM. The oligo triazole amide (OTA) trimers were chosen as typical representatives of the SCP, synthesized on the basis of two different monomers. We examined the possibility of depositing the OTAs in ultra high vacuum via electrospray ion-beam deposition technique. After adsorption on a metal surface, the correlation between the secondary structure and polymer chain folding was investigated.

Since this thesis covers several domains of nanoscience, each chapter provides a specific introduction to the corresponding area of research, complemented by a brief theory overview. The theoretical background of shot noise in terms of the scattering approach and a description

of the Kondo effect are provided in the beginning of the second and third chapters respectively. In summary, the work presented in this thesis shows that atomic scale insight as given by high resolution method like STM, is one of the best approaches towards answering the pressing challenges of nanotechnology.

1 Experimental and theoretical foundations

1.1 Scanning tunneling microscopy

1.1.1 History

The history of Scanning Tunneling microscopy goes back to the end of the 60's. At that time, three scientists: Young, Ward and Scire had a pioneering idea of using the tunneling effect in metal-vacuum-metal junctions for exploring the microstructure of surfaces. Later, they built a set-up called "Topographier" in the National Bureau of Standards (NIST). [30] Its resolution reached 3 nm in the direction perpendicular to the surface and at least 400 nm out of plane. The scanning was performed at the distance of 5 nm to the sample, in the regime, which is more close to the field emission rather than tunneling effect. Apart from that, certain difficulties, as for example bad vibration isolation, prohibited examination of surfaces at the nanoscale.

Gerd Binnig and Heinrich Rohrer in the early 80's constructed a similar set-up at the IBM lab in Zurich, which allowed more precise investigation of surface structure. [31] They demonstrated its promising trend with a publication of the atomic resolved 7x7 restructure of Si(111) surface, being a "holy grail" of surface science at that time. [32] In 1986 for the invention of the Scanning Tunneling Microscopy (STM) they were awarded the Nobel Prize in physics.

However, the first STM was thought to be just an imaging instrument, without a possibility to control or manipulate individual objects on the surface. Later, in 1989, Don Eigler and colleagues were the first to demonstrate the powerful application of the STM as the so called "Feynman machine", [33] moving single Xenon atoms on the Nickel surface with an STM tip. [34] For that, they cooled the STM chamber down to 4 K with liquid Helium, what dramatically increased the stability of the microscope and reduced the contamination of the surface by

residual gases.

Nowadays, after more than two decades since its first demonstration, the low-temperature STM is proven to be a perfect tool for nanoscale research and engineering. Large zoo of advanced scanning probe techniques were developed on the STM basis. Their spatial resolution has almost reached its limit, going down to sub-atomic contrast, provided by the non-contact Atomic Force Microscopy. [35] However, new challenges arise on the way towards time-scale examination, where single spin dynamics [22] or statistics of quasiparticles [36],[37] could be explored.

1.1.2 Theory of the tunneling effect

The tunneling effect is a pure phenomenon of quantum mechanics. In classical physics, spatial coordinates of a particle and its momentum can be evaluated with an arbitrary precision. Moreover, a particle with energy E being situated in a potential field U can occupy only those space coordinate \vec{r} , where $E(\vec{r}) > U(\vec{r})$.

Contrary to that, in quantum mechanics, the exact position of a free particle and its momentum cannot be obtained simultaneously according to the Heisenberg uncertainty principle ($\Delta p \Delta x \sim \hbar$). The system is described via plane wave: $\psi(\vec{r}, t) \sim \exp i(k\vec{r} - \omega t)$. It determines the probability density $\rho = |\psi(\vec{r}, t)|^2$ for the particle to be at the coordinate \vec{r} at time t . The plane waves are solution of the Schrödinger equation [38]:

$$i\hbar \frac{\delta \psi(\vec{r})}{\delta t} = -\frac{\hbar^2}{2m} \nabla^2 \psi + U(\vec{r}, t) \psi(\vec{r}, t) \quad (1.1)$$

where \vec{r} is the coordinate, $U(\vec{r}, t)$ - the potential field, m - mass of the particle. For explaining the tunneling effect one can consider a one dimensional case and finite-height potential barrier. Then, the Schrödinger equation takes its simplified time-independent form:

$$E\psi(x) = -\frac{\hbar^2}{2m} \frac{d^2 \psi}{dx^2} + U(x)\psi(x) \quad (1.2)$$

with E being the energy of the particle.

For the classically forbidden case of $E < U$, the wave function shows an exponential decay inside the barrier region: $\psi \sim \exp(ikx)$, where k is defined as $k = \sqrt{\frac{2m}{\hbar^2}(E - U)}$. Hence, the

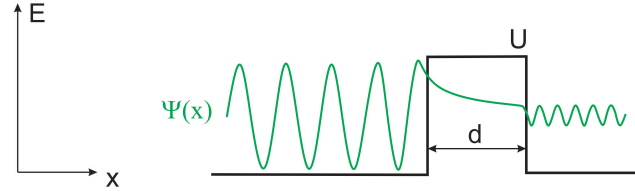


Figure 1.1 – Schematic illustration of the tunneling effect

probability for the particle to pass a potential barrier of depth d is not equal to zero:

$$\rho \sim |\psi(x = d)|^2 \sim \exp -2kd = \exp \left\{ -\frac{2}{\hbar} \sqrt{2m(U - E)d} \right\} \quad (1.3)$$

In the case of STM, the scanning tip is brought close to the sample surface at a distance of several nanometers. The effective height of the tunneling barrier can be calculated as an average of the tip and sample workfunction:

$$\Phi^* = \frac{1}{2}(\Phi_{Sample} + \Phi_{Tip}) \quad (1.4)$$

After applying a bias voltage V , electrons near the Fermi energy start to tunnel through the vacuum. For the barrier, established between two metal electrodes, the tunneling current density in the one-dimensional case was first calculated by J.G. Simons [39]:

$$J_{Tunnel} = J_0 [\Phi^* \exp(-A\sqrt{\Phi^*} d) - (\Phi^* + eV) \exp(-A\sqrt{\Phi^* + eV} d)] \quad (1.5)$$

where A and j_0 are parameters, described as:

$$J_0 = \frac{e}{4\pi^2 \hbar d^2}, \quad A = \frac{2}{\hbar} \sqrt{2m} \quad (1.6)$$

For low bias voltages ($eV < \Phi^*$) the equation 1.5 can be reduced to:

$$J_{Tunnel} = J_0 \frac{A\sqrt{\Phi^*} eVd}{2} \exp(-A\sqrt{\Phi^*} d) = \frac{e^2 \sqrt{2m\Phi^*}}{4\pi^2 \hbar^2} \frac{V}{d} \exp \left\{ -\frac{2}{\hbar} \sqrt{2m\Phi^*} d \right\} \quad (1.7)$$

Since the exponential dependence on the barrier thickness d is the dominating one, quiet often a simplified approximation $J_{Tunnel} \sim \exp \left\{ -\frac{2}{\hbar} \sqrt{2m\Phi^*} d \right\}$ is used for qualitative evaluations.

Chapter 1. Experimental and theoretical foundations

A real junction between tip and sample in the STM is not one-dimensional and has usually a complicated geometry. However, the exponential decay of the tunneling current with the simultaneous increase of the tip-sample distance is always a pronounced feature and was confirmed by many experiments on various systems.

1.1.3 Working principle

A scanning tunneling microscope is based on the electromechanical system with negative feedback. The feedback loop keeps the tunneling current (and hence, the tip-sample distance) stable at a certain set-point value. This is realized through changing the tip position in vertical direction by z-piezoelectrode (Figure 1.2) Due to the fact that the current value has exponential dependence on the tunnel barrier height, the STM technique allows precise depiction of the sample surface with a sub-angstrom resolution.

Generally, the surface topography can be obtained by two different methods: constant current or constant height scanning. In the former one the tip position is changed in order to keep the current stable and the signal of the z-piezo electrode in feedback line is recorded. For the constant height scanning the vertical position of the tip is set constant by switching the feedback off and the tunneling current is obtained.

The lateral resolution is realized by moving the tip in plane over the region of interest, like it is shown in Figure 1.2.

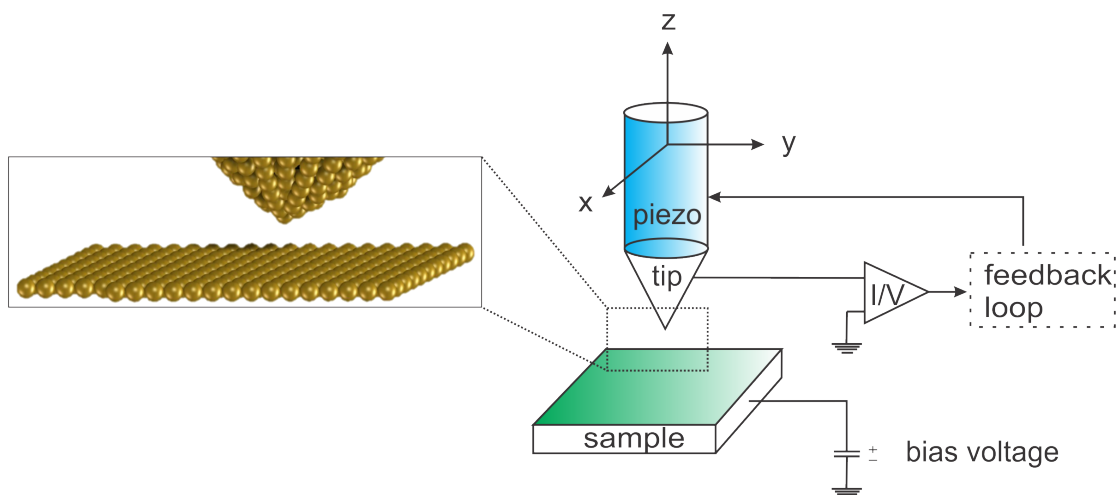


Figure 1.2 – STM working principle.

1.1.4 Scanning tunneling spectroscopy

For the case of non-metal electrodes, the electron energy spectrum is not continuous anymore and might contain discrete states. The scanning tunneling microscopy allows to probe the

local density of states (LDOS) both of tip $\rho_T(E)$ and sample $\rho_S(E)$. When a positive bias voltage is applied to the sample, the electrons from the tip are tunneling into the empty states of the sample. For a negative bias, a reverse process is taking part: the electrons from the occupied states of the sample are tunneling into the empty states of the tip. [40]

The total current can be evaluated by using the Fermi golden rule [41]:

$$dI(V, d) \propto \rho_S(E)\rho_T(E - eV) |M(E, d)|^2 (f_T(E - eV, T) - f_S(E, T)) dE \quad (1.8)$$

where T is the temperature, and $M(E, V, d)$ is the transmission matrix for the tunneling barrier. $f_T(E, T)$ and $f_S(E, T)$ are the Fermi distribution functions for tip and sample respectively:

$$f(E, T) = \frac{1}{1 + \exp(E/k_B T)} \quad (1.9)$$

A possible way to calculate the tunneling matrix element M was originally provided by Bardeen [41]:

$$M \propto \int (\Psi_S^\dagger \nabla \Psi_T - \Psi_T \nabla \Psi_S^\dagger) d\vec{S} \quad (1.10)$$

He assumed that the tip and sample are independent systems and the wavefunctions Ψ_S and Ψ_T could be treated separately. However, for the further calculation of M their concrete evaluation is necessary, which is not that trivial for the STM, since the structure of the tip-apex is not known. Later, Tersoff and Haman used a single s-orbital wavefunction to describe the tip, and the plane wave approximation for the sample. Under these assumptions, the matrix element at zero temperature takes the following form [42]:

$$M^2 \propto \exp\left\{-2d\sqrt{\frac{m}{\hbar^2}(\Phi_S + \Phi_T - 2E + eV)}\right\} \quad (1.11)$$

In order to evaluate the tunneling current, one has to integrate the equation 1.8 over the states from the Fermi energy E_F to eV :

$$I(V, d) \propto \rho_T(E) \int_{E_F}^{E_F + eV} \rho_S(E) \exp\left\{-2d\sqrt{\frac{m}{\hbar^2}(\Phi_S + \Phi_T - 2E + eV)}\right\} \quad (1.12)$$

Regarding the latter expression and assuming that the tip density of states is constant and

independent of voltage, one can easily find that the sample LDOS is directly proportional to the dI/dV signal:

$$\frac{dI}{dV} \propto \rho_S(eV)\rho_T(0) \quad (1.13)$$

1.2 Experimental Set-up

All experiments presented in this thesis were performed on a home made low temperature ultra high vacuum STM, unless stated otherwise. The set-up is presented in Figure 1.3. It consists of two chambers: the cryogenic, which is coupled to the cryostat with the STM itself, and the sample preparation chamber. The latter one is equipped with a horizontal manipulator, where the sample holder is positioned during preparation. It can be heated by electron bombardment from a tungsten filament up to 1200 K, or cooled down by liquid helium flow to 60 K. For ion sputtering a SPECS ion gun is used. Different gases, as for example, argon needed for sputtering, can be dosed into the chamber via a leak valve. The two chambers are separated by a valve, so that each of them can be vented independently. The main preparation chamber is equipped with a four cell versatile evaporation source for organic molecular beam epitaxy and an electron beam evaporator for metal deposition. The transfer of new samples from outside or from the vacuum suitcase into the chamber is performed through a loadlock. The pumping set of the whole system consists of two turbo pumps, two ion getter pumps, one back turbo pump and one membrane pump. In addition, a titanium sublimation pump with multiple filaments is installed at the main chamber.

The cryostat is cooled down with liquid helium and has a base temperature of 8 K. In order to increase the STM stability, it can be passively damped separately from the whole set-up, since the coupling to the main chamber is realized via a UHV welded bellow and is not stiff. The STM head is based on the beetle type design, originally suggested by Besocke [43] and later improved with an inertial coarse approach [44]. Throughout the last four years many improvements have been performed on the STM insert and the UHV chamber. The whole set-up was moved from the old building of the institute to the new precision laboratory.

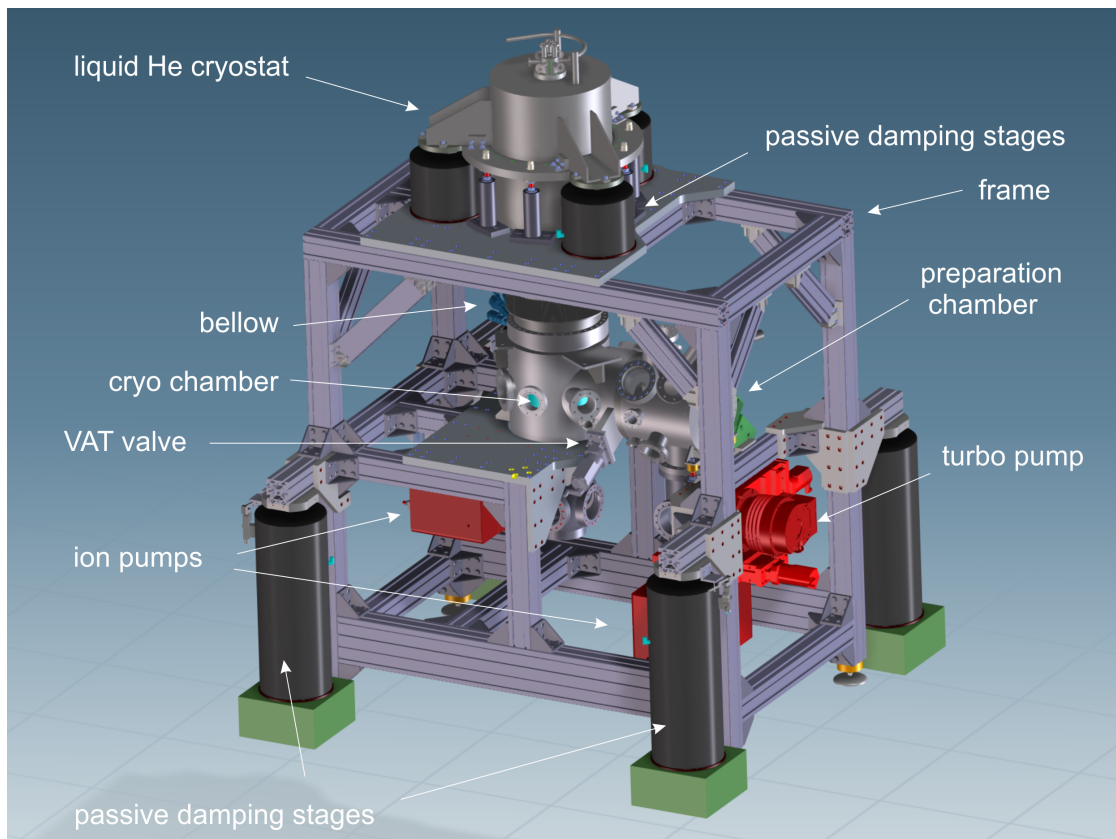


Figure 1.3 – CAD drawing of the low temperature ultra high vacuum STM

2 Quantum noise

2.1 Introduction

Shot noise is a fundamental feature of any tunneling process and appears due to the discrete nature of charge. [45] Already in the 1960s Rolf Landauer predicted, that noise, otherwise referred to as fluctuations in time of current or voltage - can be a source of information. It can provide an insight into complicated physical phenomena, such as non-equilibrium properties of the Kondo regime and composition of individual conductance channels of an atomic size contact. [46]

The very first observation of shot noise was conducted by Schottky in 1918 during measurements on vacuum diodes. [47] Later, in 1951, van der Ziel and colleagues also confirmed its existence in the current passed through a semiconductor. [48]

However, at that moment shot noise was not considered as "useful" for any application. After just some decades, when Rolf Landauer considered the scattering approach for describing the conductance in ballistic transport regime, the interest on this topic started to increase. Later, Lesovik and Büttiker showed that in this case (when the dimensions of the conductor are smaller than the phase-coherence length of an electron) current fluctuations can arise due to the discreteness of passing current. [49], [50] The intensity of these fluctuations is related to the components of a conductor's scattering matrix.

Such ballistic system could be realized experimentally by the break-junction technique; when a thin metallic wire is pulled apart, at some point just several atoms form the so-called quantum point contact (QPC). Due to the narrow constriction, the macroscopic model does not hold anymore and the scattering approach is needed to describe the electron transport.

Obtaining conductance of a QPC is a relatively easy task, whereby the transmission channel composition - the components τ_n of scattering matrix - could not be disclosed just by a sim-

ple I/V measurement. The group of Prof. Ruitenbeek first demonstrated how to extract the information of conductance channels by measuring shot noise over the break-junction. [27] Later it was also shown that similar measurements can contribute to the detection of vibrational scattering modes in nanowires. [51] Ruitenbeek and colleagues measured shot noise by using voltage amplifiers connected to a spectrum analyzer. After performing a background correction with a calibration noise source they were able to achieve an agreement between scattering theory and experiment for the shot noise dependence on bias voltage. However, for the second experiment where the shot noise was measured at different conductances, the obtained values exhibited a wide spread and did not confirm the theoretical prediction. The measurement technique of pulling a wire between two electrodes to establish an atomic contact has a disadvantage of low control of the QPC and a lack of manipulation capability, compared to scanning tunneling microscopy.

Since the shot noise level is proportional to the charge transferred at a single tunneling event, it also allows the observation of many-particle correlations such as the scattering of conduction electrons on a localized spin. Pioneer experiments on quantum dots in the Kondo regime were done in the group of Prof. Kobayashi, where two electron back scattering process was proved by obtaining the corresponding shot noise level. [52] However, such an approach does not allow to probe the spatial extend of the effect observed and, moreover, the fact that the quantum dot is occupied by a large number of electrons at the same time prohibits the examination of the true single spin physics.

In contrast to both techniques mentioned above - break junction and transport measurements on a quantum dot - an ultra-high vacuum STM, working at 4 K, is known to be a powerful instrument to address single objects on the surfaces with atomic precision. Later, H. Birk *et al.* demonstrated compatibility of shot noise measurement procedure with the STM technique. They showed the suppression of shot noise due to the Coulomb blockade on a single-electron tunneling system. [53]

Our original aim was to extract information from shot noise measurements over single atoms and molecules and to determine the number of conductance channels participating in the tunneling process and contribution provided by each. Another interesting application of shot noise detection would be characterization of the many-particle scattering in a Kondo impurity or probing the competition between Kondo screening and magnetic interactions. This data could be complemented by topographic imaging and corresponding I/V characteristics. For this goal, we combined the STM electronics and noise amplification circuits, functioning together at the same time without damaging their individual performance.

2.2 Theoretical background

The main characteristic of noise is the Spectral Density $S(w)$ of a random variable $X(t)$. It is defined as [54, 55]:

$$S_x(w) = 2 \int_{-\infty}^{\infty} \overline{X(t)X(t+s)} \exp(-iws) ds \quad (2.1)$$

The upper equation represents the Wiener-Khintchine theorem, which describes the spectral density as a Fourier transform of the random process correlation function. [54] Classical noise formalism for macroscopic conductors was developed mainly by H.Nyquist, J.Johnson and W.Schottky[56, 57, 47] in the 1st half of the 20th century. Fluctuations of voltage and current, which could be observed in a conductor, are distinguished by their origin and indeed, different spectral characteristics. First, the three types of noise can be defined according to the classical approach.

- **Thermal noise** or Johnson-Nyquist noise. This type of fluctuations always occurs due to the thermal movement of charge carriers and is unavoidable in an electrical conductor in an equilibrium state. Its current spectral density for finite resistance R and temperature T yields[57]:

$$S_I(T, R) = 4k_B T \frac{1}{R} \quad (2.2)$$

where k_B is the Boltzmann constant. The intensity of the thermal noise does not depend on the frequency. It is called white noise - on the analogy of white light - which contains waves at all frequencies.

- **Shot noise** could arise in many different systems, such as a vacuum electron tube or a p-n semiconductor junction. The reason for it lies in the discreteness of electric charge. Its spectral density was originally derived by Walter Schottky for vacuum diodes[47]:

$$S_I(I) = 2eI \quad (2.3)$$

where I is the current passing through. Shot noise is usually also considered to be white noise.

- **Flicker noise** (called also pink noise) is the least understood type of fluctuation. It occurs in a large range of electronic devices and systems. For many processes flicker

current spectral density was roughly approximated by Van der Ziel[58]:

$$S_I(I, f) \sim \alpha I^2 / f \quad (2.4)$$

where α is a parameter, f - frequency and I is the forward current.

However, the classical approach is not sufficient when one starts to decrease the scale of conductors from the macro- to the nano limit. In the latter case, the situation drastically changes and the macroscopic noise theory does not provide an explanation for many observed effects. Here, the scattering approach[46] and Landauer[26] model can be applied to describe conductance and noise behavior of an atomically sized junctions. The conductor is viewed as a parallel circuit of N independent transmission channels between two macroscopic wires and can be described by a scattering matrix \mathbf{S} that consists of $N \times N$ reflection and transmission matrices:

$$\mathbf{S} = \begin{pmatrix} R & T' \\ T & R' \end{pmatrix}$$

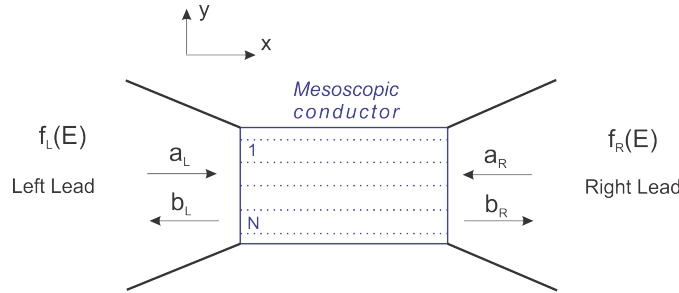


Figure 2.1 – Ballistic conductor (tunnel junction) between macroscopic wires (2 electron reservoirs). N - number of conductance channels. \hat{a} and \hat{b} are annihilation operators for ingoing and outgoing channels of both wires. Adopted from Ref.[46]

A schematic depiction is presented in Figure 2.1. The macroscopic wires act as sources or sinks of charge carriers and the scattering states can be described by applying standard quantum mechanical creation and annihilation operators. The operator $\hat{b}_{\alpha,m}$ annihilates a carrier in an outgoing channel m in the wire α (Left or Right) and operator $\hat{a}_{\beta n}$ annihilates a carrier in an ingoing channel n in the wire β (Right or Left). Consequently, operators $\hat{b}_{\alpha,m}^\dagger$ and $\hat{a}_{\beta n}^\dagger$ create carriers in corresponding channels. The relation between $\hat{b}_{\alpha,m}$ and $\hat{a}_{\beta n}$ is given by the scattering matrix:

$$\hat{b}_{\alpha,m} = \sum_{\beta,n} \mathbf{S}_{\alpha\beta mn} \hat{a}_{\beta n} \quad (2.5)$$

The current spectral density can be calculated from the average current, flowing through the junction. The standard quantum mechanical current operator:

$$I = \frac{ie\hbar}{2m} \int dA \left[\left(\frac{d}{dx} \Psi^* \right) \Psi - \Psi^* \frac{d}{dx} \Psi \right] \quad (2.6)$$

is applied to the scattering states, which describe the reflection and transmission of charge carriers [50]:

$$\Psi(x, t) = \int dE \sum_{n=1}^N e^{-itE/\hbar} \frac{\phi_n(y)}{(2\pi\hbar v_n(E))^{1/2}} [\hat{a}_n e^{ik_n x} + \hat{b}_n e^{-ik_n x}] \quad (2.7)$$

where \hat{a} and \hat{b} are the annihilation operators of the ingoing and outgoing states correspondingly in a certain channel n and $\phi_n(y)$ - are the transverse wave functions. The wave vector k_n is defined as $k_n = \hbar^{-1} [2m(E - E_n)]^{1/2}$ and the velocity of the charge carriers in the n -th channel, considering the free electron-gas approximation, is defined as $v_n(E) = \hbar k_n / m$. By integrating over the cross section of the reservoir dA , one can deduce the current:

$$I = \frac{e}{2\pi\hbar} V \sum_{n=1}^N \int dE dE' [\hat{a}_n^\dagger(E) \hat{a}_n(E') + \hat{b}_n^\dagger(E) \hat{b}_n(E')] e^{i(E-E')t/\hbar} \quad (2.8)$$

The distribution function of electrons in both macroscopic wires is the Fermi distribution function: $f_\alpha(E) = 1 / [\exp(E - \mu_\alpha) / k_B T + 1]$, where μ_α is the chemical potential either of the right or left wire. Hence, the number operator for ingoing states is:

$$\langle \hat{a}_{\alpha m}^\dagger \hat{a}_{\beta n} \rangle = \delta_{\alpha\beta} \delta_{mn} f_\alpha(E) \quad (2.9)$$

with $\delta_{\alpha\beta} \delta_{mn}$ being the delta functions. Using the latter two formulas and equation 2.5 the average current can be evaluated as:

$$\langle I \rangle = \frac{e}{2\pi\hbar} \int dE \left(f_L(E) \left[1 - \sum_{kk} \mathbf{S}_{LL;kk}^\dagger \mathbf{S}_{LL;kk} \right] - f_R(E) \sum_{kk} \mathbf{S}_{RL;kk}^\dagger \mathbf{S}_{RL;kk} \right) \quad (2.10)$$

Considering that the scattering matrix is unitary, one can find that:

$$1 - \sum_{kk} \mathbf{S}_{LL;kk}^\dagger \mathbf{S}_{LL;kk} = 1 - \text{Tr}[R^\dagger R] = \text{Tr}[T^\dagger T] \quad (2.11)$$

Chapter 2. Quantum noise

and $\sum_{kk} \mathbf{S}_{RL;kk}^\dagger \mathbf{S}_{RL;kk} = \text{Tr}[T^\dagger T]$ where T is the off-diagonal part of the scattering matrix, responsible for the transmission of charge carriers through the ballistic conductor. Hence, the average current can be written as:

$$\langle I \rangle = \frac{e}{h} V \sum_{n=1}^N \tau_n \int dE [f_L(E) - f_R(E)] \quad (2.12)$$

$f_L(E)$ and $f_R(E)$ are the Fermi-Dirac distribution functions in the left and right reservoirs respectively, τ_n - is the individual transmission probability of each channel. The conductance increases with the number of open channels by multiples of the conductance quantum $G_0 \approx 77.48 \mu S$ [46]:

$$G = \frac{2e^2}{h} \sum_{n=1}^N \tau_n = G_0 \sum_{n=1}^N \tau_n \quad (2.13)$$

Considering the scattering approach, the spectral density of current fluctuations can be calculated from the expression 2.12 by using the Wiener-Khintchine theorem mentioned above [46]:

$$S_I = \frac{e^2}{2\pi\hbar} \sum_{n=1}^N \int dE \left\{ \tau_n [f_L(1-f_L) + f_R(1-f_R)] + \tau_n [1-\tau_n] (f_L - f_R)^2 \right\} \quad (2.14)$$

After integrating one obtains the general equation for quantum noise:

$$S_I = \frac{2e^2}{h} \sum_{n=1}^N \left\{ 2k_B T \tau_n^2 + \tau_n (1-\tau_n) eV \coth\left(\frac{eV}{2k_B T}\right) \right\} \quad (2.15)$$

The latter formula considers only fermions and is frequency independent, although it does not hold anymore for the very high frequencies $\omega \sim \frac{eV}{\hbar}, \frac{k_B T}{\hbar}$, where vacuum fluctuations come into play. They arise due to the oscillations in energy provided by the Heisenberg uncertainty principle ($\Delta E \Delta t \approx \frac{\hbar}{2}$). These oscillations can be described as virtual particle-antiparticle pairs, which are created and annihilated in very short time spans. For $\omega > \frac{eV}{\hbar}$ shot noise is not proportional to the applied voltage anymore and is described as [59]:

$$S_I = \frac{e^2 \omega}{\pi} \coth\left(\frac{\hbar \omega}{2k_B T}\right) \sum_n T_n \quad (2.16)$$

For the low frequency case and zero voltage, the expression for quantum noise 2.15 reduces to the thermal contribution for finite temperature T:

$$S_I = 4k_B T G_0 \sum_{n=1}^N \tau_n = 4k_B T G \quad (2.17)$$

In the zero temperature limit and a finite voltage V the shot noise spectral density is:

$$S_I = 2eG_0 V \sum_{n=1}^N \tau_n (1 - \tau_n) \quad (2.18)$$

Basically, the $(1 - \tau_n)$ coefficient is the only difference from the classical case. One can see, that the total value of quantum shot noise depends not only on the conductance, but also on the number of transmission channels and their transparency (Figure 2.2 (b,c)). Then, for $\tau_n \rightarrow 0$ the shot noise approaches its classical limit:

$$S_I = 2eGV = 2e\bar{I} \quad (2.19)$$

On the other hand, when τ_n is getting closer to 1, the shot noise is suppressed. The suppression coefficient is called the Fano factor and is determined by:

$$F = \frac{S_I^m}{2eG_0 V \sum_{n=1}^N \tau_n} \quad (2.20)$$

Where S_I^m is the measured current spectral density of the shot noise. In reality, it can be suppressed due to many factors, but in the case of the scattering approach it is the Pauli principle, two electrons with the same characteristics cannot tunnel into the same state at the same time, hence a certain anti-bunching between tunneling events arises. If this is the only reason for suppression, S_I^m should approach the value according to expression 2.18 and the Fano factor takes the form:

$$F = \frac{\sum_{n=1}^N \tau_n (1 - \tau_n)}{\sum_{n=1}^N \tau_n} \quad (2.21)$$

This explains why quantum shot noise can be observed during tunneling processes. In the case when both voltage and temperature have finite values, a transition between thermal- and shot noise contribution is observable (Figure 2.2 (a)). This is well described by a hyperbolic

cotangent. The general current spectral density will then look as in equation 2.15.

It is important to point out that the transmission channel composition does influence not only the electronic transport, but also the thermal diffusivity of the contact. The total value of quantum noise might vary for different number of channels, even when temperature, conductance and voltage applied are kept constant (Figure 2.2 (d)).

2.3 Results

On the way towards performing shot noise measurements, certain challenges arise. Since the shot noise intensity for a μA current is on the order of $10^{-24}\text{A}^2/\text{Hz}$, a strong amplification of the alternating current passing between a single atom on the sample surface and the STM tip is required. On the other hand, together with the shot noise, one amplifies the total noise in the system. Among this are general unavoidable disturbances and crosstalk, arising either because of external influences (GSM networks, mechanical noise etc.) or internal factors that stem from the electronics used for the experiment (amplifiers, voltage/current sources, STM controller). Whereas the outer noise could be relatively easy shielded from the system by using a Faraday cage and filters, the internal one is the most difficult to minimize. An additional problem is the stray capacitance, which makes the whole circuit act like a low-pass filter and limits the frequency range for investigations. Before going to the real measurements at the STM, we decided to perform several tests in order to find out the best circuit for the shot noise amplification.

2.3.1 Test measurements of thermal noise on a resistor using a current amplifier

The Femto-DLPCA-200 is a standard commercial amplifier used for STM current amplification, so it would be very convenient to use it for the shot noise detection at the same time. Usually, during standard STM measurements, the amplifier has a gain of 10^9 A/V . However, because of the relatively high currents needed for a decent shot noise detection one cannot maintain the same operational gain and has to decrease the amplification to at least 10^6 A/V . It allows keeping the feedback of the STM loop closed during shot noise experiment, which is a big advantage.

First, we decided to measure the classical thermal (Johnson-Nyquist) noise just from a metal film resistor. For recording a Fourier transformed spectrum of current, the Stanford Research SR780 FFT spectrum analyzer was used with a uniform frequency window and AC coupling. The data and simple set-up are presented in Figure 2.3.

Such a standard linear resistor exhibits classical thermal noise behavior of $S_I = 4k_B T/R$, which

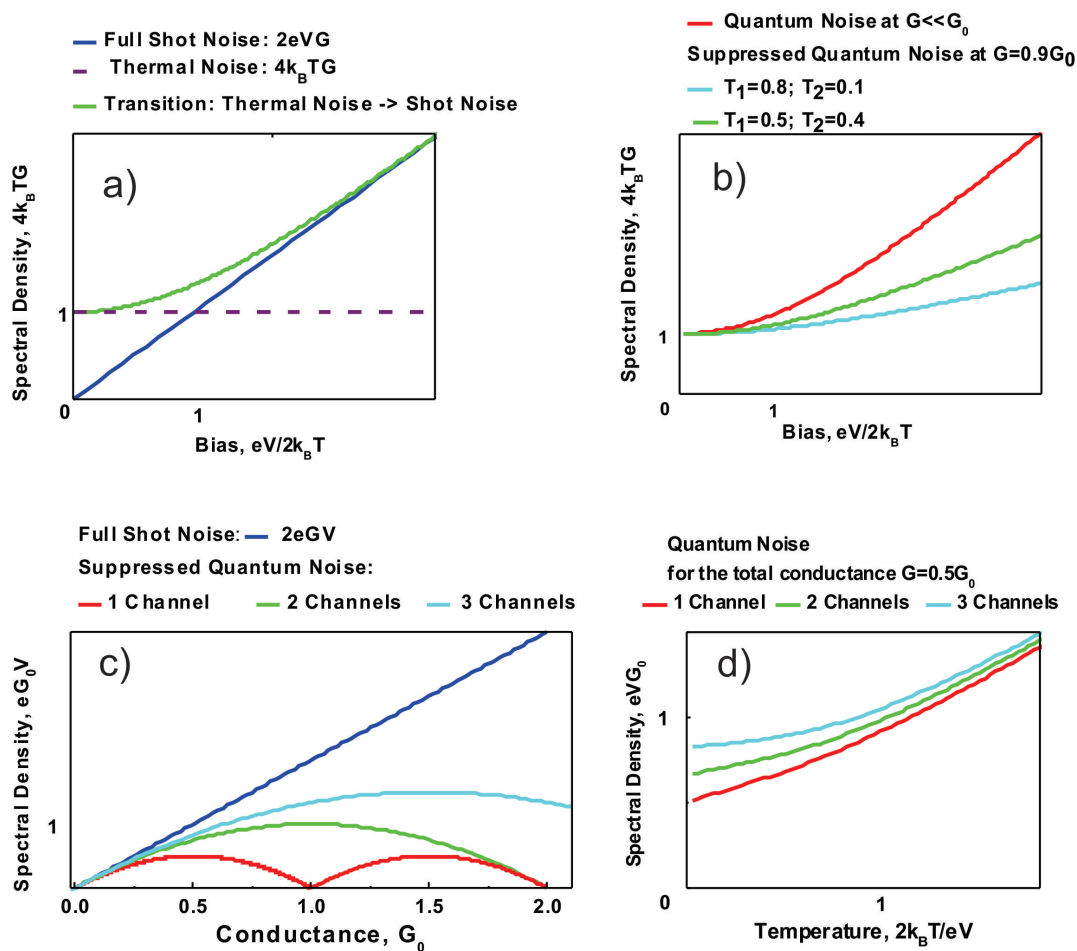


Figure 2.2 – Calculated quantum noise spectral density according to the Landauer-Buttiker formalism.

a) Transition between thermal and full shot noise (no suppression) with bias.

b) Shot noise increase with bias for the case with a negligible suppression (red curve) and for the total conductance of $G = 0.9G_0$ for different transmission channel compositions.

c) Suppression of shot noise for one, two and three channels depending on conductance, blue curve - full shot noise.

d) Dependency of quantum noise on temperature for a constant bias and constant conductance of $G = 0.5G_0$ for one channel with transmission $T = 0.5$, two ($T_1 = 0.1, T_2 = 0.4$) and three channels ($T_1 = 0.1, T_2 = 0.2, T_3 = 0.2$).

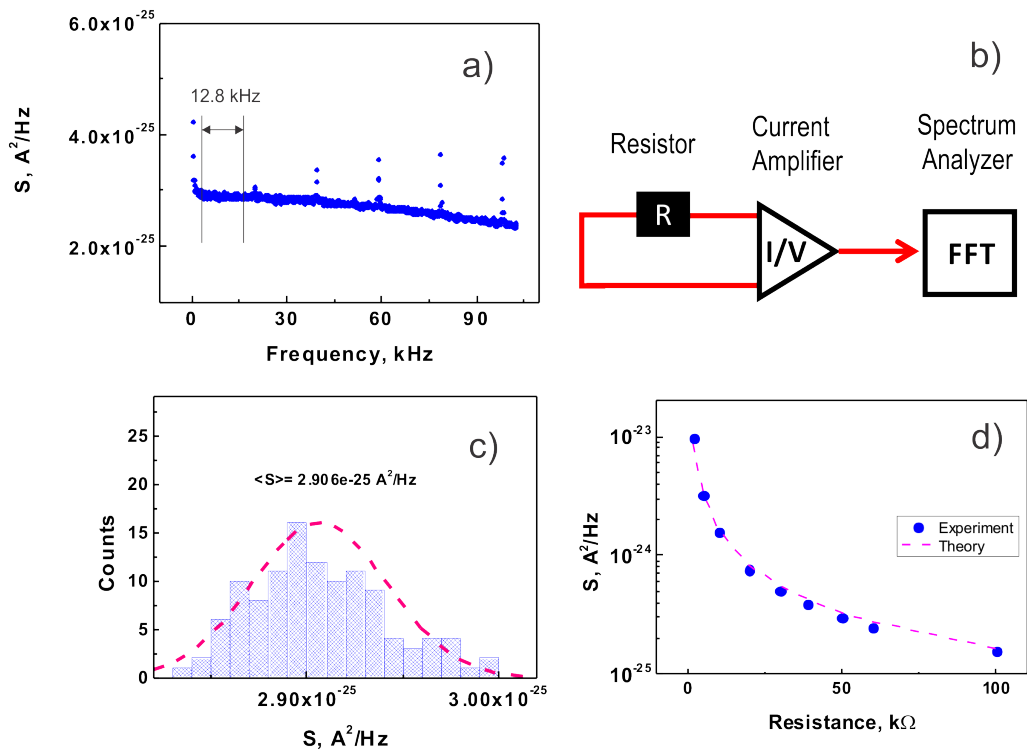


Figure 2.3 – Thermal noise measurements on a metal film resistor.

- a) Typical current spectrum obtained after 1000 averages. Selected span of 12.8 kOhm is shown.
- b) Set-up: resistor - R, I/V - Femto-DLPCA-200 current amplifier (amplification gain 10^6), FFT - SR780 spectrum analyzer.
- c) Histogram plot of the noise values from the span, shown in Figure 2.3 (a) with a Gaussian fit (red line).
- d) Mean noise values over 12.8 kHz span, obtained after a Gaussian fit in Figure 2.3 (c) for different resistances (blue points) and corresponding theory values of thermal noise spectral density: $S_I = 4k_B T(1/R)$ (red line).

could be easily observed; the noise level in the current spectrum is inversely proportional to the resistance value. An example of a spectrum is shown in Figure 2.3 (a). Ideally, the thermal noise is independent of frequency, hence its intensity should be represented in the bottom level, which remains quite uncertain even after 1000 averages at the spectrum analyzer. In order to get a value closer to the true one, the further averaging over different frequencies is necessary. For this purpose the largest span possible of approximately 12.8 kHz was selected, avoiding big sharp spikes. These spikes are provided by the internal crosstalk of the spectrum analyzer and could not be avoided. The noise intensities from the selected span were plotted as a histogram (Figure 2.3 (c)). After a Gaussian fit the mean value of thermal noise in the circuit was obtained. This procedure was repeated for different resistors from 1.9 to 100 kOhm and the result is presented in Figure 2.3 (d). It shows a perfect agreement between theory and experimental data. This procedure for extracting the mean values of noise from an FFT spectrum will be used later on in this chapter.

2.3.2 Test measurements of shot noise on a diode using a current amplifier

The next step was to conduct a test measurement of shot noise. Due to dissipation processes and high thermal contribution, observing shot noise at room temperature in a macroscopic conductor is not straightforward, as it would seem to be from the first look. The 1N4448 Stabilatron (Zener-diode) was found to be a good specimen, which showed the proper shot noise dependence on the bias voltage according to the theory. [58] The important point is that shot noise in diodes, being still a macroscopic effect, does not follow the original Schottky formula for vacuum tubes because the fundamental reason for current fluctuations in a $p - n$ junction is the generation-recombination and diffusion noise of charge carriers.

A detailed study of noise in semiconductor diodes was provided by Aldert van der Ziel and colleagues, where the current spectral density is described as follows [58]:

$$S_I = 2eI + 4eI_0 \quad (2.22)$$

I_0 is the saturation current that comes from the holes generated in the n region and being collected in the p region. Moreover, the interplay of differential and series resistance plays a crucial role; diodes usually have a “parasitic” non-differential resistance R_S , which can be evaluated at the deviation of the diode’s $I(V)$ curve from its exponential character. Such linear resistance brings additional thermal noise into the circuit and should be taken into account

[58]:

$$S_I = \frac{2eIR_D^2}{(R_S + R_D)^2} + \frac{4k_B TR_S}{(R_S + R_D)^2} \quad (2.23)$$

The bias voltage was applied from the Nanonis STM control electronics with a home-made low-pass filter (300 Hz). A 10 kOhm resistor was added in order to limit the thermal noise in the circuit (Figure 2.4 a)). The mean noise values for comparing to the theory were extracted with the same procedure of Gaussian fitting. After that, a very good agreement between experimental data and Van der Ziel theory was obtained, as presented in Figure 2.4 (b).

The two tests discussed above - the thermal noise measurements on a resistor and shot noise measurements on a diode - proved the ability of noise detection with the Femto-DLPCA amplifier.

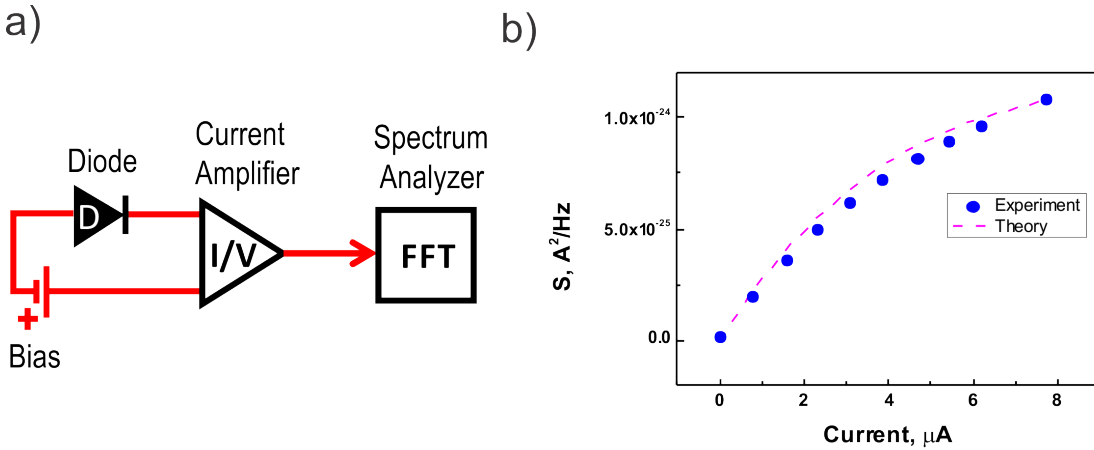


Figure 2.4 – Shot noise measurement from a diode.

a) Set-up: D - 1N4448 Stabilatron, F - homemade low-pass filter (300 Hz), I/V - Femto-DLPCA-200 current amplifier (amplification gain 10^6), FFT - SR780 spectrum analyzer.

b) Mean noise values over 12.8 kHz span obtained after the same procedure of Gaussian fitting, as in the Figure 2.3 and corresponding theory values for shot- and thermal noise in diodes (eq. 2.23).

2.3.3 Thermal noise amplification combined with the STM electronics

The easiest method for the real measurement of shot noise at the STM would be to just plug in the spectrum analyzer to the output of the amplifier and check the noise level for different tunneling currents. However, no difference was observed in the noise levels during changing the current setpoint. The reason might lay in the Nanonis STM electronics, which hampers the shot noise detection. This problem will be discussed in details at the end of this chapter.

A solution that made the noise measurement possible was obtained - the AC and DC currents have to be separated. The constant current needed for STM operation is passed through an inductor to the STM electronics, to keep the feedback operating, whereby the AC part is fed directly to the ground of the current amplifier through a capacitor, in order to establish a shorter circuit (comparing to that of the DC), avoiding the path through the STM electronics. The most promising variant of the circuitry is shown in Figure 2.5.

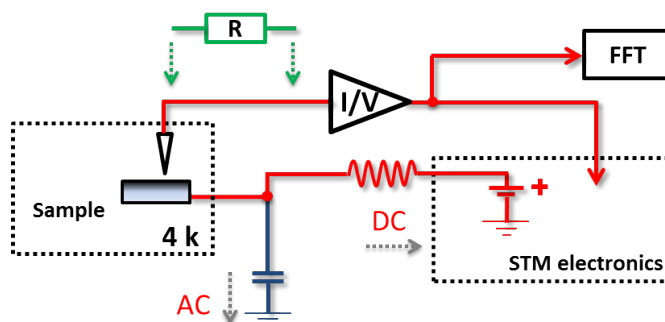


Figure 2.5 – *Set-up: Noise measurement combined with STM circuit. I/V - Femto-DLPCA-200 current amplifier, FFT - SR780 spectrum analyser. The capacitor makes a direct connection to the cryostat ground. Modifications for the test measurement: the tip is crashed into the surface (ohmic contact) and a resistor is installed for providing thermal noise for calibration (shown in green).*

A standard linear resistor exhibits classical thermal noise behavior of $S_I = 4k_B T/R$, which was already observed. The noise level in the current spectrum is inversely proportional to the resistance value.

In order to prove the concept of the established set-up (Figure 2.5), the tip was crashed into the sample surface (Cu111) to create an ohmic contact, a metal film resistor was added in series between the input of the amplifier and tip-sample junction. This resistor provides a known value of thermal noise in the whole circuit, including the contact in the STM. The spectra measured for different resistances are presented in Figure 2.6 (a). The noise level looks almost flat for each of them, except for the one of $1.2 \text{ k}\Omega$, which shows behavior similar to flicker noise for the frequencies lower than 30 kHz. The sharp spikes at 42, 60, 80 and 100 kHz became much stronger probably due to the direct connection to the cryostat ground through a capacitor.

Therefore, a span of approximately 9 kHz at the 84 kHz center frequency was selected. This is far enough from the flicker noise range and does not include any spikes. Further averaging of noise values in the span was performed by a Gaussian fit. The mean value of thermal noise in the circuit was obtained for five different resistors from 1.2 to 70 kOhm. The result is presented in Figure 2.6 (b). One can see that the agreement between theory and experiment is almost

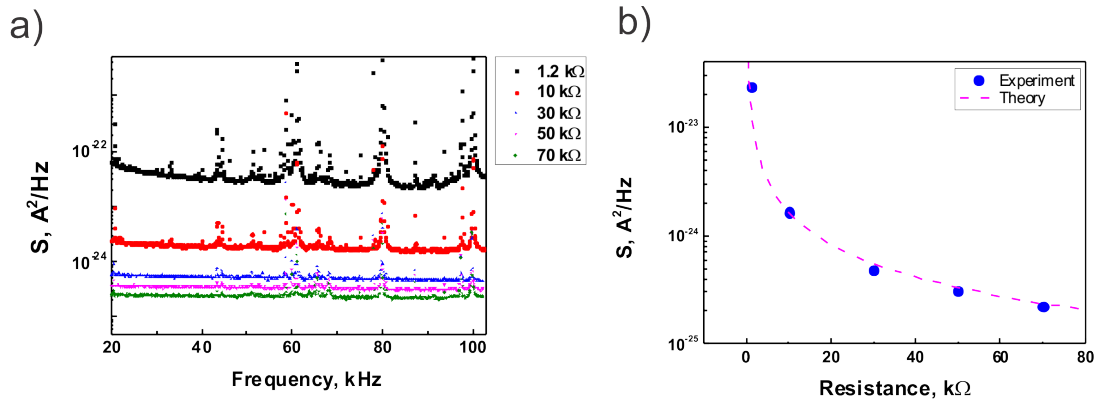


Figure 2.6 – Test measurement of noise within the STM according to the circuit, presented in the Figure 2.5.

- a) Spectra in the range from 20 to 100 kHz taken for different resistance values. Clear peaks at 42, 60, 80 and 100 kHz - unavoidable disturbances.
- b) Mean noise values over 9 kHz averaging span for 1.2, 10, 30, 50 and 70 kOhm resistors (blue points) and corresponding theory values of thermal noise spectral density: $S_I = 4k_B T(1/R)$ (red line).

perfect.

The latter measurement showed that the splitting of the AC and DC currents makes the noise detection possible within the STM.

2.3.4 Shot noise measurement in a weak tunneling regime with the STM by current amplification

For the experiments on a tunneling contact, a Cu(111) sample was prepared by typical UHV procedure. The crystal was sputtered by Ar^+ ions with 1 kV beam energy for 30 minutes and annealed up to 800 K for 10 minutes. After that the sample was transferred directly to the microscope (in a liquid He cryostat), which allows a stable scanning over the sample surface. By slowly bringing the tip towards the surface with extracting the scanning piezo a contact could be formed (Figure 2.7). During this procedure, a drop of a single atom on the surface is possible. In Figure 2.8, a Cu atom on the Cu(111) surface is shown.

Ideally, for observing a suppression of the quantum shot noise, one would like to establish a QPC by approaching the tip towards such a single atom. This should be made in several steps by increasing the current set-point value for the feedback loop. Note that all these steps have different conductance values because the tip-sample distance is changed. At each step, a shot noise measurement was conducted. The whole procedure was performed on a Cu(111) sample in a conductance range from $3 \cdot 10^{-4}$ to $0.12 G_0$.

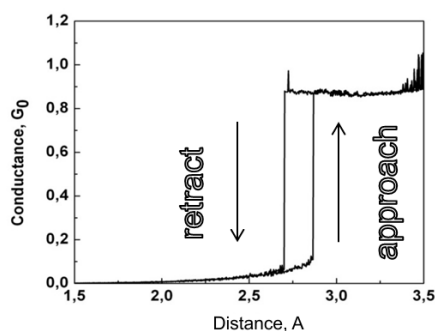


Figure 2.7 – Conductance record during fine approaching the tip towards the surface. The contact plateau corresponds to approximate single conductance quantum. Bias set point: 100 mV

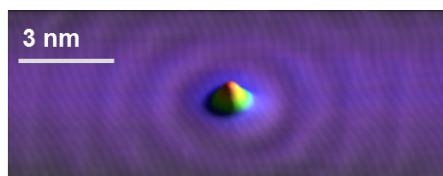


Figure 2.8 – A single Cu atom on Cu(111) surface, dropped during contacting the surface with the tip (Figure 2.7).

After the spectra were taken, the standard analysis for extracting the mean noise values was done. Figure 2.9 (a) presents a span around 70.5 kHz, selected so as to avoid the spikes and flicker noise. Further averaging was performed by a Gaussian fit. The mean values of noise spectral density were plotted against the conductance and current (Figure 2.9 (b)). The theory was calculated according to the Landauer-Buttiker formalism for noise in a ballistic conductor (equation 2.15) and is shown as a red line.

There are general observations concluded from many measurements like the latter one. First, in the weak tunneling regime (conductance $< 0.1 G_0$) the noise intensity has linear dependence on current, which is a typical fingerprint of the shot noise effect. Second, there is a constant offset between theory and experiment. Third, at the values of conductance higher than $\sim 0.1 G_0$ the spectrum starts to be unstable. It means that during averaging the base level (which is relevant for the shot noise determination) is "jumping" and changing its value within a very broad range. Figure 2.9 (a) shows two spectra that are clear separated from the rest. These are the reason for the last two points in Figure 2.9 (b) being significantly higher than the experimental sequence.

As was already mentioned before, together with the shot noise one is measuring all kinds of other disturbances that could not be separated. Due to this fact, a background correction is necessary. For that, the noise level measured at a very small current of 3 nA was defined as

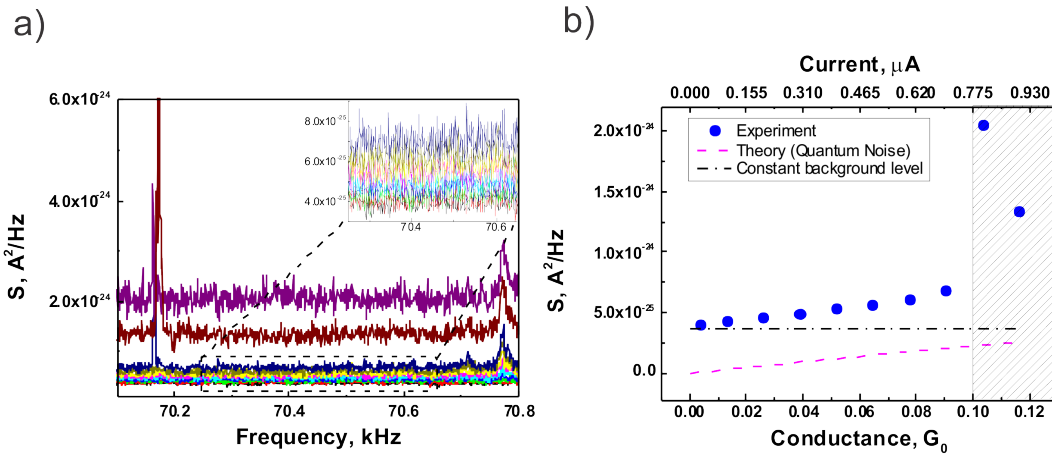


Figure 2.9 – a) Spectra measured at different conductances. Insert - zoom into stable part. b) Mean noise values extracted from a) (blue points). Theory is plotted as a red line according to the equation 2.15. On the top scale, the corresponding current is shown and on the bottom - the conductance values. Unstable region above $0.1 G_0$ is marked with lines. Black dash-dot line - constant background value recorded at 3 nA.

"background". This current set-point is at least one order of magnitude lower than the current for the latter experiment and the real shot noise value is almost negligible there. In addition, the two last data points in the unstable region were removed from the consideration. Figure 2.10 presents data after background correction. For the first five positions, agreement between theory and experiment is perfect, whereas at the end the deviation is much more pronounced and becomes higher than theory values for the full (unsuppressed) shot noise. This could be due to the flicker noise contribution, which is known to have most likely quadratic dependence on current.

Measurements similar to the one described above were tried several times. However, the spectrum always became unstable after the conductance reaching 0.1-0.2 G_0 . This fact and, of course, the big background noise level prompted efforts towards another type of measurement.

2.3.5 Test measurement of thermal noise on a resistor using a voltage amplifier

Shot noise can be also observed in the voltage spectral density recorded across the junction. This was first realized by Ruitenbeek and coworkers. [27, 51] The advantage of this path is the possibility to use the cross-correlation mode, where two voltage amplifiers could be switched in parallel and the spectrum analyzer records the correlation function of the two input signals. During this kind of operation the uncorrelated disturbances in the spectrum, provided by the amplifiers and parallel cabling, are filtered out.

The voltage spectral density is significantly higher than the one of current: $S_U = S_I * R_T^2$ where

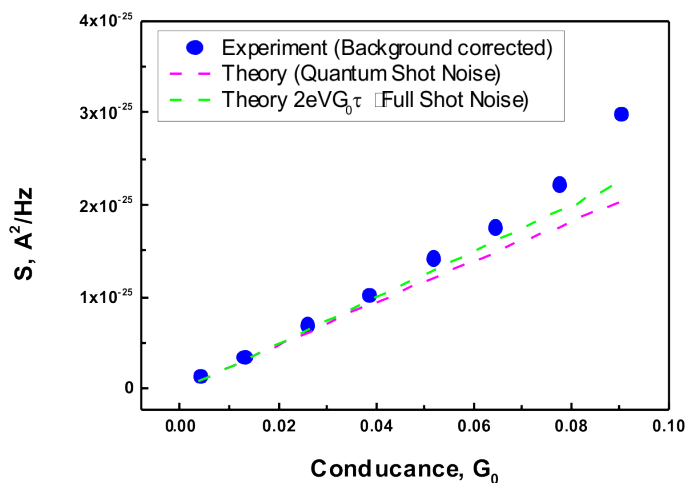


Figure 2.10 – Eight experimental values from the Figure 2.9 after background subtraction. Red line - theory according to the equation 2.15. Green line - theory for the full unsuppressed shot noise.

R_T is the tunneling resistance. Hence, lower amplification gains are needed to measure it. For a test, the thermal noise from a metal film resistor was measured using two commercial voltage amplifiers (Stanford Research SR560). The setup is presented in Figure 2.11 (a). Extraction of the noise values was performed similarly as in the previous sections; by selecting a proper span and Gaussian fitting. Figure 2.11 (b) shows a comparison between theory and experiment (different resistance values) for the cross-correlation test measurement. In addition, both amplification modes were compared; a spectrum taken with a single amplifier and two, running in parallel. The cross correlation output is situated closer to the theory than the single one (Figure 2.12).

2.3.6 Shot noise measurement at a quantum point contact with the STM by voltage amplification

During standard STM performance the feedback loop operates in constant current mode and keeps the position of the tip stable for scanning or I/V spectroscopy. For the shot noise experiment (this time with a voltage spectrum), the feedback should be opened and the cabling switched to the voltage amplifiers. Meanwhile, the FFT analyzer averages the signal in cross-correlation mode. After the spectrum is ready, the system can be switched back to the usual STM circuit and the feedback closed.

The experimental scheme is shown in Figure 2.13. For applying a DC voltage to the junction during the shot noise experiments, one cannot use the bias from the Nanonis STM electronics

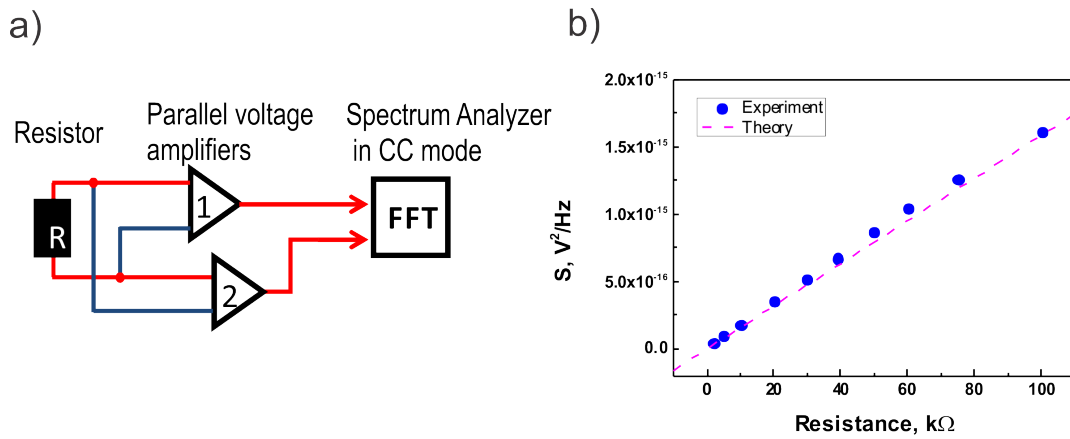


Figure 2.11 – Noise measurement from a resistor by cross-correlated voltage amplification. a) Set-up: R - resistor. 1,2 - SR560 Voltage amplifiers switched in parallel. FFT- SR780 Stanford Research spectrum analyzer. b) Mean noise values for different resistors (blue points) and corresponding theory for thermal noise voltage spectral density: $S_U = 4k_B T R$ (red line)

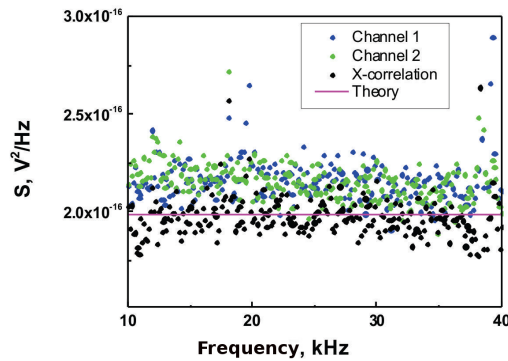


Figure 2.12 – Comparison of a single channel noise measurement from one amplifier (green or blue) and cross-correlation mode with two amplifiers in parallel (black). Corresponding theory value for thermal noise voltage spectral density is calculated according to: $S_U = 4k_B T R$ (red line)

anymore - it is not differential. While commercial voltage sources add additional noise, a special "low-noise" voltage divider was constructed. It applied voltage from a battery and the output was changed by rotating a step motor (Figure 2.14). The divider is supposed to stay as close as possible to the STM (positioned inside a Faraday cage) and be connected to the external controller.

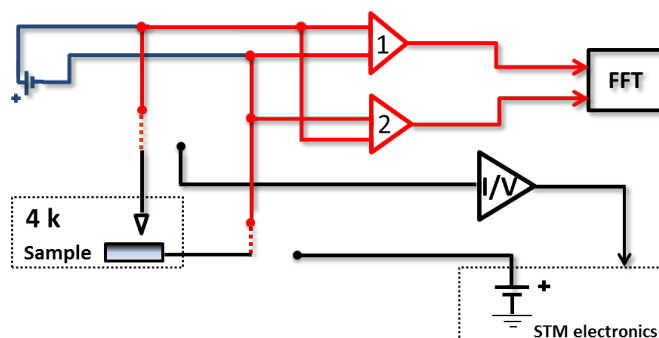


Figure 2.13 – *Set-up: noise measurement is combined with STM circuit through the switch mechanism (switched to the shot noise amplification). I/V - Femto-DLPCA-200 current amplifier. FFT - SR780 spectrum analyser. 1,2 - parallel SR560 voltage amplifiers.*

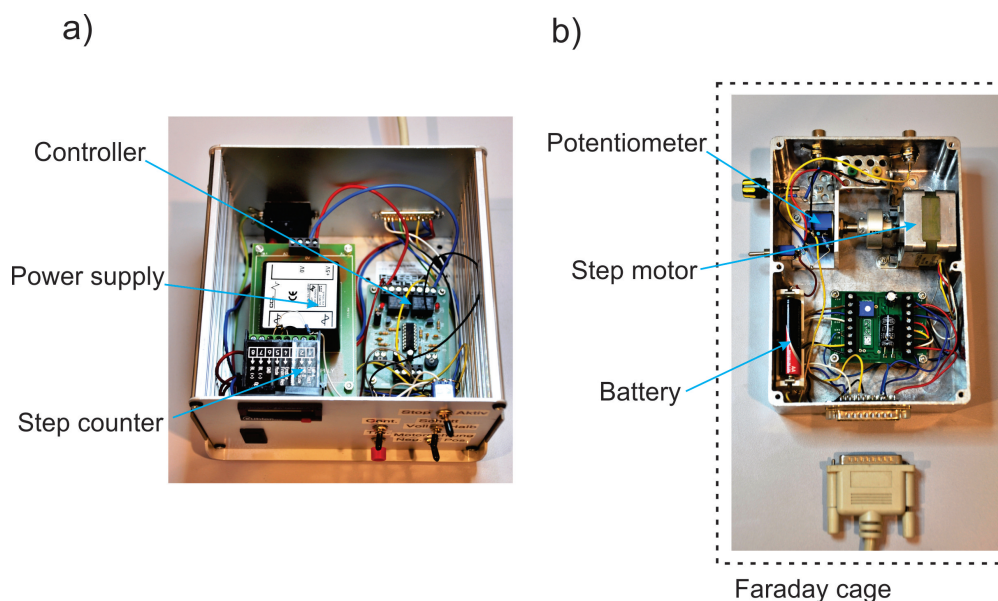


Figure 2.14 – *a) Controller of the voltage divider with the power supply and step counter (for controlling from the desk) b) Voltage divider with a battery and a step motor (to be positioned close to the cryostat feedthroughs).*

We used the already-tested Stanford Research 560 low noise voltage amplifier and the SR780 spectrum analyzer for noise measurement. Results were obtained on a gold QPC. The Au(111) single crystal surface was prepared by standard UHV methods and transferred into a low temperature STM.

At this time, continuing to measure the conductance while the spectrum analyzer was running was not possible (as for the current amplification), because the connection was switched. Therefore, the conductance of the QPC was checked before and after the averaging. The tip was slowly brought towards the surface until the conductance reached its value of $0.27 G_0$.

Shot noise spectra were recorded on an atomic junction for different currents passing through. Examples of spectra are shown in Figure 2.16 (a). Ideally, shot noise is independent of frequency, but in this case a strong roll-off is observable. At frequencies above 12 kHz, even no difference between spectra were observed. To obtain a mean value that can be compared to theory, averaging over a small frequency window is necessary. A span of approximately 2.2 kHz was selected at different center frequencies, chosen to avoid sharp spikes. Later, the standard procedure for extracting the mean noise values was performed. Figure 2.16 (b) shows a zoom into a span at 4.9 kHz for two different spectra. All the values for each spectrum in the selected span were plotted as histogram and fitted with a Gaussian function (Fig. 2.16 c)). Corresponding theory was calculated according to the Landauer-Buttiker formalism (equation 2.15). Its comparison with the result is presented in Figure 2.15 (a,b). One can see that the experimental data (blue circles) show typical shot noise behavior - a linear increase with current. However, the corresponding theoretical line for the conductance value of $0.29 G_0$ (red line) has a much steeper slope. The dependence we have observed is more close to $0.85 G_0$ for a gold monoatomic contact.

2.4 Conclusions

2.4.1 Discussion of the results

All test measurements of thermal noise from a resistor and shot noise from a diode showed perfect agreement with the theory. The standard STM circuitry was modified in order to be complemented with the shot noise detection. For the voltage amplification, a switching mechanism and voltage divider were constructed. For the current amplification, a splitting of the AC and DC components of the tunneling current was done.

The input shield of the current amplifier usually is not connected to the cryostat - it is floating. The tunneling current (including the noise signal) has to go through a long circuit and pass through the STM electronics before reaching the grounding point of the current amplifier. This may hamper the shot noise detection. One of the possible reasons is the frequency dependent output resistance of the STM electronics, which influences the shot noise spectrum. The feedback loop of the STM needs only a DC current in order to keep the tip stable during the measurement, whereby for the shot noise experiment just the AC part is relevant. Hence, the circuitry can be split.

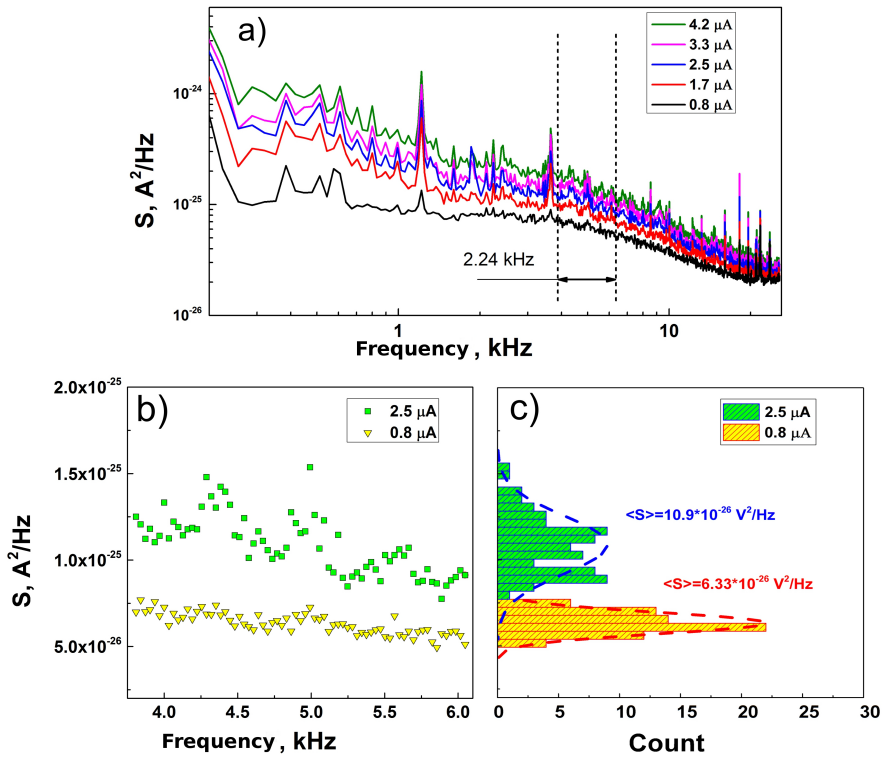


Figure 2.15 – a) Example of several spectra, obtained with the SR780 after 1000 averages. Selected span for further averaging over 2.24 kHz at 4.96 kHz is shown with the black arrow. b) Zoom into the average span for two values of current, passing through the junction. c) Histogram plot of the noise values from the span, shown in Fig. 2(b) with Gaussian fits (red and blue dotted line)

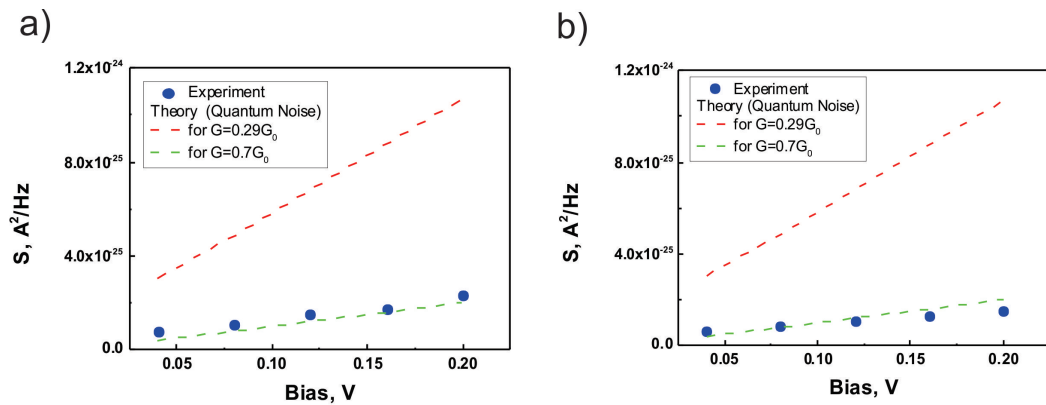


Figure 2.16 – Mean noise values, obtained after a Gaussian fit of values in the averaging span of 2.24 kHz at different central frequencies (2.4 and 4.96 kHz) for different current and corresponding theory values calculated from the expression 2.15 considering only one channel participating in the transport, for a Fano factor of 0.73 in red ($0.27 G_0$). Theory values for Fano factor of 0.15 ($0.85 G_0$) are plotted for comparison in green.

The experimental shot noise values on a copper QPC show a good matching to the theory in the weak tunneling regime after background correction. For the voltage amplification, experimental values were lower than expected. A further challenge was to keep the contact stable during shot noise measurement (means obtaining same conductance before and after FFT averaging). Since all tests worked well, most likely the reason for the disagreement lays in the STM-insert. There is a large variety of electronic effects that could ruin experimental observation of shot noise, from simple over-float by flicker noise to environmental Coulomb blockade because of the impedance mismatch. We decided to measure the transfer function of the STM and evaluate the stray capacitance in order to exclude its "parasitic" effect.

The STM transfer function is presented in Figure 2.17. In the range up to 100 kHz where shot noise was detected, attenuation is about -2.5 dB (0.7 of the power is getting through), which still is not enough to explain the low experimental values for the case of voltage amplification. For the MHz frequencies, the transparency drops drastically and is much lower than the value expected from the wiring inside the STM (Lakeshore coaxial cables). This fact prohibited us to measure shot noise in the RF frequency range.

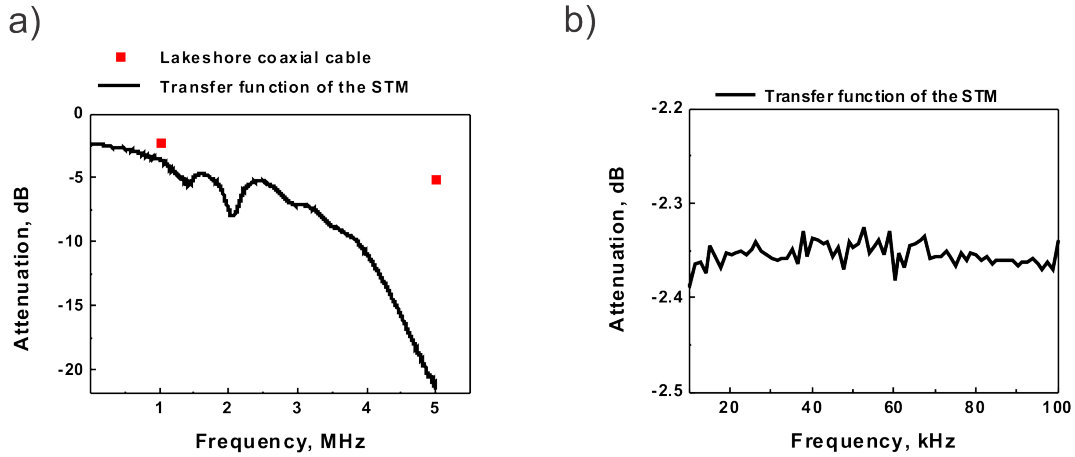


Figure 2.17 – Transfer function of the STM. a) Frequency range from 0 to 5 MHz b) Frequency range from 10 to 100 kHz. Red points - Attenuation characteristic points for a Lakeshore coaxial cable (from datasheet)

The imaginary part of admittance is known to be linearly dependent on frequency $Im\{Y\} = \omega C$. Using a Rohde & Schwarz Network analyzer, which allows to measure the $Im\{Y(C)\}$ directly, and fitting the curve, the approximate value of $C_{Stray} = 1.5nF$ was extracted for the cabling we have (see Figure 2.18). According to Levitov, the measured current spectral density should be reduced, comparing to one at the QPC like [60]:

$$S_I^{LEADS} = \frac{S_I^{QPC}}{1 + \omega^2 R^2 C_{Stray}^2} \quad (2.24)$$

where R would be the vacuum impedance of 307 Ohm. The found value of 1.5 nF is negligible for the kHz frequency range. The authors in Ref. [25] also accounted for a suppression of shot noise by about 1/3 of the expected value at a ballistic contact. Later, Lee and Levitov in Ref. [60] provided a theoretical explanation for these results. They independently regarded two current operators - one for the current through the junction and the other for current in the wires. The reason for shot noise decrease at the weak tunneling regime ($G < G_0$) was found to be the combined effect of charge relaxation time and the quantum dynamics of the environment. In our case, all measurements were done in the kHz range, which excludes the effect of finite relaxation time of the charge on the shot noise intensity.

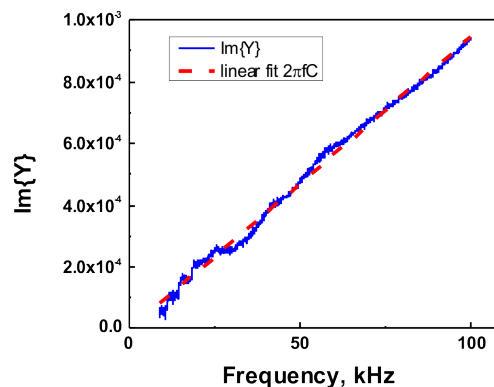


Figure 2.18 – Admittance measurement of the STM insert. Red line - linear fit of the data

2.4.2 Design of the new STM Head

The discrepancy with the corresponding theory both for voltage and current spectral density of shot noise and low transparency of the STM at high frequencies instigated the decision to design a new insert in order to provide access to a larger frequency bandwidth (hence, more flexibility for selection of measurement points in noise spectrum) and possibly increase the ratio between Shot- and all other types of noise. The modifications would be as follows:

- Cryogenic impedance amplifier allowing noise detection up to MHz range.
- Calibration shot noise source, installed in the closest vicinity to the tip-sample junction.
- High-frequency, low loss semi-rigid cabling with transparency up to 60 GHz and double sided grounded shielding.
- SMA or SMK type of connectors, transparent up to 50 GHz.
- *In situ* tip exchange mechanism and controlled X-Y coarse movement. Another interesting possibility would be to install a calibration noise source (tunnel diode) directly in

the tip exchange plug, which would allow to perform a test measurement by contacting roughly different samples.

In addition to the properties mentioned above, a possibility for *in situ* evaporation on the sample is preserved. CAD drawings of the designed STM head are presented in Figure 2.19.

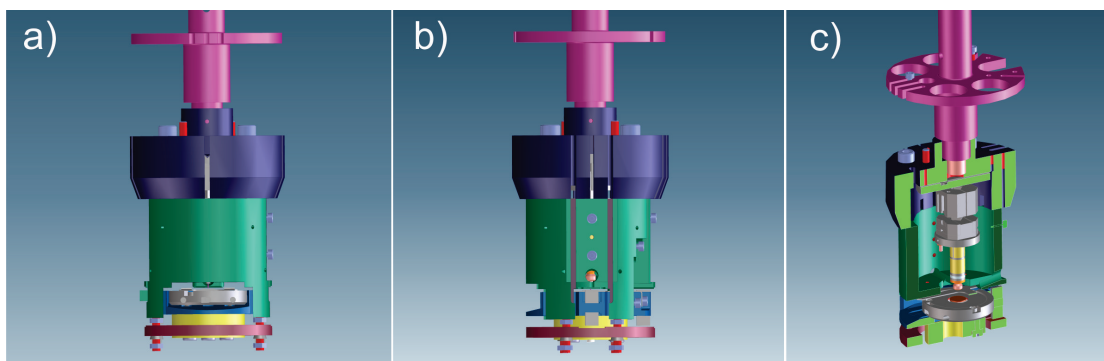


Figure 2.19 – CAD drawing of the STM-Head. a) Front view with the sample-holder (gray color) inserted. b) View from the side c) View on the inner part

3 Pure organic molecule with spin system 1/2

3.1 Introduction

Control of the behavior of single spins opens a broad horizon for new technologies in molecular electronics and is of a great importance for the development of new electronic components. Concerning industrial applications, such a "single spin" component will be contacted by metal electrodes as a part of large integral circuit. The interaction between a free electron gas and a localized spin therefore plays a crucial role in the prospective device performance. One of the intervening processes is scattering of conduction electrons at a single spin impurity called the Kondo effect. It was observed for the first time in a gold wire by de Haas and colleagues in 1934. [61] They measured resistivity as a function of temperature and observed a minimum around 3.7 K, after which the resistivity started to rise with temperature decreasing. None of the existing models explained such an effect at that time. In general, the main reason for resistance in metals is the scattering of conduction electrons by nuclei, defects or electron-electron scattering. When the temperature is decreased the lattice vibrations are frozen out and hence, the resistivity due to electron-nuclei collisions becomes smaller, in direct contrast to de Haas observations.

After almost 30 years, Jun Kondo suggested that the magnetic impurities in metal are responsible for additional scattering processes. When a conduction electron interacts with the unpaired electron of the magnetic impurity, a spin flip might occur. [62] This leads to an increase of the resistivity with temperature decrease up to a certain point, named the Kondo temperature, where the conduction electrons are coupled strongly to the unpaired spin and attempt to screen it.

In recent years interest in the Kondo effect has grown dramatically because of the possibility of investigating its properties not only in bulk samples, but also on a single impurity like individual magnetic adatoms on metallic surfaces. Low temperature scanning tunneling

microscopy is the only method that allows the spatially-resolved interrogation of such systems at the nanoscale. V. Madhavan *et. al* [63] were the first to measure the Kondo effect with the STM technique in 1998 for Co atoms on Au(111). They obtained the so-called Fano line shape in scanning tunneling spectroscopy (STS) and observed its intensity slowly decreasing as a function of the lateral distance from the center of a single Co atom. Since that time, a large zoo of Kondo-systems has been explored by means of STM. Most of these are single transition metal atoms (Co, Fe, La, Cr, Mn etc.) adsorbed directly on various surfaces [64] or embedded in an organic complex like a phthalocyanine molecule [65]. However, the physics of these metal-organic compounds seems to be rather difficult to understand, due to their multiorbital character.

Experimental examination of Kondo physics on pure organic radicals is still a very rare case. Recently Y. Zhang et al. [1] reported on observation of the Kondo effect of an organic complex, containing a nitronyl-nitroxide radical. Its Kondo temperature, being quite low, allowed a unique probing of the weak coupling between the single spin and conduction electrons.

Further studies of the mentioned radical on different substrates is of current importance for understanding of single spin physics and future applications in molecular electronics.

3.2 Theoretical background

3.2.1 Kondo model

Jun Kondo provided a theoretical description of the resistivity increase in metals at low temperatures due to magnetic defects. He considered just the interaction between the spins of the conduction band electrons and the unpaired spin of the impurity. For the unperturbed Hamiltonian the general operator of free electrons was taken [62]:

$$H_0 = \sum_{k,s} \epsilon_k a_{ks}^\dagger a_{ks} \quad (3.1)$$

where a_{ks} and a_{ks}^\dagger are the annihilation and creation operators of an electron in the conduction band with the corresponding wave number k and ϵ_k as its energy. The perturbed Hamiltonian looked as follows [62]:

$$H'_0 = -\frac{J}{N} \sum_{n,k,k'} e^{i(k-k')R_n} \left\{ (a_{k'+}^\dagger a_{k+} - a_{k'-}^\dagger a_{k-}) S_{nz} + a_{k'+}^\dagger a_{k-} S_{n-} + a_{k'-}^\dagger a_{k+} S_{n+} \right\} \quad (3.2)$$

3.2. Theoretical background

where S_n is the spin operator of the n -th impurity atom and R_n is its position vector. Parameter J is responsible for the interaction between free electrons and impurity spin, being positive for ferromagnetic and negative for antiferromagnetic coupling.

Using the second Born approximation, Kondo deduced the resistivity that arises just due to spin scattering:

$$\rho_{\text{spin}} = c\rho_m \left(1 + \frac{3zJ}{\epsilon_F} \log(T)\right) \quad (3.3)$$

where ρ_m was defined as:

$$\rho_m = \frac{3\pi m J^2 S(S+1)V}{N 2e^2 \hbar \epsilon_F} \quad (3.4)$$

with V being is the volume of the crystal, c concentration of impurity atoms and ϵ_F the Fermi energy. One can clearly see from the equation 3.3 that for antiferromagnetic ($J < 0$) coupling $J \log(T)$ will increase towards low temperatures. At a certain point (named the Kondo temperature) it will dominate over classical resistivity and conduction electrons will couple strongly to the impurity spin, which leads to the total spin becoming zero due to the screening. In the case of a ferromagnetic interaction ($J > 0$), the coupling is weak and the total spin of the system remains finite. In summary, there are three regimes of the Kondo effect: antiferromagnetic (AFM) strong, AFM weak (above T_{Kondo}) and FM weak, as it is illustrated in Figure 3.1.

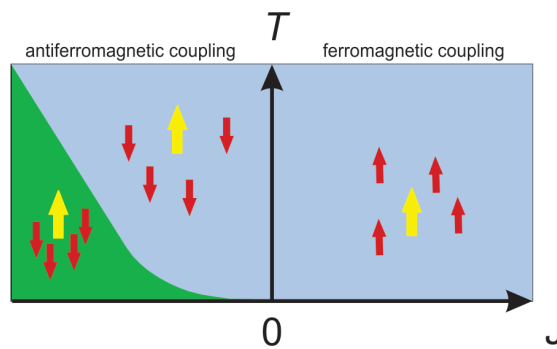


Figure 3.1 – The different regimes of the Kondo effect. Adopted from Ref. [1]. Antiferromagnetic regime for $J < 0$ with both strong coupling (colored green) and weak coupling (colored blue) depending on the temperature. Ferromagnetic regime for $J > 0$ with weak coupling only.

3.2.2 Signatures of the Kondo effect in scanning tunneling spectroscopy

The Kondo effect can be observed on a individual magnetic impurity on a surface by means of STM. A general description of a spin- $\frac{1}{2}$ impurity was provided by Anderson. [66] The interaction of the unpaired spin and conduction electrons creates a sharp resonance near the Fermi level, which can be detected by tunneling spectroscopy in close vicinity of the impurity. A rough sketch of the process is presented in Figure 3.2 (a). The unpaired impurity electron is located below the Fermi level of the host metal. A certain energy is needed to bring that electron up to the Fermi level, but in quantum mechanics such excitations are possible due to vacuum fluctuations [67]. This electron then leaves into an empty state of the metal and another replaces it. The "new" unpaired electron can have an opposite spin comparing to the "previous" one and hence change the spin state of the impurity atom. This action gives rise to a resonant state, positioned quite close to the Fermi energy with a certain half width half maximum Γ . The latter parameter has a direct relation to the Kondo temperature [68]:

$$\Gamma = k_B T_K \simeq \sqrt{2\delta \frac{U}{\pi}} \exp\left\{-\frac{\pi}{2\delta} \left\{ \left| \frac{1}{\epsilon_f} \right| + \left| \frac{1}{\epsilon_f + U} \right| \right\}^{-1}\right\} \quad (3.5)$$

Where ϵ_f is the difference between the Fermi level of the host metal and energy position of the unpaired impurity electron, U - coulomb repulsion energy in the case of two electrons occupying the impurity state and δ - broadening of the impurity orbital due to its hybridization with the conduction electron sea.

However, the Kondo effect does not usually appear as a peak in the STS, but rather like a dip or a mixture of both. Ujsaghy *et. al* [69] showed that a magnetic impurity below the Kondo temperature, observed by STM, causes the so called Fano line shape of the resonance. The reason for this lies in the tunneling process; electrons from the tip being positioned close to the magnetic atom on a surface have several possibilities for tunneling. They can either tunnel directly in the localized state of the magnetic atom or into the Fermi sea of the metal. In the first case, a spin flip is involved. These two paths interfere and provide a spectroscopic feature, described by U.Fano [70]:

$$\rho(E) \propto \rho_0 + \frac{\left(q + \frac{E - E_K}{\Gamma}\right)^2}{1 + \left(\frac{E - E_K}{\Gamma}\right)^2} \quad (3.6)$$

with E_K being the exact position and $q \sim \frac{\tau_{\text{Impurity}}}{\tau_{\text{Fermi Level}}}$ denoting the relation between direct and

indirect tunneling matrix elements. Figure 3.2 (b) presents various shapes of Kondo resonance for different values of q -factor. Later, a more accurate function was derived by H.O. Frota [71]:

$$\rho(E) \sim \frac{1}{2\pi} \chi \epsilon \sqrt{\frac{E + i\Gamma}{i\Gamma}} \quad (3.7)$$

which will be used for fitting the data, obtained in this thesis.

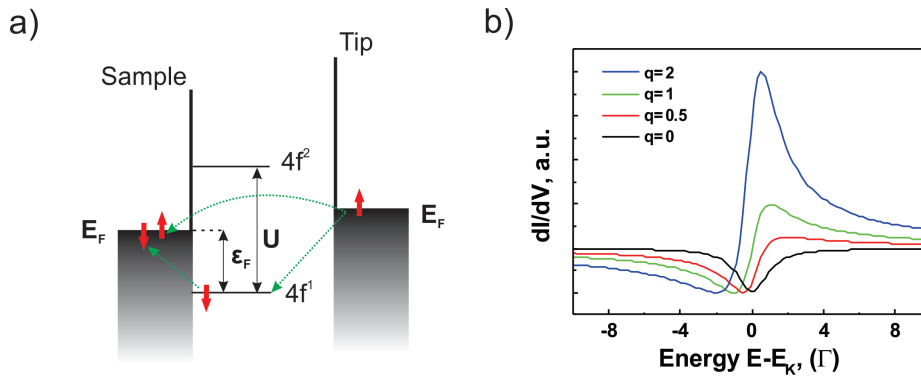


Figure 3.2 – a) Schematic depiction of the experiment with a spin 1/2 impurity (for instance, a Ce atom with one electron in the 4f orbital) on a metal surface and a close approached STM tip. b) Different shapes of Kondo resonance calculated with Fano equation for various q -factor values. Adopted from the Ref. [64]

3.2.3 Overview / Motivation

In this chapter experimental investigations of an organic molecule $C_{28}H_{25}O_2N_4$ will be discussed. Its chemical structure is presented in Figure 3.3. The full name of the complex is 2'-nitronilnitroxide-5'-methyl-[1,1';4',1'']terphenyl-4,4''-dicarbonitrile, called here NMTD for simplicity. It contains a nitronyl-nitroxide radical, which was discovered by Ullman [72] and proved to be the first purely organic magnet [73]. This side group with two NO bonds is responsible for maintaining an unpaired electron. During surface adsorption the radical is expected to be protected from chemical reactions and charge transfer by the large backbone of the molecule, consisting of three benzene rings.

Previous STM studies showed that the molecule, when adsorbed on a Au(111) surface, demonstrates a zero bias anomaly, [1] which was attributed to a Kondo effect in the weak coupling regime. This is a very unique case. The Kondo temperature of the NMTD is below 1.5 K, [74] which allows one to probe the weak coupling of the radical spin to the conduction electrons already at the temperature of liquid Helium (4.2 K). For other Kondo systems, like, for instance, single cobalt atoms on copper surface, one needs to heat the sample up to about 60 K in order

to approach the same interaction regime, since the Kondo temperature is about 55 K. [75] However, heating up will result in the atoms becoming mobile and forming clusters on the surface, which will prohibit examination of the local Kondo effect at the nanoscale. Therefore, the NMTD compound is a good playground for the investigation of Kondo physics by means of low-temperature STM.

Our interest was to explore further the behavior of the nitronyl-nitroxide radical on different substrates. For this purpose, cobalt and palladium were chosen, due to the former being ferromagnetic and the latter paramagnetic.

3.3 Results

3.3.1 Experimental approach / Sample preparation

All experiments were performed in a home-built low temperature STM operating in ultra-high vacuum (UHV). The setup is described detailed in the 1st chapter of this thesis.

Single crystals of Cu(111) and Pd(111) were prepared by standard UHV procedure of sputtering and annealing cycles. The Cu(111) crystal was sputtered by Ar^+ ions with 1 kV beam energy for 30 minutes and annealed up to 800 K for 10 minutes. The palladium crystal was sputtered with higher energy of 3 kV and annealed up to 1000 K. Moreover, additional annealing in oxygen atmosphere was performed for Pd in order to reduce the amount of carbon defects.

The NMTD molecule was synthesized by C. Stroh at the Karlsruhe Institute of Technology (KIT) and delivered in the form of a purified powder. [76] For deposition, it was sublimated inside the UHV chamber at 475 K in a crucible pointing to the sample surface, which was simultaneously cooled down to ≈ 250 K with liquid nitrogen in order to prevent agglomeration of molecules into clusters.

Cobalt islands on Cu(111) surface were grown by evaporation from a cobalt rod heated by electron bombardment and targeting towards the sample. Deposition of approximately 0.6 monolayers resulted in formation of triangular Cobalt islands on the copper surface [77].

3.3.2 NMTD on Pd(111)

A typical constant current STM topography of the NMTD adsorbed on Pd(111) surface is presented in Figure 3.4. The appearance of the molecules is quite similar to what was previously observed on Au(111). The main protrusion is interpreted as the nitronyl-nitroxide radical. [1] However, upon closer inspection subtle differences in STM scans were found.

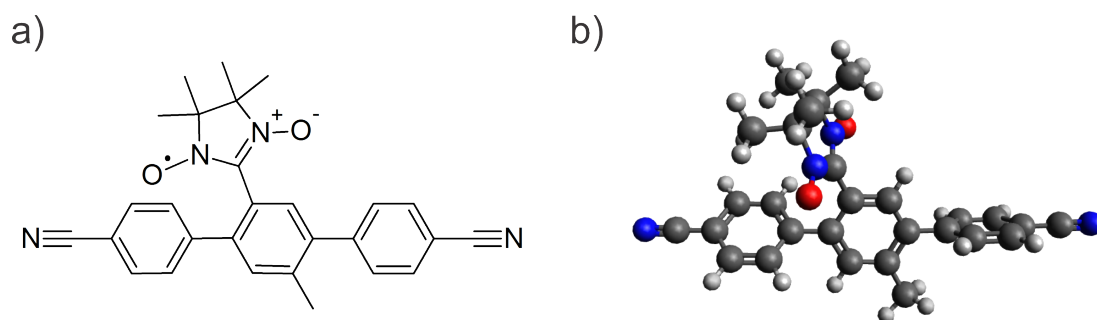


Figure 3.3 – a) Chemical structure of the NMTD. b) Corresponding 3D model.

In Figure 3.5 three molecules with notable conformation variances are presented. The large protrusion changes its apparent height and position from (a) to (c), which is also clearly represented in the horizontal line scans of each molecule (Figure 3.6). These differences could be attributed to the varying position of the nitronyl-nitroxide radical, which stands up with different angles to the surface.

By means of the STS we measured the local density of states (LDOS) by first positioning the tip on the apparent center of the radical. All the investigated molecules showed similar spectroscopic features; two broad symmetric peaks and a zero bias anomaly. The broad features slightly vary their position for different molecules, moving closer to each other. For the molecule (a) in Figure 3.5 the peaks are positioned around ± 200 mV, whereby for (b) and (c) they appear shifted to ± 100 mV. Apart of that, the zero-bias anomaly changes its behavior from peak to dip or even Fano shape. The dI/dV spectrum, taken on the bare Pd(111) surface is plotted in red for comparison on the (b) part in Figure 3.5. On the (a) and (c) parts an approximate fit with three Lorentzian functions is shown.

Spectra in the smaller range from -50 to 50 mV are shown for the same molecules in Figure 3.7. Similar to the case of NMTD on Au(111) [1], the Frota function [71] was used for fitting. Extracted half width at half maximum value is not the same for two fits - in Figure 3.7 it is 10.7 mV for (a) and 4.6 mV for (b). The center of the peak on the first plot is shifted from zero to -8.9 mV.

In order to verify the spatial distribution of the spectroscopic features, a dI/dV map with resolution of 18×32 points was acquired on the apparent position of the radical and in its closest vicinity. In Figure 3.9 (a) STM topography with the selected region for spectroscopic map (white rectangle) is presented. All spectra were fitted with a superposition of three Lorentzian functions, as it is shown in Figure 3.8 for 5 points, positioned on the horizontal cross section over the molecule. These fits showed that the central peak exhibits the highest intensity exactly on the radical location and is much weaker on the molecular backbone or

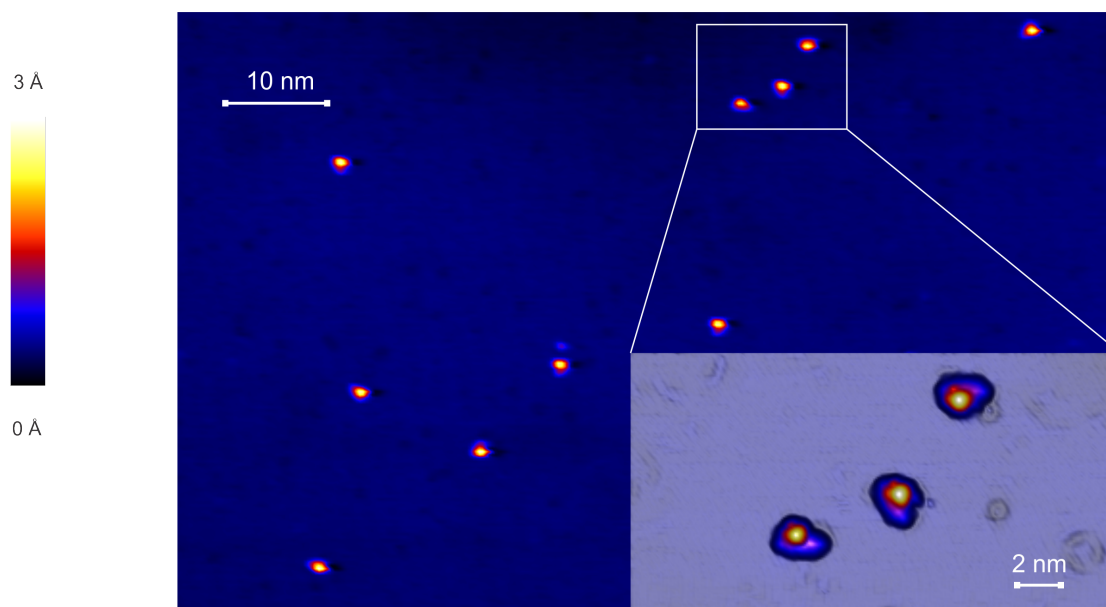


Figure 3.4 – Constant current STM topography for NMTD on Pd(111). Set Point: 0.1 V and 0.1 nA. Inset - zoom into a small area with three molecules.

disappears completely on the palladium surface (Figure 3.9 (b)). The same holds for the right Lorentzian (broad peak at positive bias), which is mostly localized at the center of the map (Figure 3.9 (c)). However, the broad feature at the negative bias (left Lorentzian) is not that pronounced, which hampers the fitting procedure and does not provide a clear estimation for the intensity distribution.

The broad side peaks, obtained for all molecules might be contributed to a split molecular orbital, whereby the central anomaly appears apparently due to the Kondo effect. All spectroscopic features will be carefully discussed in the conclusions of this chapter.

3.3.3 NMTD on Co Islands on Cu(111)

Cobalt islands on Cu(111) are well known for playing a role of a ferromagnetic electrode in STM experiments. [78] Figure 3.10 (a) presents a typical constant current topography of 0.6 monolayers of cobalt on copper. With a cobalt-coated tip, created by picking up part of the island, it is possible to probe the spin polarized density of states and distinguish between clusters with different magnetization directions, like that in Figure 3.10 (b). dI/dV spectra taken on both types of the cobalt islands exhibit typical spin polarized density of states for parallel and antiparallel orientations with respect to the tips magnetization (Figure 3.10 (c,d)). The peak at -0.3 V is a characteristic feature and corresponds to minority $d_{3z^2-r^2}$ states. [79] Note, the obtained contrast in dI/dV signal (Figure 3.10 (b)) is not due to different stacking of Co islands, since several islands are found with the same direction of stacking, but exhibit

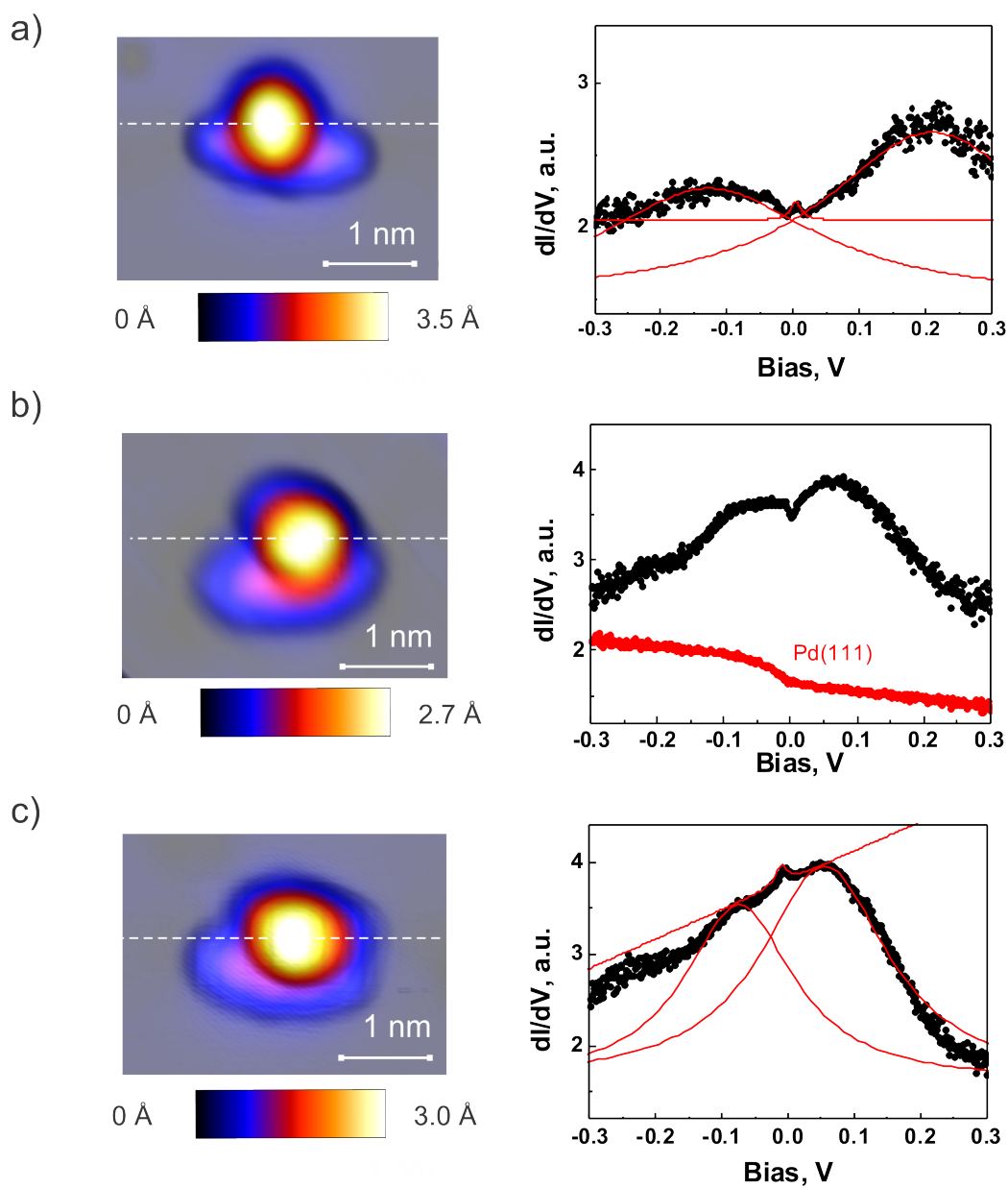


Figure 3.5 – Different adsorption conformations of NMTD. STM topography with corresponding STS signals, taken on the radicals. For (a) two broad peaks are positioned around ± 200 mV. For (b,c) - around ± 100 mV. In (a) and (c), an approximate fit with three Lorentz functions is shown. For the molecule (b) the spectrum taken on the Pd(111) surface is plotted for comparison. Dashed lines - apparent height profiles, presented in Figure 3.6.

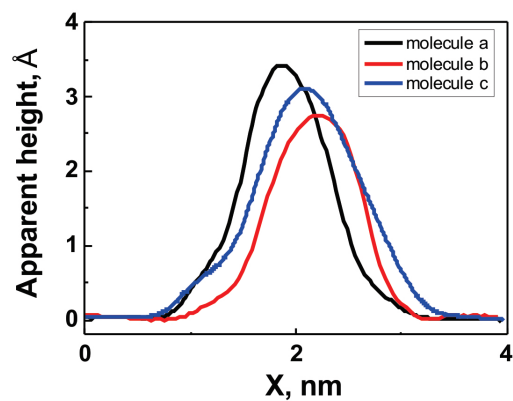


Figure 3.6 – Profile comparison for the three molecules from the Figure 3.5. The apparent height variation is observable.

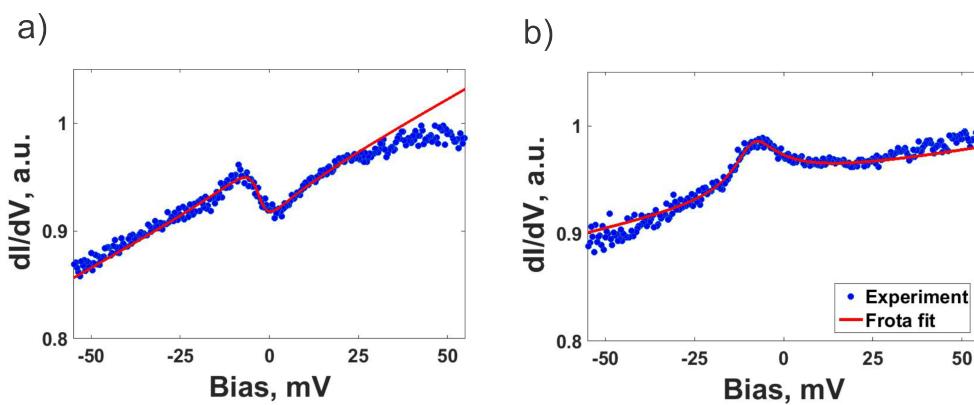


Figure 3.7 – dI/dV spectra taken on the two molecules (Figure 3.5 (b) and (c)) in a small voltage range showing a dip on the (a) with $HWHM=4.6$ meV and a peak on the (b) with $HWHM=10.7$ meV around zero bias. Apparent Kondo features are fitted with a Frota function.

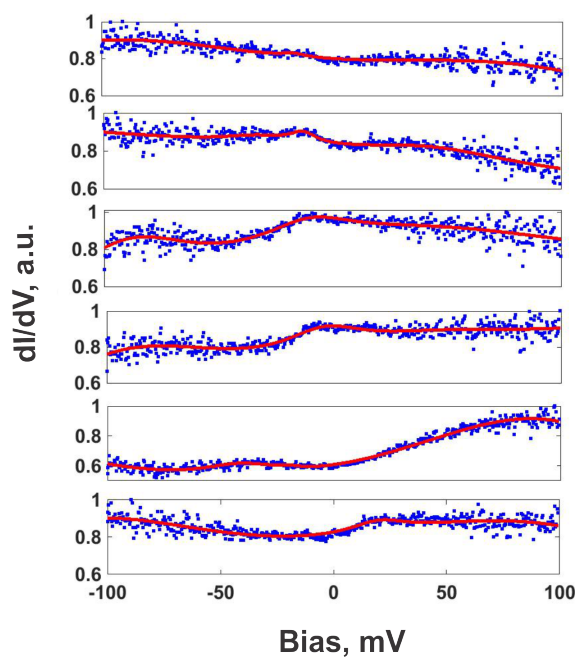


Figure 3.8 – Spectra from the dI/dV map along the dashed line in Figure 3.9. The fit is performed using a superposition of three Lorentz functions.

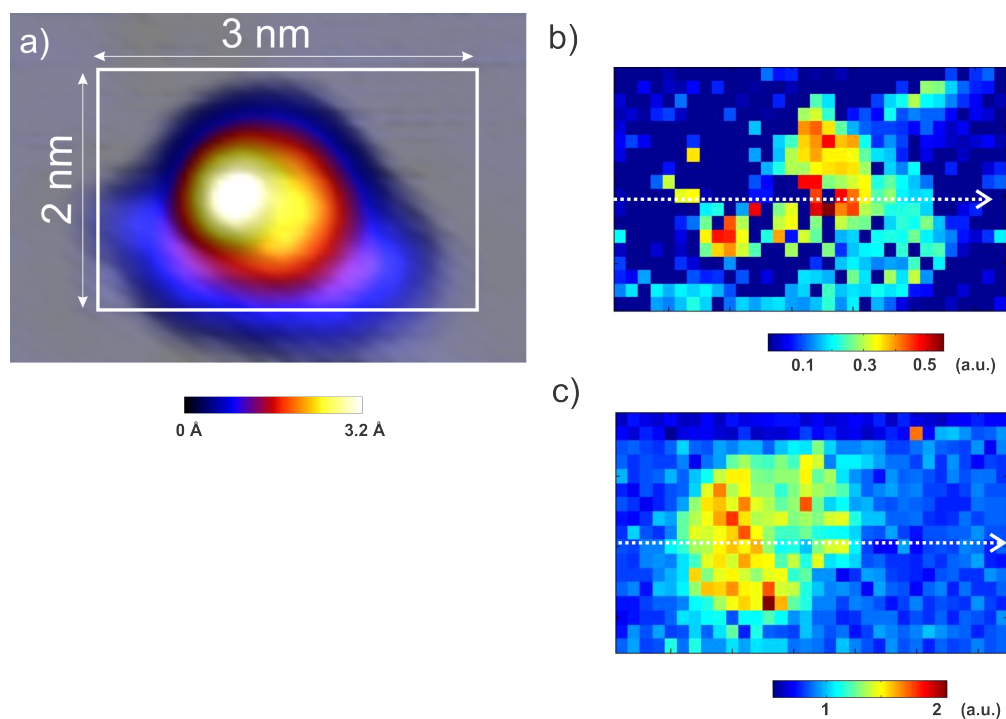


Figure 3.9 – dI/dV spectral map of an NMTD molecule. a) Topography scan in constant current mode. b) Intensity distribution of the central Lorentzian. c) Intensity distribution of the right (at positive bias) Lorentzian. Clear localization of the peak is observable. White dashed line - indication for the position of the spectra in Figure 3.5.

different intensities in the dI/dV spectra.

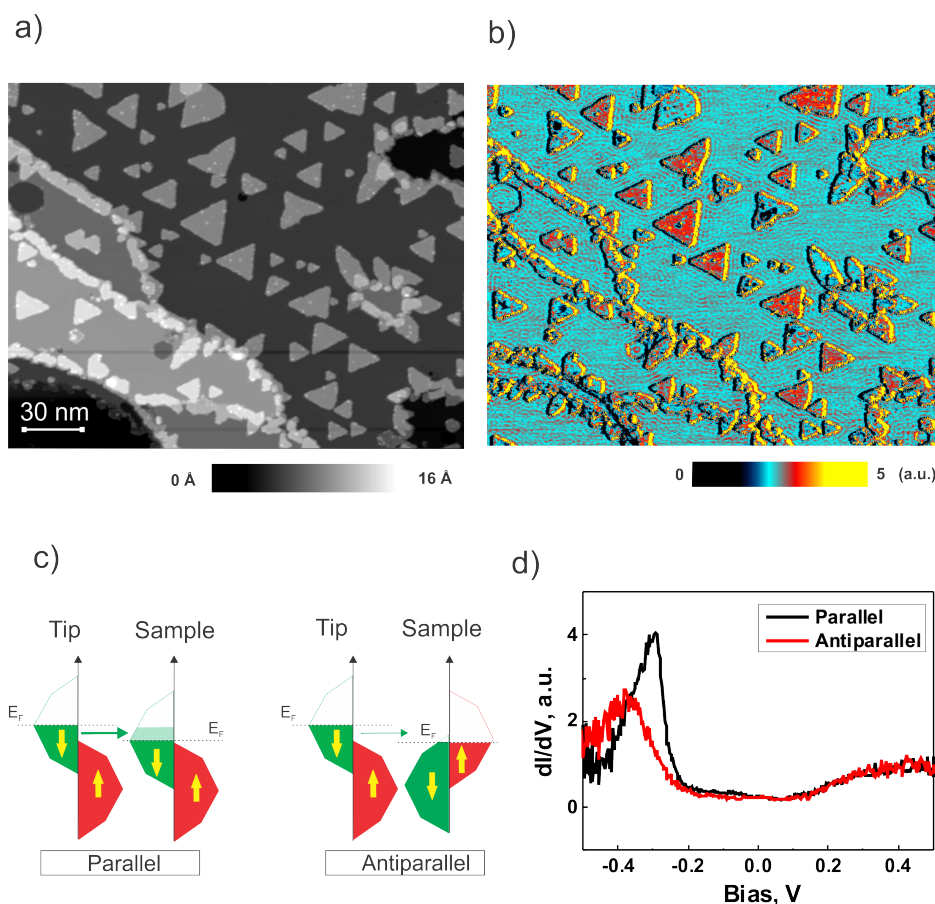


Figure 3.10 – Co islands on Cu(111). a) STM constant current topography. b) dI/dV signal. Islands with different spin polarization are observable. Set Point: $V=-0.25$ V and $I=0.1$ nA c) Schematic representation of spin-polarized tunneling process. d) Typical dI/dV spectra taken on the parallel and antiparallel oriented Cobalt islands with respect to the tip magnetization

The NMTD molecules were deposited on top of the cobalt islands. A typical STM topography is presented in Figure 3.11 (a). The adsorption geometry is similar to what was found on Pd(111) and on Au(111) surfaces before. However, the dI/dV spectra showed a previously unobserved broad dip at the center with slightly pronounced step-like singularities (Figure 3.11 (b)). The corresponding energies of these are usually associated with inelastic electron tunneling due to vibrational modes of the molecule. Spectra in the smaller range from -300 to 300 mV are shown for two different molecules in Figure 3.12 (a). Generally inelastic signatures should appear more clear in a d^2I/d^2V signal, which is processed with a low-pass smoothing. Figure 3.12 (b) presents derivative of the obtained spectra from plot (a). The most pronounced features (dips at negative bias and peaks at positive) does not appear quite symmetric, which might be explained by the effects of an asymmetric junction configuration.

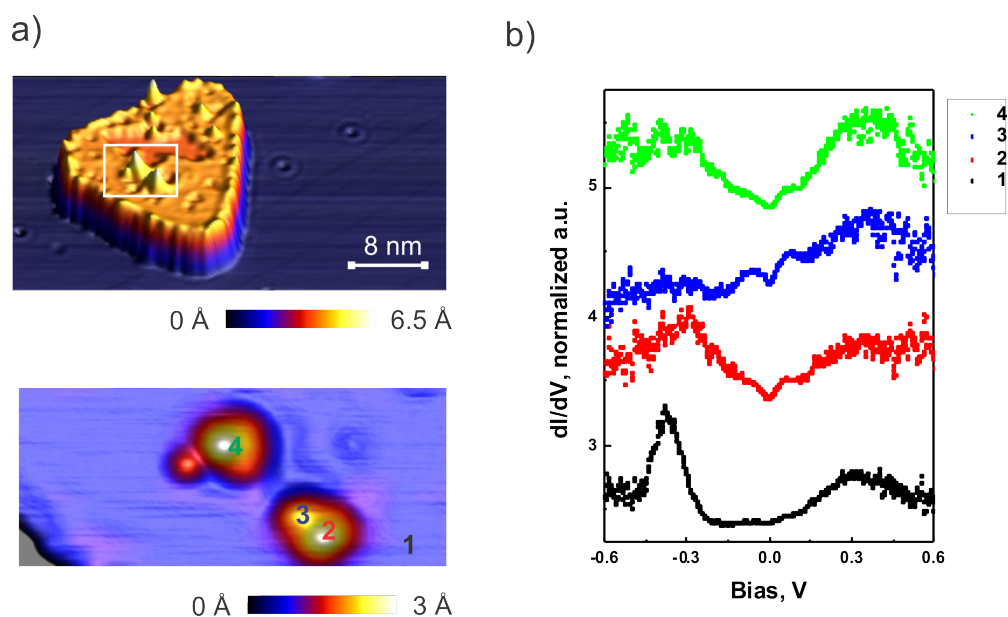


Figure 3.11 – NMTD molecules on cobalt islands on Cu(111). *a*) STM constant current topography. *b*) dI/dV spectra for two different molecules. The numbers of the spectra correspond to the marked points in (a); the spectrum on the bare cobalt island is shown in black for comparison.

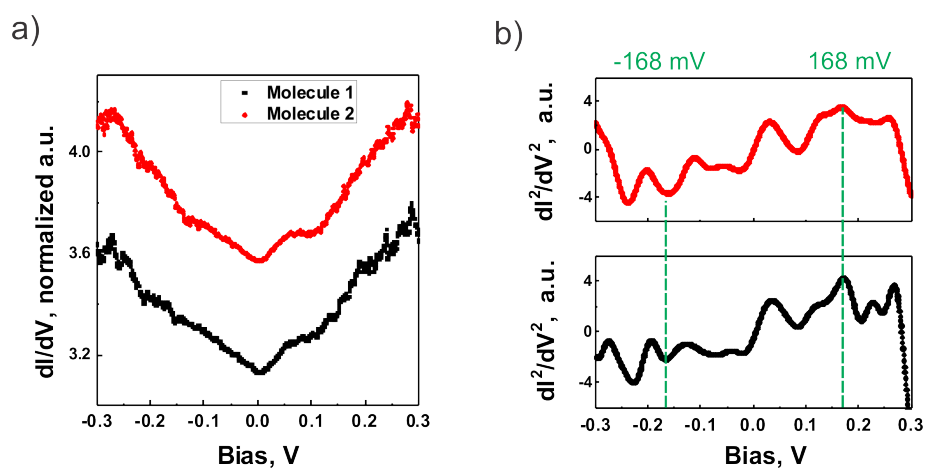


Figure 3.12 – *a*) dI/dV spectra in the range of ± 300 mV for two different molecules. *b*) Derivation of the spectra from (a) with low-pass smoothing.

3.4 Conclusions

3.4.1 Discussion of the results

The NMTD molecule was investigated by means of STM on two substrates - Pd(111) and Co islands on Cu(111). For both cases their dI/dV spectra reveal complicated structure of LDOS.

Typical dI/dV signal for NMTD on the palladium surface consist of two broad side peaks and a zero-bias anomaly. The latter one could be ascribed to the Kondo effect, which was already observed for this molecule on Au(111). [1] However, contrary to the previous studies, where just a peak appears in STS, in the case of adsorption on Pd(111) the zero bias feature changes from one molecule to the other and exhibits different shapes of Kondo resonance. These could be assigned to both direct and indirect tunneling processes dominating on different molecules and their interference resulting in a Fano shape. Also the presumed Kondo temperature extracted from the fits is much higher than what was found on the gold surface before and varies from 50 K to 124 K.

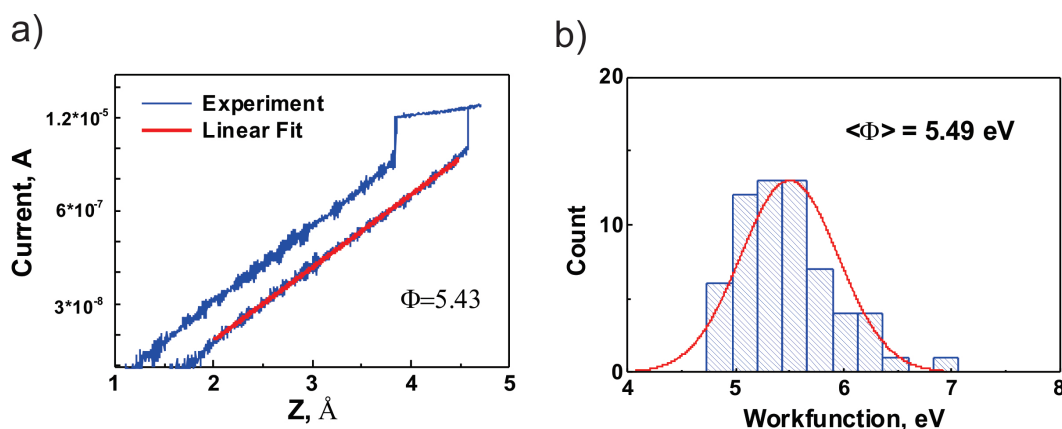


Figure 3.13 – Estimation of the Pd(111) workfunction. a) Current record during close approach of the tip towards the surface, plotted on a logarithmic scale. b) Histogram of obtained workfunction values with a Gaussian fit.

Two broad peaks appearing at $\pm 200 \text{ mV}$ or closer to zero could be attributed to a single occupied molecular orbital (SOMO), which is split due to the Coulomb interaction. A similar effect was already observed for molecules adsorbed on metals by the groups of Pietro Gambardella [65] and Ignacio Pascual [80]. dI/dV spectrum from Ref. [65] is presented in Figure 3.15 (a). In both cases, two broad peaks at negative and positive bias were associated with single and double occupation of the lowest unoccupied molecular orbital (LUMO), which is pinned by the Fermi level of the metal and hence becomes partially filled (turns into SOMO). Adding another electron to it, or removing one (adding a hole) is blocked by the Coulomb repulsion, which leads to the splitting of the orbital in dI/dV spectra. Such pinning of a molecular orbital

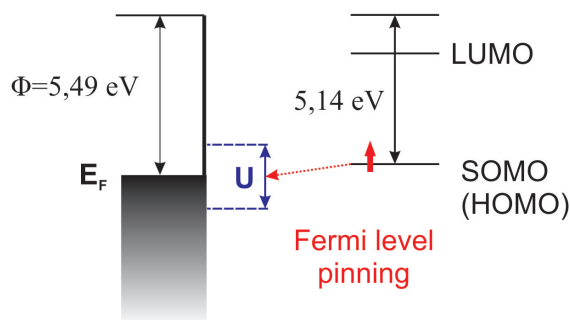


Figure 3.14 – Energy levels comparison for Pd(111) surface (from Figure 3.13) and NMTD molecule (from DFT calculation in vacuum).

becomes only possible if its energy with respect to vacuum is similar to the workfunction of the host metal.

In order to explore the possibility of a similar effect in the case of NMDT on Pd(111), the energy levels of the molecule were calculated in vacuum by density functional theory (DFT) and compared to the experimentally obtained work function of Pd(111). The latter one could be extracted by fitting the current dependency on approaching distance, as shown in Figure 3.13 (a). Its mean value after a series of measurements using a histogram plot and Gaussian fit (Figure 3.13 (b)) was established to be 5.49 eV.

Ab initio DFT calculations were performed by Rico Gutzler with the ORCA 3.0.3 electronic structure program package using a hybrid functional. NMTD molecule was relaxed in vacuum to a doublet state, since the nitronyl-nitroxide radical is supposed to retain an unpaired electron. The highest occupied orbital (containing one electron) was found to be at 5.14 eV with respect to vacuum. Figure 3.14 shows that both energies - the Fermi level of Pd(111) and the SOMO of NMTD - are positioned close to one another, which might lead to the pinning effect during adsorption and, therefore, to splitting of the partially occupied orbital by coulomb repulsion.

The calculations also demonstrated, that the unpaired electron is localized around the O-N-C-N-O part, which is in agreement with the previous investigations. [74] Note that the next "free" orbital (LUMO) was found to be positioned around 1.93 eV in respect to vacuum, which is more than 3 eV from the singly occupied orbital and so it has much less chance to be pinned by the Fermi level of the metal.

The latter considerations to some extent, also explain the shifting of the broad peaks observed in dI/dV spectra for various molecules. Coulomb repulsion depends on hybridization of

the molecular orbital with the Fermi sea of electrons in metal and may be different for every adsorption geometry. The stronger the hybridization, the lower the splitting energy. This might also explain the changing of the half width at half maximum parameter for the observed zero bias anomalies: The Kondo temperature is dependent on the charge transfer and hybridization of the singly occupied state with the conduction electron bath. With increasing hybridization, the Kondo temperature should also increase, hence, it will be higher on the quite reactive palladium surface than on the noble gold, what is in agreement with our observations.

Typical dI/dV spectra of NMTD on Co islands on Cu(111) show a relatively broad dip with step-like features. It can be assigned to inelastic excitations in the molecular backbone. However, the infrared spectra of molecules with the nitronyl-nitroxide radical usually display characteristic NO and CN bond vibrations at rather higher energies: 0,169 eV and 0,275 eV correspondingly. [76] The authors of Ref. [81] have seen a similar behavior for a molecule, consisting of 4 benzene rings and assigned steps at 66 and 118 mV to their vibrational modes (Figure 3.15). Pronounced asymmetry of the d^2I/d^2V signal was contributed to interface defects. Note, the discussed spectroscopic features can not be assigned either to spin excitations, or to Ruderman-Kittel-Kasuya-Yoshida (RKKY) interactions between the molecule and cobalt, since the energy range for such processes is on the order of several meV. [82] [83]

In summary, the investigated organic compound showed quite interesting behavior on two different substrates, which is most likely due to complicated electron transport; vibronic excitations, molecular orbitals and Kondo screening are involved.

3.4.2 Outlook: NMTD chains on Cu(111)

In addition to experiments on an isolated 1/2 Kondo system, as NMTD, it would be interesting to probe the interaction between several coupled impurities. When evaporated on Cu(111) surface in a substantial amount, NMTD molecules start to form chains, like those shown in Figure 3.16. Most likely, the bonding occurs via the cyano groups at both ends of the molecular backbone, which was already observed before for many types of organic compounds. Such system represent promising specimens for studying correlated electron behavior.

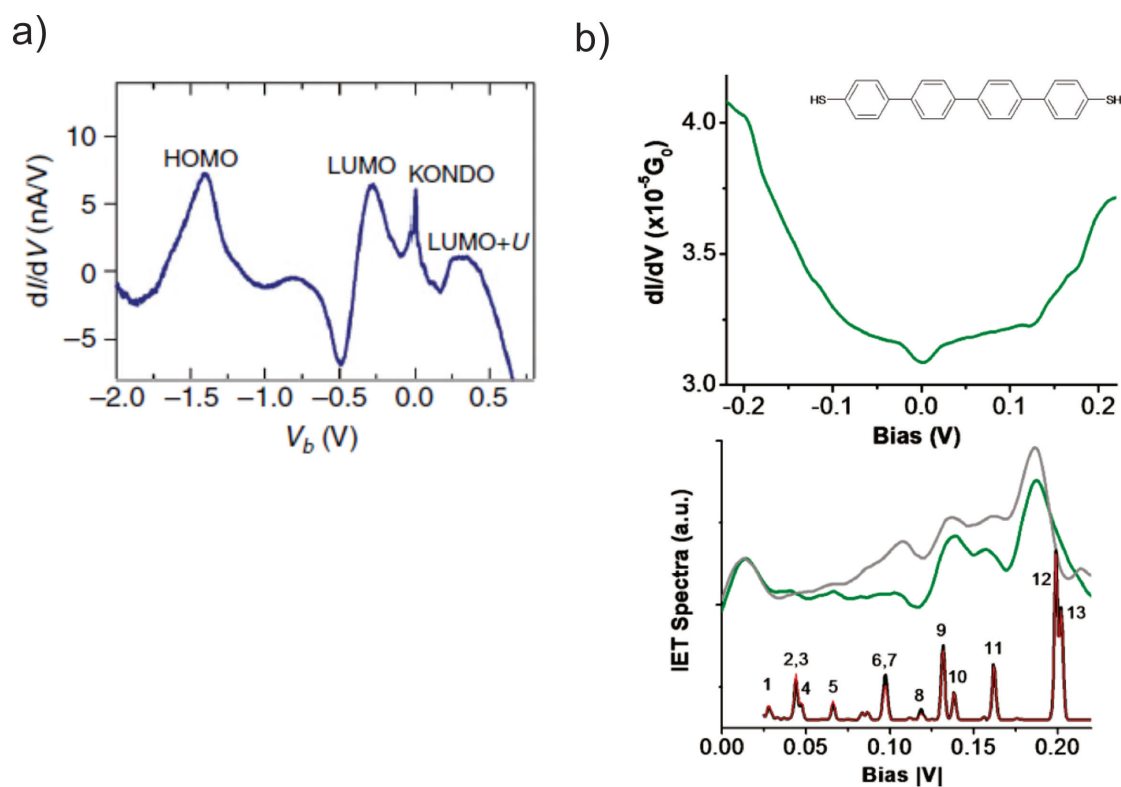


Figure 3.15 – a) dI/dV spectrum from Ref.[65]. The lowest unoccupied molecular orbital is split into two symmetric peaks and the Kondo resonance appears in the middle. b) dI/dV , d^2I/d^2V and spectra from Ref.[81] containing the vibrational modes of four benzene rings.

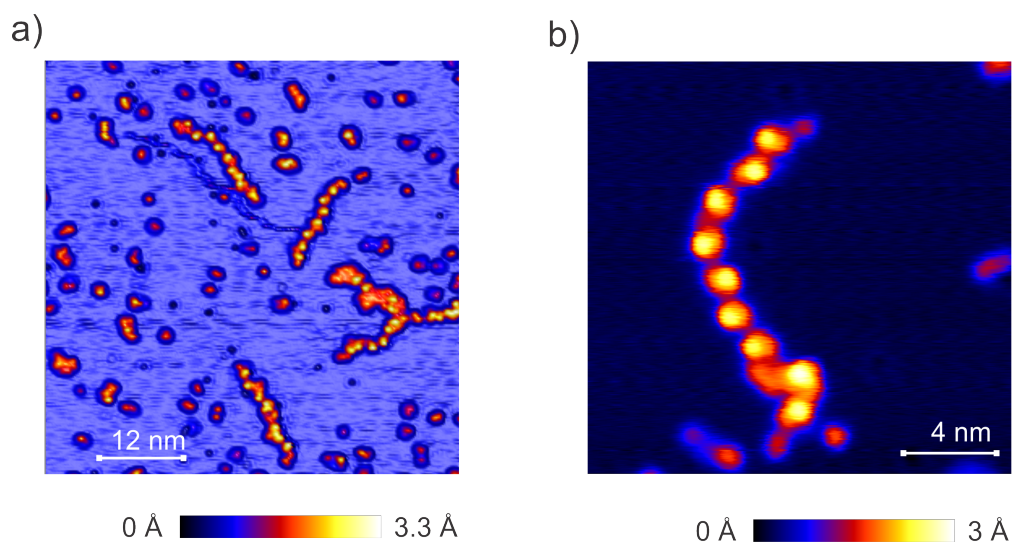


Figure 3.16 – Chains of the NMTD molecule on Cu(111).

4 STM imaging of sequence controlled polymers

4.1 Introduction

Sequence controlled polymers (SCP) have recently attracted great interest in academic and industrial research and were proposed to be the next "holy grail" in polymer science, due to their miscellaneous tunable properties.[29] One of the possible applications is information storage in the polymer sequence.[84] Moreover, just as nature does in polypeptides, SCPs could encode a secondary molecular structure, which could be used to further define the molecular functionality.

Due to the recent developments in chain-growth and step-growth polymerization methods, SCP synthesis could be automated using fast and large-scale procedure, allowing one to store and copy significant amount of molecular binary code.[85] A long oligomer sequence consisting of just two different monomers, which are associated with «0» and «1» bits is the most canonical method to realize an SCP. The read-out procedure of such a memory device presents a challenge similar to the sequencing of DNA or proteins. Since an amplification by the polymerase chain reaction, for example, is not available, it requires an ultra-sensitive analytical methods such as tandem mass spectrometry (MS/MS) [86], liquid chromatography–mass spectrometry (LC-MS) [87] or membrane ion channel blockade [88]. For practical applications in data storage, these types of analysis seem to be rather inconvenient, since a substantial amount of the species is needed and the result is an ensemble-averaged value. In contrast to these, scanning probe techniques are known for providing structural resolution of polymers at the single molecule scale [89] and can be a useful tool for exploring the secondary structure of an SCP. Despite the fact that the slow readout associated with scanning probe techniques limits their usage as an industrial read-out technology, their mapping abilities at the single molecular level are crucial for understanding the fundamentals of polymers behavior on surfaces.

The order of monomers in the chain can dramatically influence the properties of the whole molecule. This effect will depend strongly on the chemical structure of the monomers itself. Similar to the principle by which protein function is derived, a structural motif may cooperatively generate a property, that goes beyond the sum of the individuals. Examples in nature are manifold; the conductivity behavior of DNA, dependent on the sequence of bases and their stacking, varies from insulating to nearly ohmic (although the latter point is still controversial).[90]

The electronic properties of molecules adsorbed on a surface can be precisely unveiled by means of low-temperature scanning tunneling microscopy (STM). The great advantage of this technique is its sub-nanometer spatial resolution, which allows precision probing of the occupied and unoccupied molecular orbitals of single species.[91] Moreover, by means of STM one can repeatedly switch between two different regimes like tunneling and transport at various positions, or deliberately induce chemical reactions.[92]

4.2 Background

4.2.1 Oligo triazole amides (OTA)

This chapter presents an investigation of short SCPs - oligotriazole amides (OTA) trimers. Their whole family consists of 8 permutation triples of «0» and «1» monomers (presented in Figure 4.13). The experimental investigation will concentrate mainly on the three species: «000», «011» and «010». We analyze the STM data with respect to the OTA's potential applications as an information storage platform or secondary structure encoding. In addition, a possibility of polymer crystal formation on the OTA basis will be discussed.

The OTA trimers considered here were synthesized by repeating cycles of amidification and copper-assisted alkyne-azide cycloaddition reactions (in the group of Jean-Francois Lutz from the Charles Sadron Institute in Strasbourg). [93] A Wang resin was used as a solid support.

Two types of monomers were added as building blocks in a trimer sequence. The difference between monomer encoding a «0» or a «1» is the presence of one methyl group. Both monomers are separated from each other by a spacer moiety consisting of a 1,2,3-Triazole.

4.2.2 Electrospray ion beam deposition

One of our aims is to study these oligomers with the perspective to decode their sequence of monomers or find a structure-sequence relation. Hence, exploration of an extended conformation is necessary and will allow us to potentially achieve both goals simultaneously. For that purpose we decided to use low temperature (LT) STM, performing at 4K. Cooling down

4.2. Background

Binary assignment	Structure	Calculated [M+H] ⁺
000		695.372
100		709.388
010		709.388
001		709.388
110		723.403
011		723.403
101		723.403
111		737.419

Figure 4.1 – Chemical structure of the oligotriazole amide (OTA) trimers from the Ref.[93]. Red colored - monomer «0», blue colored - monomer «1».

Chapter 4. STM imaging of sequence controlled polymers

with liquid helium increases the stability of the microscope and reduces the contamination of the surface by residual gases. This method requires the OTA to be deposited on a substrate in ultra high vacuum (UHV) conditions. However, the molecules are non-volatile, which prohibits their thermal evaporation. With this in mind, a technique like electrospray ion beam deposition (ES-IBD) is used here to prepare the samples for subsequent STM analysis. [94]

An overview sketch of the ES-IBD method is presented in Figure 4.2. The instrument consists of various differential pumping stages connected through thin 2 mm apertures, with the pressure decreasing from atmospheric at the emitter down to the ultra high vacuum (10^{-10} mbar) at the sample stage. A solution with the required organic compound is dispersed into an aerosol of charged droplets that evolves into a molecular ion beam, which is then guided through the differentially pumped chambers by means of ion optics. Upon arriving at the sample surface, which is usually a metallic single crystal, the molecules adsorb and can later be characterized by means of the STM.

Each investigated oligomer was dissolved in methanol at a concentration of 0.1 mmol/l. The solution was then fed to the emitter, where a voltage of approximately 5 kV was applied to the metallic needle. The high electric field between the emitter and counter electrode causes the formation of a so-called Taylor cone at the thin end of the emitter, where the solution expands into an aerosol because of the instability of liquid and its decay into charged droplets. The droplet size decreases drastically due to evaporation down to the charged molecular clusters.

The established ion cloud enters the first chamber (0.5 mbar) through the thin capillary and is directly collimated by the ion funnel. At the next stage two rf-quadrupoles are installed to achieve collisional cooling and mass selection during deposition, so that only the intact molecules of interest arrive at the sample. The beam is guided further by electrostatic lenses and steering plates. In the next chamber, pumped down to the high vacuum range (10^{-7} mbar) a time-of-flight mass spectrometer (TOF-MS) is connected, which is a powerful tool for chemical characterization of the beam compounds and allows one to check its purity before and after the deposition. For monitoring the kinetic energy of the molecules, a retarding grid detector is installed. In the last chamber, which maintains UHV conditions (10^{-10} mbar) a sample on a movable stage is positioned perpendicular to the beam. Directly after the deposition, the sample can be transferred *in-situ* to an STM, operating at room temperature, or to a vacuum suitcase. During the deposition the soft landing of molecules is ensured by a bias deceleration voltage applied to the sample.

A Cu(100) single crystal was prepared by the standard UHV procedure of sputtering and annealing cycles. It was sputtered by argon (Ar^+) ions with 1 kV beam energy for 30 minutes and annealed up to 800 K.

The transfer from ES-IBD to the LT-STM cannot be achieved at atmospheric pressure, due

to adsorption of contaminants. For maintaining a UHV environment, a vacuum suitcase is needed. It consists of a small vacuum chamber, a manipulator and a battery powered ion-getter pump. This provides the necessary mobility and allows one to move the prepared sample between different instruments. The transfer procedure is realized through pumped load-locks, which are installed at the vacuum chamber of the ES-IBD and the STM.

electrospray ion beam deposition

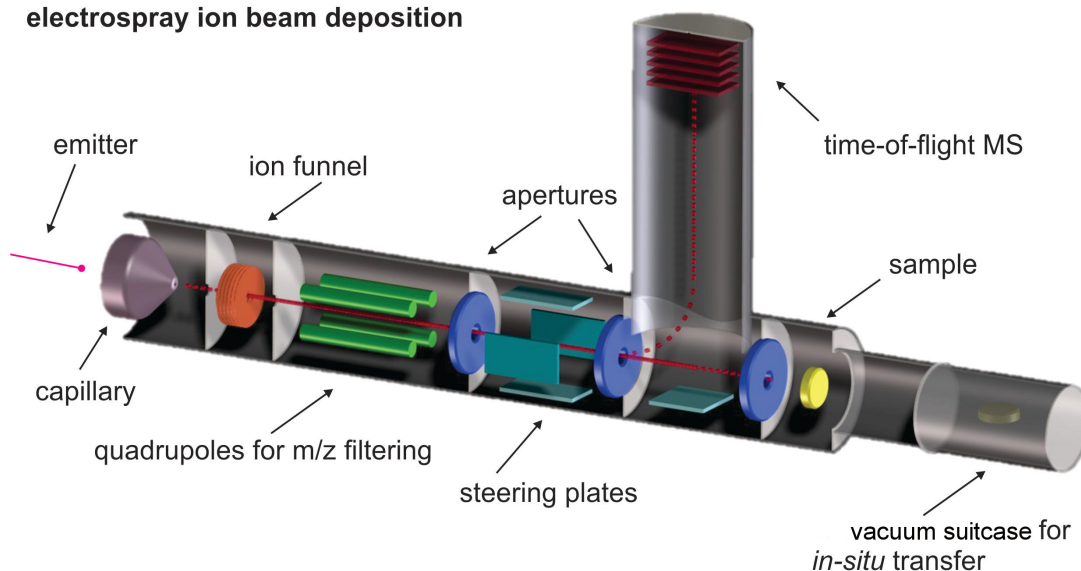


Figure 4.2 – Schematic of the electrospray ion beam deposition apparatus. The molecular ion beam (red line) is passed through a series of differentially pumped chambers by means of ion optics

The STM measurements presented in this chapter were performed on the set-up described in Chapter 1.

4.3 Results and discussion

4.3.1 Mass spectrometry of OTA trimers

First, a mass spectrometry analysis of the solution was performed in order to establish a protocol for a stable ion beam deposition. Mass spectra of three OTA: «000», «011» and «010» were measured with a commercial single quadrupole mass spectrometer (Agilent 4840), which is modified with a home built nanospray source [95]. The spectra are presented in Figure 4.3 (b). Each spectrum only contains a peak corresponding to the intact molecule. The difference between the molecular peaks ($M+H^+$) of the different OTA sequences are multiple of 15 u/e corresponding to the differing number of methyl groups or, in our "bitwise" analogy, «1» monomers. In addition, signals of singly charged sodium ($M+Na^+$) and potassium ($M+K^+$) ion adducts were detected, which are typical contaminations in ESI. Right before deposition

we also took reference mass spectra in the time-of-flight mass spectrometer (Figure 4.3 (a)) inside the ES-IBD instrument, in order to ensure the purity of the deposited species and confirm the mass selection of the intact molecular peak.

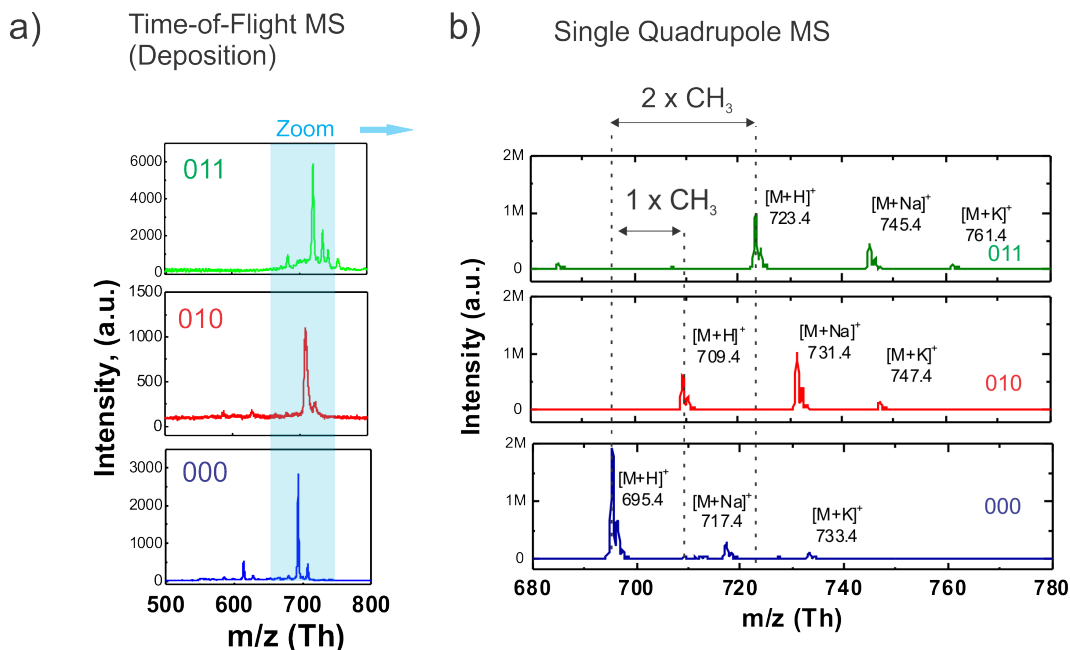


Figure 4.3 – Mass spectrometry of three OTA oligomers taken just prior to the deposition with the time-of-flight mass detector (a) and zoom into the area shown with a single quadrupole mass spectrometer (b).

4.3.2 STM topography of OTA trimers

We deposited four OTA species separately: «011», «010», «000» and «111». A typical STM survey scan after deposition is presented in Figure 4.4 (a). The surface contained a large number of adsorbates. Nevertheless, we are able to unambiguously identify at least two classes of conformation for each oligomer, whereas 40 % of the molecules appear to take a random configuration. The apparent height of these conformations is about 1.5 nm and only exhibits a small spread. Figure 4.4 (b) presents STM topographies of the «011» oligomer, which we associate with the first (upper) and second (lower) conformation. Each of them appears to have two mirror symmetries on the surface. The same was found for other two species, the «010» and «000». The characteristic length of all conformations is around 3.5 nm, whereas the fully extended molecule is expected to be approximately 4.5 nm long. The unidentified species, which could not be included in any of two conformation classes, had a similar size of about 3 - 3.5 nm and the same apparent height of 1.5 Å. Apart of that, big clusters of adsorbates approximately 5 x 5 nm were observed. Their apparent height varies from 1.5 to 2 nm. The «111» oligomer showed much a larger variety of conformations than the three other OTA

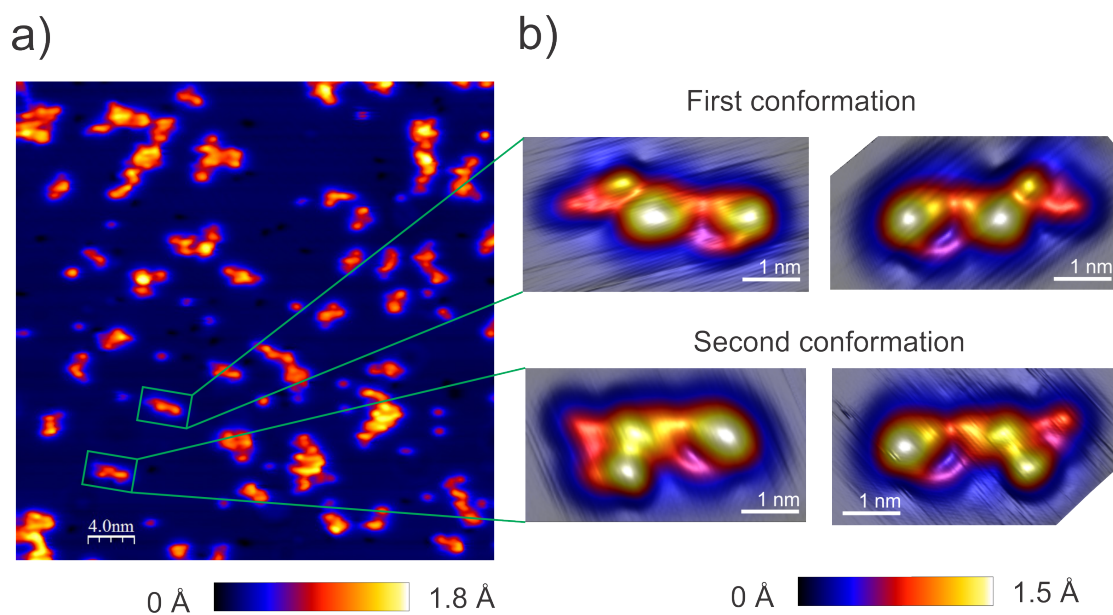


Figure 4.4 – STM topography of the «011» oligomer deposited on Cu(100). a) Survey scan b) The two different conformations with two mirror symmetries each.

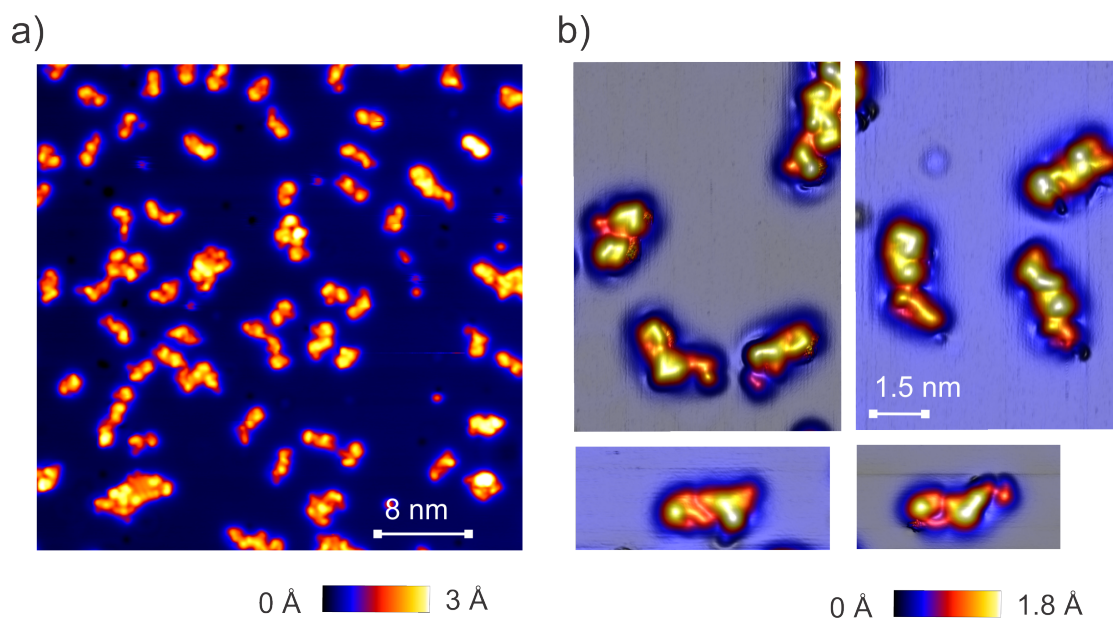


Figure 4.5 – STM topography of the «111» oligomer. a) Survey scan. b) Zoom into different conformations.

species. A typical STM topography is presented in Figure 4.5. Some of the foldings have certain similarities to the second conformation of the «011» and «010» oligomer, with the same size and apparent height, but also have more tangled internal structures.

The two bright spots, observable in both conformations of each oligomer might correspond to the 1,2,3-triazole, since nitrogen is well known to have a higher electronegativity than, for example, carbon. Nitrogen atoms would consequently have a higher electron density around them and may appear with bigger apparent heights in STM topography. This was confirmed by the STM tip manipulation of the «011» oligomer, presented in Figure 4.7 (c), where the extended molecule is comparable to its chemical model. This also suggests that all investigated oligo triazole amides are most likely folded on the Cu(100) surface by default. In Figure 4.6, the second conformation of all OTA is presented for comparison. Interestingly, the «011» and «010» species seem to be almost identical, while the «111» and «000» are somewhat distinct.

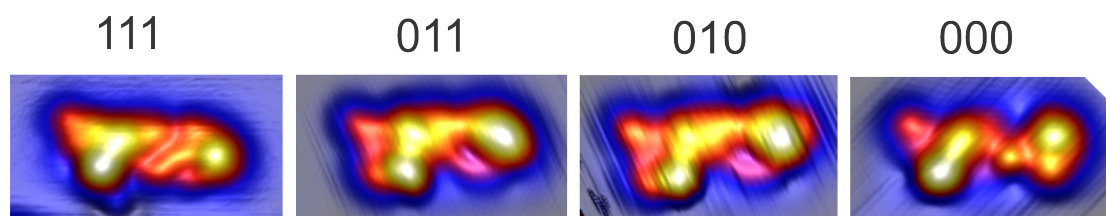


Figure 4.6 – Second conformation of the three oligomers: «011», «010», «000» and «111».

4.3.3 Analysis of the STM topographies

The obtained STM scans did not reveal the exact folding of the oligomer and, in addition, there seems to be tiny differences even between the molecules of the same conformation. In order to gain a better understanding of how the different species fold on the surface, we performed a quantitative analysis of the data.

First, a coordinate system was defined through each molecule, taking the two largest bright spots as fixed points for the X axis. This was necessary for the subsequent comparison of different conformations and oligomers. Then, we selected five characteristic points on all three OTA. Figure 4.8 shows an example of the procedure for the second conformation of the «011» oligomer. The coordinates of these feature-points can be compared for different molecules, so for that purpose all representable STM topographies with sufficient resolution were cut to the same frame size of 4 nm x 2.2 nm, and aligned in such a way that the X axis is horizontal (see Figure 4.9). For the zero coordinate, the first big bright spot was selected.

In Figure 4.9 the characteristic points of the investigated molecules are plotted separately for each type of OTA molecule and its two conformations - the first (a) and the second (b).

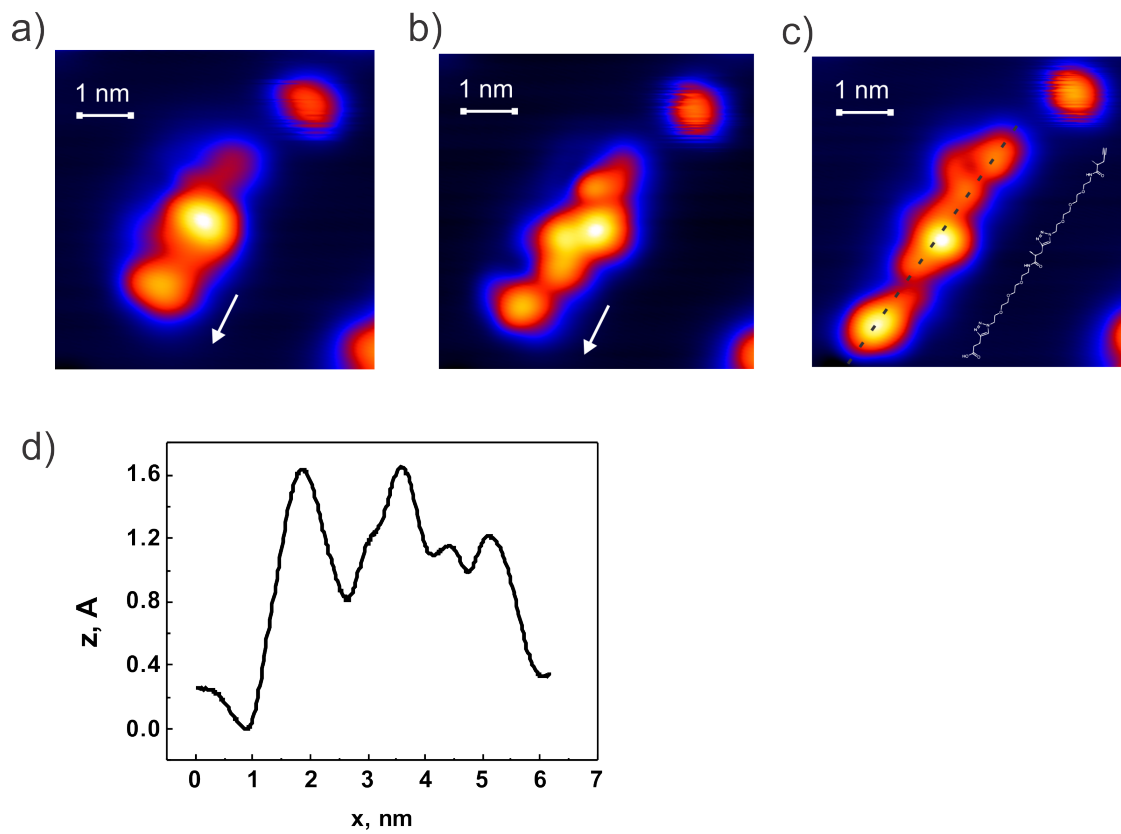


Figure 4.7 – a)-c) Manipulation of the «011» oligomer by the STM tip. d) Height profile of the extended oligomer.

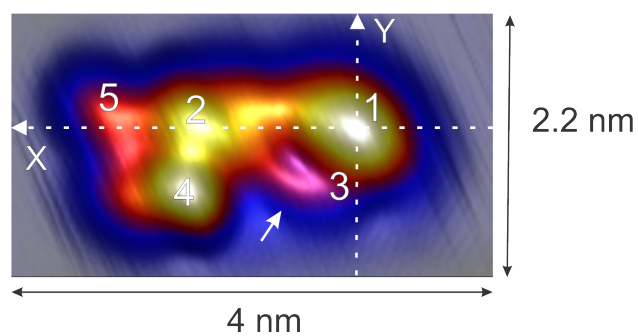


Figure 4.8 – Axis definition through a «011» molecule of the second conformation. Characteristic points are numbered. The small arrow points towards the "ring" structure.

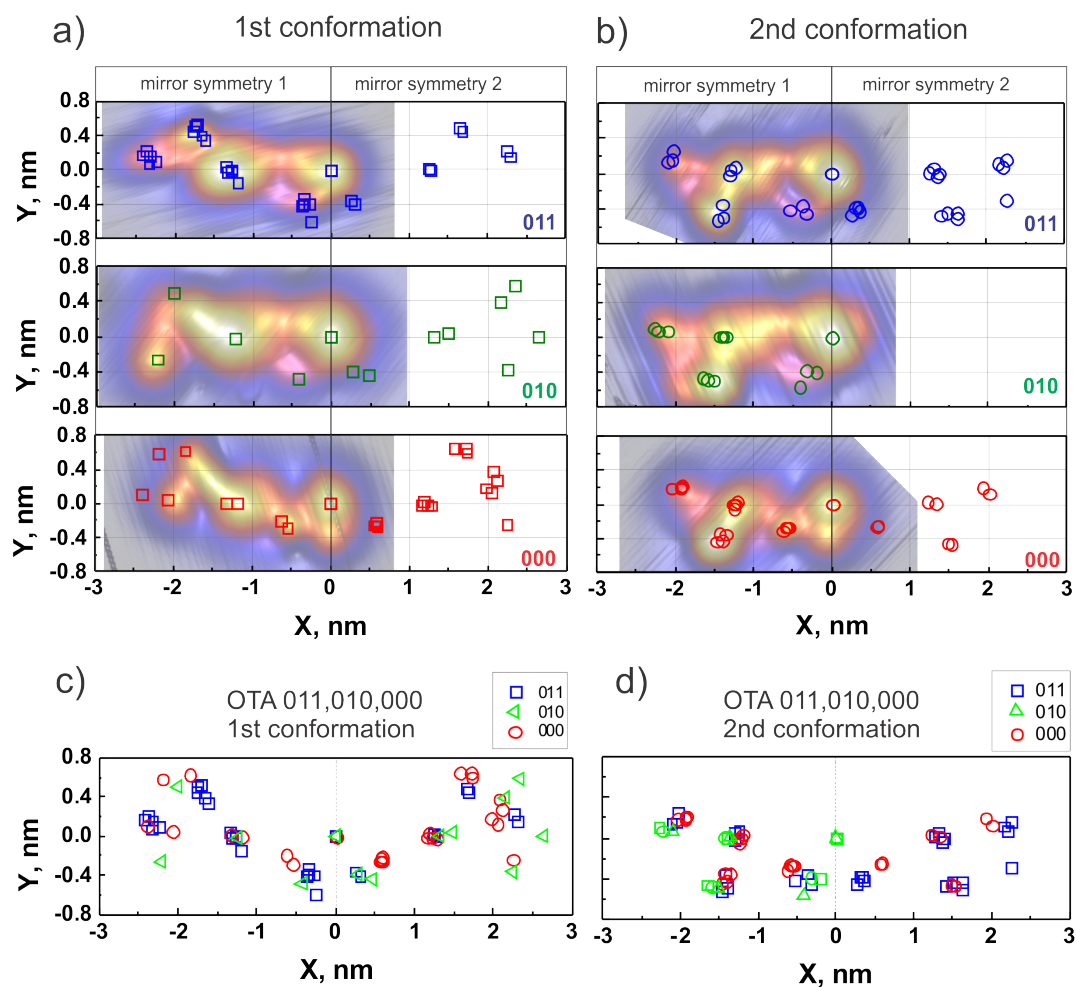


Figure 4.9 – Analysis of the STM data. a), b) First and second conformation of all oligomers. c) First conformation of all deposited OTA. d) Second conformation of all deposited OTA.

Note that each of them has also two mirror-symmetrical versions, which is most likely due to a racemic mixture of the molecule itself, being present on the surface. The positions of the characteristic points lie close to one other for all three OTA, however small differences are observable. Comparisons of the first and second conformations are presented in the (c) and (d) graphs, respectively. The former shows a larger spread of the characteristic points for the «000» and «010» oligomers, which might indicate that the first conformation is more flexible on the surface and, additionally, that the folding of the oligomer chain is apparently influenced by the number of CH_3 groups.

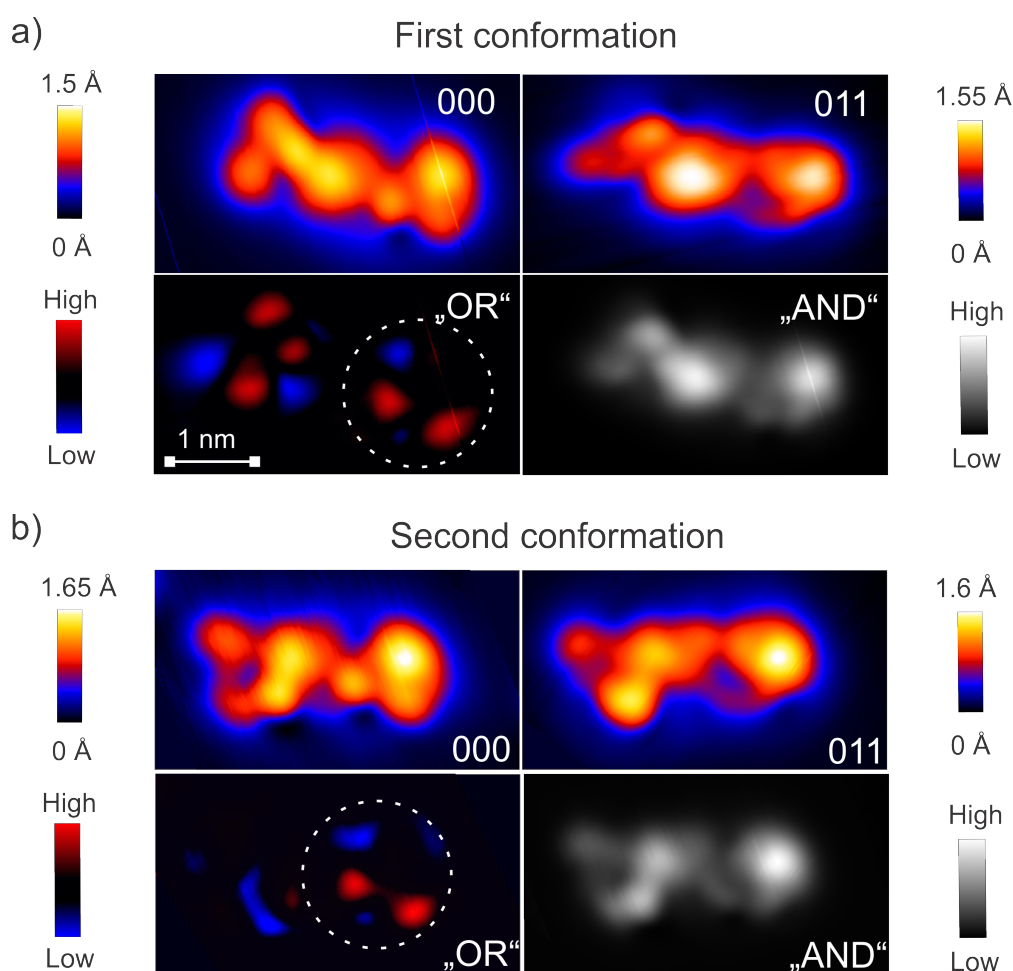


Figure 4.10 – Analysis of the STM data of two oligomers: «000» and «011». "OR" map represents differences between topographies, "AND" map - similarities. a) First conformation. b) Second conformation. The white dashed ellipse indicates same differences for both conformations.

As mentioned above, the «1» monomer differs from the «0» by just one methyl group. We hypothesize that this rather small difference is influential to the oligomer folding. The OTA trimers with a CH_3 group in the middle of the chain show a «ring» like feature in the STM topography close to the center of the molecule. We took the onset of this ring as the second

characteristic point in our analysis. In the case of «000» oligomer, no such feature was observed in any conformation. The methyl group from the third «1» monomer in the «011» case is positioned close to the end of the whole molecule and can increase its stiffness. This explains the relatively small spread of characteristic points for the tail of the «011» species. For the «000», the methyl group is absent, and hence the larger spread of the corresponding points of the tail is observable.

To visualize these variations, we performed a subtraction between the STM topographies of different oligomers with the same conformations, in order to separate the regions where differences or common features are depicted more pronouncedly. For this, all topographies had to be aligned, which was possible due to the already introduced coordinate system; the zero XY points of axes needed to be collocated. Prior to subtraction each image pair was brought to the same resolution by extrapolation. In Figure 4.10, difference and equality maps between «011» and «000» oligomer are presented for both conformations separately. It shows clearly that the similarities dominate over the whole molecular backbone, whereas the differences are minor and spread over the edge: at the position of the "ring" offset (since it exists only in the «011» oligomer) and around the thin tail, because the latter one seems to become more flexible in the «000» molecule and constantly changes its alignment. Difference maps of the first and second conformations show common features, marked with the dashed white ellipses. Later, these differences will be compared to a molecular model for testing its validity.

4.4 Conclusions

4.4.1 Summary

This work demonstrated the possibility of electrospray ion beam deposition of the four oligo triazole amides: «111», «011», «010» and «000». All exhibit folded structures on the Cu(100) surface. The latter three oligomers show two major classes of conformation, whereby the «111» is the least compact one and appears to have many different foldings.

Additionally, molecular dynamics calculations of OTA were performed by Ludger Hanau using the GROMACS software package. The dominating structure was found to be most likely the lamellae conformation, which was already observed for many types of polymers. Figure 4.11 shows a possible folding happening at the location of the flexible NH-group in the middle of each oligomer. Such lamellae structure could be additionally stabilized through a "single-hairpin" - a hydrogen bonding, which arises between the OH-group at one end and an oxygen atom on the other (shown as a dashed blue ellipse). This version of folding also explains the dominating similarities of the molecular backbone between the different oligomers, since

the position of the 1,2,3-triazoles does not vary. Apparent positions of the methyl groups are shown in red circles.

Finally, our STM data demonstrate that the decoding of monomer sequence stored in oligomers such as OTA is not a trivial task, since the molecules prefer to fold on the surface and read-out procedure requires at least an additional manipulation by the STM tip. Nonetheless, the research performed on OTA is interesting in terms of lamellae polymer folding, which is used by nature in a variety of compounds.

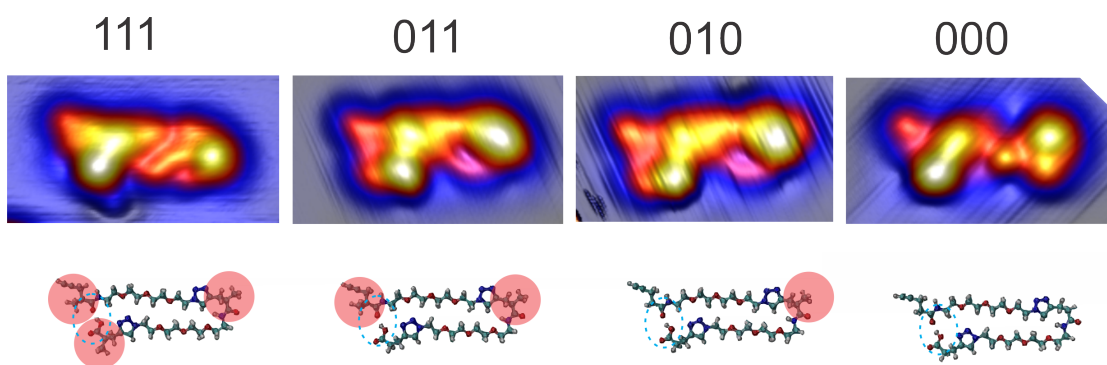


Figure 4.11 – Possible lamellae types of OTA folding. Models of each oligomer are shown in comparison with corresponding STM topographies. Hydrogen bonding between the oxygen atom and the OH-group at opposite ends are marked with dashed blue ellipses. Apparent positions of the methyl groups are painted orange.

Lamellae are the main type of long-range order for polymer crystals, but the exact reasons and preconditions for it are not well understood. [96] Moreover, the crystallinity of a polymer does not reach 100 % in most of cases, due to kinetic reasons - the longer the polymer chain is, the lower the probability that it can become disengaged in a melt and align perfectly during the crystallization procedure. The unique properties of bulk polymers, like ruggedness and the simultaneous flexibility, arise because of the combination of amorphous and crystalline regions. Figure 4.12 presents the lamellae crystalline and amorphous chain trajectories for polyethylene-like polymer. [2]

Intramolecular "hairpins", like the hydrogen bonding between the OH-group and the oxygen in the case of OTA, are crucial for lamellae formation and provide stiffness for polymer crystals. In addition, the size of the crystalline and amorphous phases could be pre-engineered by installing the so-called "assembling instructions" in the sequence of oligomers. [96]

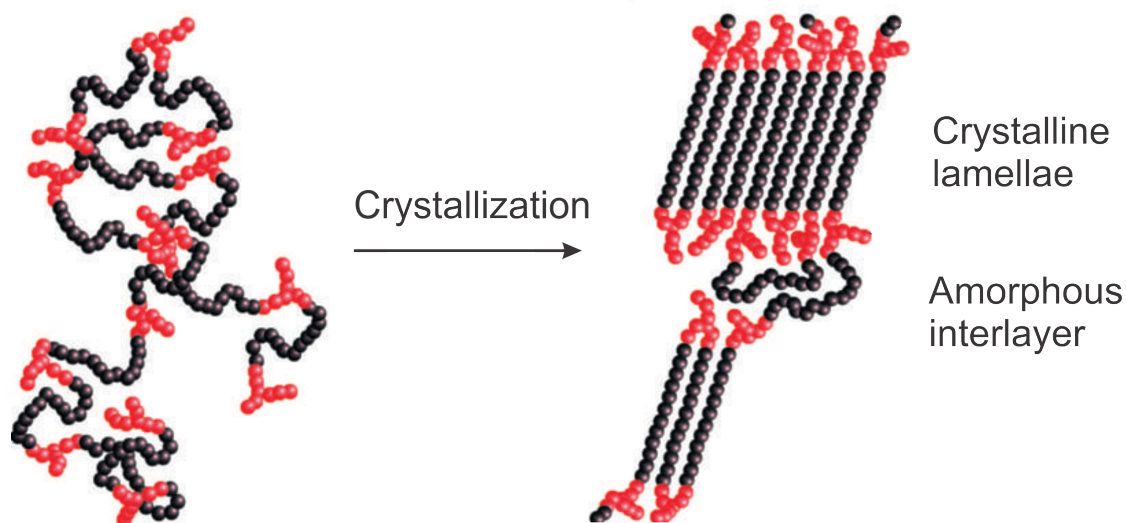


Figure 4.12 – A chain of polyethylene-like polymer before and after crystallization from Ref. [2]. Lamellae crystalline (ordered) and amorphous (disordered) regions are shown.

4.4.2 Outlook: OTA hexamers

For probing the lamellae formation we decided to study longer OTA sequences, since the 4 trimers discussed above showed simple two-folding (according to the molecular dynamics calculations). Generally, oligo triazole amides could be synthesized also as longer chains, containing up to 6 monomers. However, the synthesis procedure in this case seems to be more complex and the final product contains a mixture of molecules. We had a chance to test one initial sample. In order to verify the synthesis success, the 6 x «0» oligomer was deposited on Cu(100) surface by the ES-IBD technique described above.

In Figure 4.14 the time-of-flight mass spectrum is presented. It does not show the peak of the single ionized (protonated) «000000» oligomer, as observed for the trimers. Instead, a sequence of signals is observable, some of which could be assigned to the double ionized species (doubly protonated, for instance).

The obtained STM topographies demonstrated structures of different sizes (Figure 4.15). The shorter ones could be attributed to the smaller OTA sequences with lower mass, whereby the long structures seem to correspond to the intact oligomer with the ordered and disordered types of conformations. The ordered zig-zag like structures can be associated with the lamellae chain folding (marked with green circles). The lowest assembly (in Figure 4.15 a)) shows an amorphous interlayer between two crystalline regions. In the (c) part an STM topography of the ordered lamellae structure with 5 stacks is presented.

Since the usual STM scans do not provide a direct insight into the primary structure of the

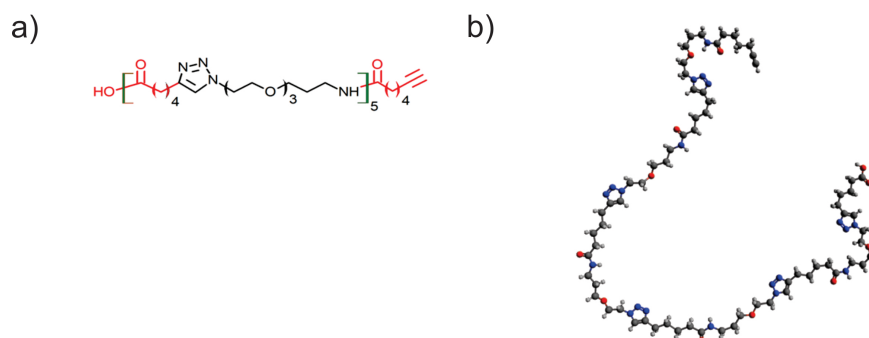


Figure 4.13 – a) Chemical formula of the 000000 oligomer. b) Possible vacuum conformation. The total length of the hexamer is about 9 nm.

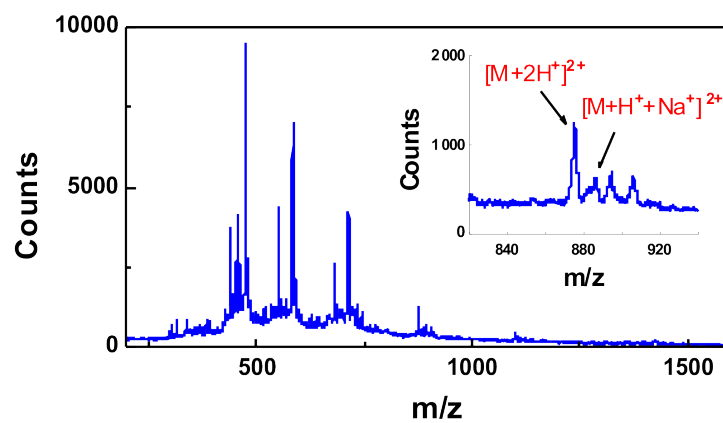


Figure 4.14 – Time-of-flight mass spectrum of the «000000» oligomer. A complicated sequence of peaks is observable. Inset - zoom into a smaller range with a doubly protonated peak.

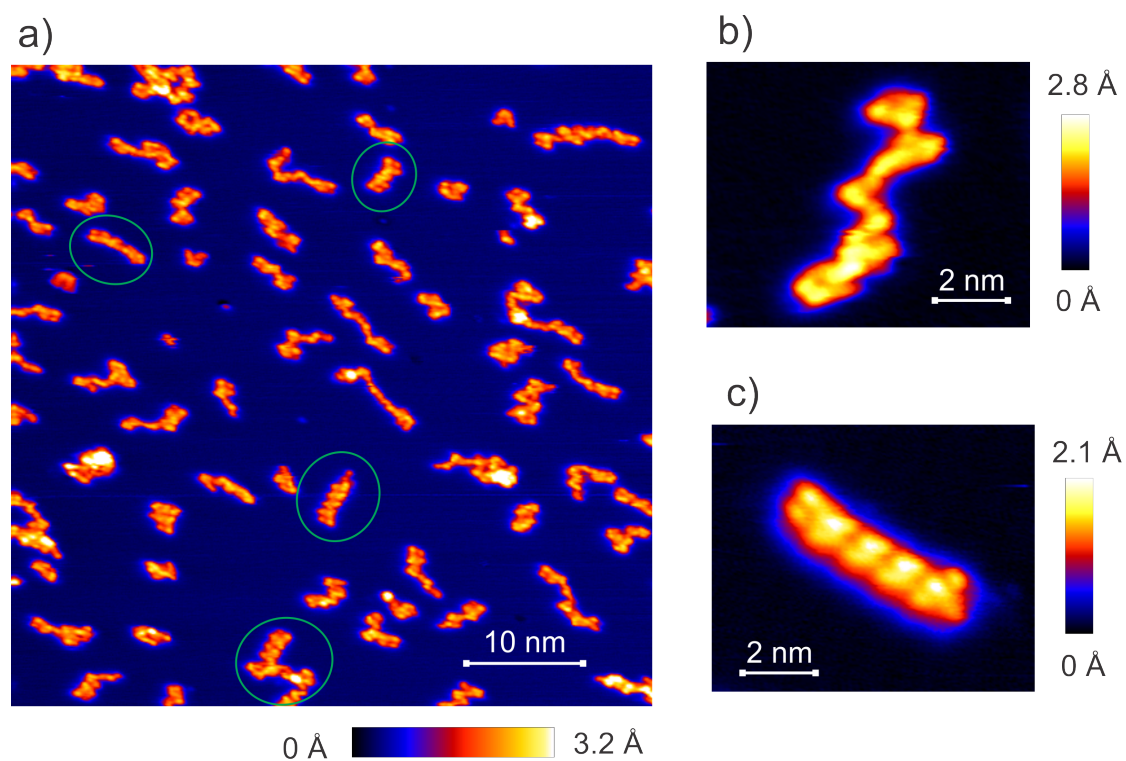


Figure 4.15 – STM topography of the «000000» oligomer. a) Survey scan. Apparent lamellae structures are marked with green circles. b) Zoom into a disordered conformation. c) Zoom into a lamellae conformation.

investigated oligomers, one can think about possible ways of pushing the resolution limit further. A well-known method is to modify the tip-apex by picking up a surface impurity (most likely a CO molecule) [97], which results in much more intricate STM topography. A comparison between scans on «011» oligomer done with "usual" and "high-resolution" tips is presented in Figure 4.16.

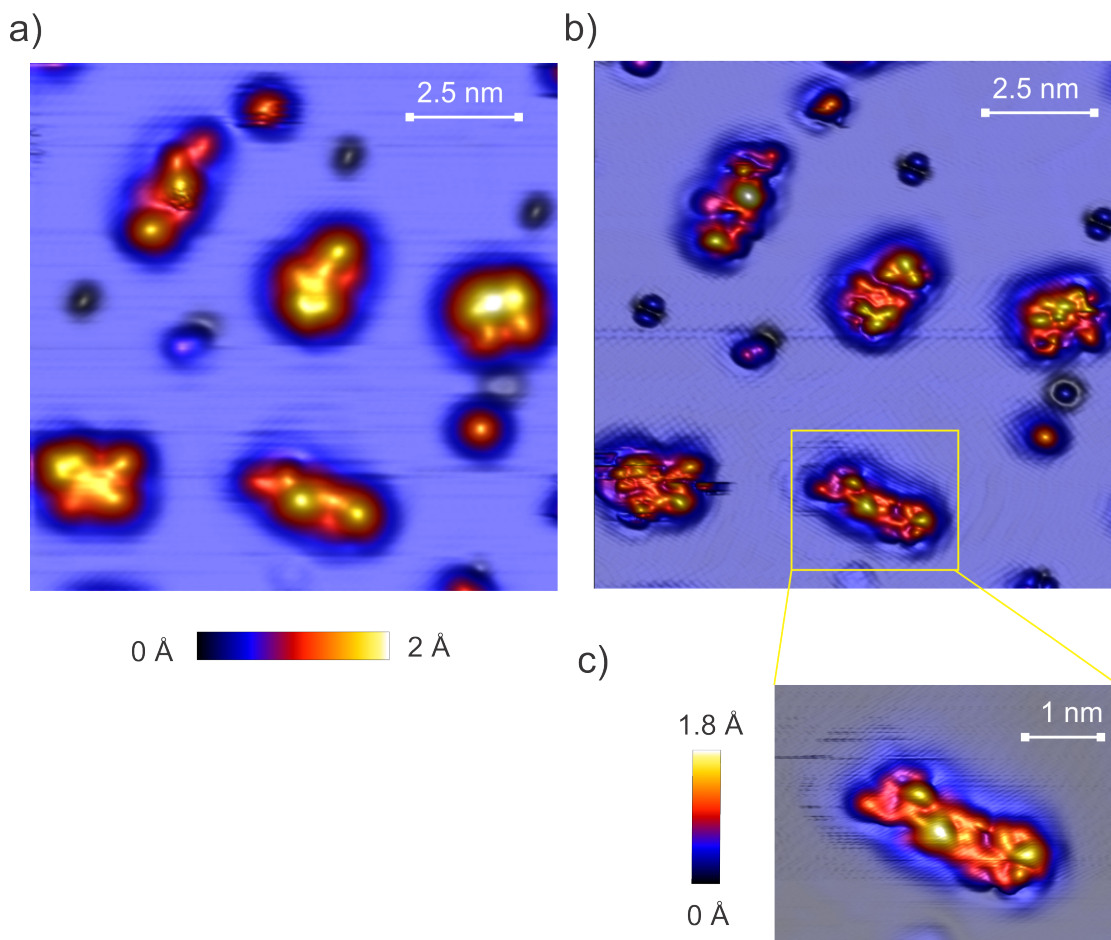


Figure 4.16 – STM topography a) - with a "usual" metallic tip. b) - with a functionalized tip. c) A zoom in a typical conformation of the "011" oligomer.

5 Summary and perspectives

In this thesis, I attempted to advance the field of molecular nanoscience on several important fronts. These included the examination of transmission channel composition in quantum point contacts by shot noise measurement, exploration of organic radical interaction with conductance band electrons in metals and understanding of polymer chain folding on surfaces. The low temperature STM was selected as the principal technique, since it is a unique tool in the research area of nanoscience and possesses an unprecedented ability to image and manipulate single atoms and molecules on surfaces. It is introduced in the first chapter where the experimental set-up is also described.

5.1 Quantum noise

The second chapter is dedicated to the combination of the STM with the quantum shot noise measurement. This complicated technique is necessary if one desires to explore the transmission channel matrix of a ballistic conductor, since it cannot be revealed by simple I/V characterization. Several test measurements are presented, which are necessary for verifying the detection circuitry for current and voltage amplification. All of them show perfect agreement with the corresponding theory and prove the ability of thermal- and shot noise detection with the selected amplifiers.

Concerning measurements on a quantum point contact, good agreement to the theory was achieved in the weak tunneling regime with the current amplification, although a background subtraction was necessary. In the case of voltage amplification, the obtained shot noise level appeared, however, lower than expected for the established conductance of the contact. Obstacles that appear on the way towards shot noise detection combined with the STM technique are discussed. Possible solutions, like, for instance, splitting the circuitry for the DC and AC current are suggested.

Limitations of the existing STM set-up, such as high noise background for current amplification and low transparency in the MHz range instigated the decision to design a new STM head. Upgraded with a low-temperature amplifier and low loss semi-rigid cabling, it should make shot noise measurements possible at frequencies up to hundreds of MHz.

5.2 Organic molecule with spin system 1/2: probing of quantum criticality

In the third chapter, a purely organic molecule (named NMTD) with spin system 1/2 was investigated on palladium and copper single crystals. The obtained data revealed complicated electron transport. The interaction between the molecular radical and the sea of conduction electrons led to a Kondo resonance, whose half width at half maximum parameter varied for different adsorption conformations. In addition, the splitting of the single occupied molecular orbital was observed due to the Coulomb interaction. These results were complemented by *ab initio* DFT calculations of molecular energy levels in vacuum.

The organic molecule with a nitronyl-nitroxide radical can be a perfect system for benchmarking tests of different theoretical models. As has been shown previously [1], after evaporation onto a Au(111) surface the NMTD molecule demonstrates a Kondo resonance with a Kondo temperature below 1.5 K, [1] whereas for other Kondo systems, like, for instance, single cobalt atoms on copper surface, the Kondo temperature is about 55 K [98]. The case of NMTD seems to be quite unique and allows one to probe the weak coupling of the unpaired electron of the molecule with the conduction electrons in metal.

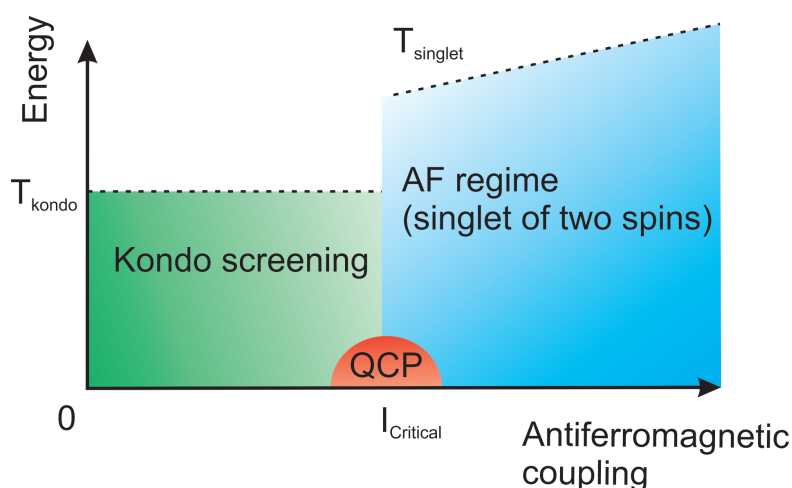


Figure 5.1 – Schematic phase diagram for the two impurity Kondo system. I_{Critical} - value of critical coupling between two impurity spins. T_{Singlet} - characteristic energy scale of singlet triplet excitation. T_K - Kondo temperature.

5.3. Sequence controlled polymers: the way towards molecular logic

The physics of quantum phase transitions has attracted great interest in recent years. Being unreachable directly in practice, the quantum critical point at zero temperature is thought to be the key to understanding many unexplained physical phenomena in correlated electron materials. [99, 100] One of the possible ways to come closer to it experimentally is the investigation of two impurity Kondo systems, where a certain competition between Kondo screening and magnetic exchange interaction occurs. Due to the rivalry of the mentioned effects, the system can be driven either into the common singlet state (two impurity spins that are antiferromagnetically coupled) or into the two separate Kondo singlets (two impurity spins screened by the conduction electrons). [101] As can be seen on the corresponding phase diagram (presented in Figure 5.1) the quantum critical point lies exactly between these two regimes.

However, the experiments conducted before on quantum dots [102, 103] or on magnetic atoms by means of the STM technique [104, 105] did not reveal a quantum critical behavior. In all cases only a crossover between the magnetic exchange interaction and the Kondo effect was obtained. The reason for this might lay in the strong coupling of the unpaired electron of impurity to the substrate. As was already proposed by theoretical investigations, [106, 107] one has to move towards Kondo impurities with much lower Kondo temperatures for revealing quantum criticality. For that, the NMTD molecule is a good candidate.

5.3 Sequence controlled polymers: the way towards molecular logic

In the fourth chapter the oligo triazole amides (OTA) are discussed. These molecules are considered as a new promising realization of sequence controlled polymers. They are synthesized out of two basis monomers (associated with "1" and "0"), which allows one to store binary information on the atomic scale. We demonstrate successful deposition of the OTA trimers (sequences of three monomers) on a sample surface by means of the electrospray ion beam deposition technique. Moreover, the subsequent STM analysis revealed several preferable foldings that happened most likely due to the "hairpin", as was also suggested by molecular dynamics calculations. The hydrogen bonding, which occurs between the oxygen atom and the OH-group, pulls both ends of the molecule together and enforces the formation of a lamellae structure. This is also observable at larger OTA molecules containing up to six monomers. The fact of the lamellae building is quite interesting – it proves that the OTA structures can appear as crystalline polymers.

Encoding a binary information in a polymer structure is just a first step towards the realization of molecular logic. Ideally, one would like to distinguish between various sequences of monomers not just by their appearance in the STM topography, but also by different electronic properties of the whole molecule. We showed, that adding just one methyl group can

Chapter 5. Summary and perspectives

change the adsorption conformation drastically. It would be quite interesting to compare vibrational energies or molecular orbitals of polymers with the same content but different order of monomers. Moreover, the correlation between structural sequence and, for example, conductance of a polymer can provide a basis for the development of logic gates.

Bibliography

- [1] Y.-H. Zhang, S. Kahle, T. Herden, C. Stroh, M. Mayor, U. Schlickum, M. Ternes, P. Wahl and K. Kern. Temperature and magnetic field dependence of a Kondo system in the weak coupling regime. *Nature Communications*, **4** (2013).
- [2] C. De ten Hove, J. Penelle, D. Ivanov and A. Jonas. Encoding crystal microstructure and chain folding in the chemical structure of synthetic polymers. *Nature Materials*, **3**, pp. 33–37 (2004).
- [3] R. P. Feynman. There's plenty of room at the bottom. *Engineering and Science*, **23**, pp. 22–36 (1960).
- [4] N. Taniguchi. On the basic concept of "nano-technology". *Proceedings of the International Conference on Production Engineering* (1974).
- [5] A. Aviram and M. A. Ratner. Molecular rectifiers. *Chemical Physics Letters*, **29**, pp. 277–283 (1974).
- [6] M. A. Reed, C. Zhou, C. J. Muller, T. P. Burgin and J. M. Tour. Conductance of a molecular junction. *Science*, **278** (1997).
- [7] L. A. Bumm, J. J. Arnold, M. T. Cygan, T. D. Dunbar, T. P. Burgin, L. Jones, D. L. Allara, J. M. Tour and P. S. Weiss. Are single molecular wires conducting? *Science*, **271** (1996).
- [8] K. E. Drexler. Molecular engineering: An approach to the development of general capabilities for molecular manipulation. *Proceedings of the National Academy of Sciences*, **78** (1981).
- [9] NSTC/CoT/NSET. *NNI supplement to the president's 2016 budget*. National Nanotechnology Initiative (2015).
- [10] C. Toumey. The man who understood the Feynman machine. *Nature nanotechnology*, **2**, pp. 9–10 (2007).

Bibliography

- [11] L. Bogani and W. Wernsdorfer. Molecular spintronics using single-molecule magnets. *Nature Materials*, **7**, pp. 179–186 (2008).
- [12] J. Hwang, M. Pototschnig, R. Lettow, G. Zumofen, A. Renn, S. Goetzinger and V. Sandoghdar. A single-molecule optical transistor. *Nature*, **460**, pp. 76–80 (2009).
- [13] C. Große, A. Kabakchiev, T. Lutz, R. Froidevaux, F. Schramm, M. Ruben, M. Etzkorn, U. Schlickum, K. Kuhnke and K. Kern. Dynamic control of plasmon generation by an individual quantum system. *Nano Letters*, **14**, pp. 5693–5697 (2014).
- [14] T. Carell. DNA as a logic operator. *Nature*, **469**, pp. 45–46 (2011).
- [15] W. R. B. Ben L. Feringa. *Molecular Switches*. Wiley-VCH (2011).
- [16] J. L. Zhang, J. Q. Zhong, J. D. Lin, W. P. Hu, K. Wu, G. Q. Xu, A. T. S. Wee and W. Chen. Towards single molecule switches. *Chem. Soc. Rev.*, **44**, pp. 2298–3022 (2015).
- [17] J. Borghetti, G. S. Snider, P. J. Kuekes, J. J. Yang, D. R. Stewart and R. S. Williams. ‘Memristive’ switches enable ‘stateful’ logic operations via material implication. *Nature*, **464**, pp. 873–876 (2010).
- [18] J. Cuevas and E. Scheer. *Molecular electronics: an introduction to theory and experiment*. World Scientific (2010).
- [19] S. J. van der Molen, R. Naaman, E. Scheer, J. B. Neaton, A. Nitzan, D. Natelson, N. J. Tao, H. van der Zant, M. Mayor, M. Ruben, M. Reed and M. Calame. Visions for a molecular future. *Nature Nanotechnology*, **8**, pp. 385–389 (2013).
- [20] A. Nitzan and M. A. Ratner. Electron transport in molecular wire junctions. *Science*, **300** (2003).
- [21] E. Loertscher. Wiring molecules into circuits. *Nature Nanotechnology*, **8**, pp. 381–384 (2013).
- [22] S. Loth, M. Etzkorn, C. P. Lutz, D. M. Eigler and A. J. Heinrich. Measurement of fast electron spin relaxation times with atomic resolution. *Science*, **329** (2010).
- [23] A. V. Balatsky, M. Nishijima and Y. Manassen. Electron spin resonance-scanning tunneling microscopy. *Advances in Physics*, **61**, pp. 117–152 (2012).
- [24] M. Dolev, Y. Gross, Y. C. Chung, M. Heiblum, V. Umansky and D. Mahalu. Dependence of the tunneling quasiparticle charge determined via shot noise measurements on the tunneling barrier and energetics. *Physical Review B*, **81**, p. 161303 (2010).

-
- [25] M. Reznikov, M. Heiblum, H. Shtrikman and D. Mahalu. Temporal correlation of electrons: Suppression of shot noise in a ballistic quantum point contact. *Physical Review Letters*, **75**, pp. 3340–3343 (1995).
- [26] R. Landauer. Many-channel Conductance formula. *IBM J. Res. Dev.*, **21**, p. 223 (1957).
- [27] H. van den Brom and J. M. Ruitenbeek. Quantum suppression of Shot Noise in metallic atomic size contacts. *Phys. Rev. Lett.*, **82**, pp. 1526–1529 (1999).
- [28] C. Beenakker. Quantum Shot Noise. *Physics Today*, pp. 37–42 (2003).
- [29] J.-F. Lutz. Sequence-controlled polymerizations: the next holy grail in polymer science? *Polym. Chem.*, **1**, pp. 55–62 (2010).
- [30] R. Young, J. Ward and F. Scire. The topografiner: An instrument for measuring surface microtopography. *Review of Scientific Instruments*, **43**, pp. 999–1011 (1972).
- [31] G. Binnig, H. Rohrer, C. Gerber and E. Weibel. Tunneling through a controllable vacuum gap. *Applied Physics Letters*, **40**, pp. 178–180 (1982).
- [32] G. Binnig, H. Rohrer, C. Gerber and E. Weibel. 7×7 reconstruction on si(111) resolved in real space. *Physical Review Letters*, **50**, pp. 120–123 (1983).
- [33] C. Toumey. 35 atoms that changed the nanoworld. *Nature Nanotechnology*, **5**, pp. 239–241 (2010).
- [34] D. Eigler and E. Schweizer. Positioning single atoms with a scanning tunneling microscope. *Nature*, **344**, pp. 524–526 (1990).
- [35] F. J. Giessibl, S. Hembacher, H. Bielefeldt and J. Mannhart. Subatomic features on the silicon (111)-(7 \times 7) surface observed by atomic force microscopy. *Science*, **289** (2000).
- [36] A. Bid, O. Nissim, H. Inoue, M. Heiblum, C. L. Kane, V. Umansky and D. Mahalu. Observation of Neutral Modes in the Fractional Quantum Hall Regime. *Nature*, **466**, pp. 585–590 (2010).
- [37] R. dePicciotto, M. Reznikov, M. Heiblum, V. Umansky, G. Bunin and D. Mahalu. Direct observation of a fractional charge. *Nature*, **389**, pp. 162–164 (1997).
- [38] E. Shpolsky. *Atomic Physics*. Nauka (1984).
- [39] J. G. Simmons. Generalized formula for the electric tunnel effect between similar electrodes separated by a thin insulating film. *Journal of Applied Physics*, **34**, pp. 1793–1803 (1963).

Bibliography

- [40] C. J. Chen. *Introduction to Scanning Tunneling Microscopy*. Oxford University Press (2008).
- [41] J. Bardeen. Tunnelling from a many-particle point of view. *Physical Review Letters*, **6**, pp. 57–59 (1961).
- [42] J. Tersoff and D. R. Hamann. Theory of the scanning tunneling microscope. *Physical Review B*, **31**, pp. 805–813 (1985).
- [43] K. Besocke. An easily operable scanning tunneling microscope. *Surface Science*, **181**, pp. 145–153 (1987).
- [44] J. Frohn, J. F. Wolf, K. Besocke and M. Teske. Coarse tip distance adjustment and positioner for a scanning tunneling microscope. *Review of Scientific Instruments*, **60**, p. 1200 (1989).
- [45] Y. Nazarov, editor. *Quantum Noise in Mesoscopic Physics. Proceedings of the NATO Advanced Research Workshop* (2003).
- [46] Y. Blanter and M. Buttiker. Shot Noise in Mesoscopic conductors. *Physics Reports*, **336**, pp. 1–166 (2000).
- [47] W. Schottky. Uber spontane Stromschwankungen in verschiedenen Elektrizitatsleitern. *Annalen der Physik*, **57**, pp. 541–567 (1918).
- [48] G. B. Herzog and A. van der Ziel. Shot noise in germanium single crystals. *Physical Review*, **84**, pp. 1249–1250 (1951).
- [49] G. Lesovik. Excess quantum noise in 2D ballistic point contacts. *JETP Letters*, **49**, pp. 592–594 (1989).
- [50] M. Büttiker. Scattering theory of current and intensity noise correlations in conductors and wave guides. *Physical Review B*, **46**, pp. 12485–12507 (1992).
- [51] M. Kumar, R. Avriller, A. Yeyati and J. M. Ruitenbeek. Detection of vibration mode scattering in electronic Shot Noise. *Physical Review Letters*, **108**, p. 146602 (2012).
- [52] Y. Yamauchi, K. Sekiguchi, K. Chida, T. Arakawa, S. Nakamura, K. Kobayashi, T. Ono, T. Fujii and R. Sakano. Evolution of the Kondo Effect in a Quantum Dot Probed by the Shot Noise. *Physical Review Letters*, **106**, p. 176601 (2011).
- [53] H. Birk, M. J. M. de Jong and C. Schönberger. Shot-noise suppression in the single-electron tunneling regime. *Physical Review Letters*, **75**, pp. 1610–1613 (1995).
- [54] N. Wiener. Generalized harmonic analysis. *Acta Math.*, **55**, pp. 117–258 (1930).

-
- [55] A. Khintchine. Korrelationstheorie der Stationaeren stochastischen Prozesse. *Math. Ann.*, **109**, pp. 604–615 (1934).
- [56] H. Nyquist. Thermal Agitation of Electric Charge in Conductors. *Phys.Rev.*, **32**, pp. 110–113 (1928).
- [57] J. Johnson. Thermal Agitation of Electricity in Conductors. *Phys.Rev.*, **32**, pp. 50–51 (1928).
- [58] A. van der Ziel. *Noise in Solid State Devices and Circuits*. Wiley, New York (1986).
- [59] R. J. Schoelkopf, P. J. Burke, A. A. Kozhevnikov, D. E. Prober and M. J. Rooks. Frequency dependence of shot noise in a diffusive mesoscopic conductor. *Physical Review Letters*, **78**, pp. 3370–3373 (1997).
- [60] H. Lee and L. S. Levitov. Current fluctuations in a single tunnel junction. *Physical Review B*, **53**, p. 7383 (1996).
- [61] W. de Haas, J. de Boer and G. van den Berg. The electrical resistance of gold, copper and lead at low temperatures. *Physica*, **1**, pp. 1115–1124 (1934).
- [62] J. Kondo. Resistance minimum in dilute magnetic alloys. *Progress in Theoretical Physics*, **32**, pp. 37–49 (1964).
- [63] V. Madhavan, W. Chen, T. Jamneala, M. F. Crommie and N. S. Wingreen. Tunneling into a single magnetic atom: Spectroscopic evidence of the kondo resonance. *Science*, **280** (1998).
- [64] M. Ternes, A. J. Heinrich and W.-D. Schneider. Spectroscopic manifestations of the kondo effect on single adatoms. *Journal of Physics: Condensed Matter*, **21** (2009).
- [65] A. Mugarza, C. Krull, R. Robles, S. Stepanow, G. Ceballos and P. Gambardella. Spin coupling and relaxation inside molecule-metal contacts. *Nature Communications*, **2** (2011).
- [66] P. W. Anderson. Localized magnetic states in metals. *Physical Review*, **124**, pp. 41–53 (1961).
- [67] L. I. Mandelshtam and I. E. Tamm. The uncertainty relation between energy and time in nonrelativistic quantum mechanics. *Izv. Akad. Nauk SSSR*, **9**, p. 122–128 (1945).
- [68] A. C. Hewson. *The Kondo Problem to Heavy Fermions*. Cambridge University Press (1993).

Bibliography

- [69] O. Újsághy, J. Kroha, L. Szunyogh and A. Zawadowski. Theory of the fano resonance in the stm tunneling density of states due to a single kondo impurity. *Physical Review Letters*, **85**, pp. 2557–2560 (2000).
- [70] U. Fano. Effects of configuration interaction on intensities and phase shifts. *Physical Review*, **124**, pp. 1866–1878 (1961).
- [71] H. O. Frota and L. N. Oliveira. Photoemission spectroscopy for the spin-degenerate anderson model. *Physical Review B*, **33**, pp. 7871–7874 (1986).
- [72] J. H. Osiecki and E. F. Ullman. Studies of free radicals - alpha-nitronyl nitroxides, a new class of stable radicals. *Journal of the American Chemical Society*, **90**, pp. 1078–1079 (1968).
- [73] M. Tamura, Y. Nakazawa, D. Shiomi, K. Nozawa, Y. Hosokoshi, M. Ishikawa, M. Takahashi and M. Kinoshita. Bulk ferromagnetism in the [beta]-phase crystal of the p-nitrophenyl nitronyl nitroxide radical. *Chemical Physics Letters*, **186**, pp. 401 – 404 (1991).
- [74] S. Kahle. Magnetic properties of individual molecule. *PhD Thesis. University of Konstanz* (2013).
- [75] N. Knorr, M. A. Schneider, L. Diekhöner, P. Wahl and K. Kern. Kondo effect of single co adatoms on cu surfaces. *Physical Review Letters*, **88**, p. 096804 (2002).
- [76] C. Stroh, M. Mayor and C. von Hänisch. Suzuki reactions with stable organic radicals – synthesis of biphenyls substituted with nitronyl-nitroxide radicals. *European Journal of Organic Chemistry*, **17**, pp. 3697–3703 (2005).
- [77] O. Pietzsch, A. Kubetzka, M. Bode and R. Wiesendanger. Spin-polarized scanning tunneling spectroscopy of nanoscale cobalt islands on cu(111). *Physical Review Letters*, **92**, p. 057202 (2004).
- [78] R. Wiesendanger. Spin mapping at the nanoscale and atomic scale. *Rev. Mod. Phys.*, **81**, pp. 1495–1550 (2009).
- [79] L. Diekhöner, M. A. Schneider, A. N. Baranov, V. S. Stepanyuk, P. Bruno and K. Kern. Surface states of cobalt nanoislands on cu(111). *Physical Review Letters*, **90**, p. 23608 (2003).
- [80] T. Umbach, I. Fernandez-Torrente, M. Ruby and K. Franke. Atypical charge redistribution over a charge-transfer monolayer on a metal. *New Journal of Physics*, **15**, pp. 083048–1–083048–9 (2013).

- [81] J. Hihath, C. Bruot, H. Nakamura, Y. Asai, I. Díez-Pérez, Y. Lee, L. Yu and N. Tao. Inelastic transport and low-bias rectification in a single-molecule diode. *ACS Nano*, **5**, pp. 8331–8339 (2011).
- [82] A. F. Otte, M. Ternes, S. Loth, C. P. Lutz, C. F. Hirjibehedin and A. J. Heinrich. Spin excitations of a kondo-screened atom coupled to a second magnetic atom. *Phys. Rev. Lett.*, **103**, p. 107203 (2009).
- [83] Y.-S. Fu, Q.-K. Xue and R. Wiesendanger. Spin-resolved splitting of kondo resonances in the presence of rky-type coupling. *Phys. Rev. Lett.*, **108**, p. 087203 (2012).
- [84] J.-F. Lutz, M. Ouchi, M. Sawamoto and T. Y. Meyer, editors. *Sequence-Controlled Polymers: Synthesis, Self-Assembly, and Properties*. American Chemical Society (2014).
- [85] J.-F. Lutz, M. Ouchi, D. R. Liu and M. Sawamoto. Sequence-controlled polymers. *Science*, **341** (2013).
- [86] V. H. Wysocki, K. A. Resing, Q. Zhang and G. Cheng. Mass spectrometry of peptides and proteins. *Methods*, **35**, pp. 211–222 (2005).
- [87] M. S. Lee and E. H. Kerns. Lc/ms applications in drug development. *Mass Spectrometry Reviews*, **18**, pp. 187–279 (1999).
- [88] B. D. Kasianowicz, Brandin. Characterization of individual polynucleotide molecules using a membrane channel. *Proceedings of the national academy of sciences of the united states of America*, **93**, pp. 13770–13773 (1996).
- [89] D. Zhong, J.-H. Franke, S. K. Podiyanachari, T. Blömker, H. Zhang, G. Kehr, G. Erker, H. Fuchs and L. Chi. Linear alkane polymerization on a gold surface. *Science*, **334** (2011).
- [90] R. G. Endres, D. L. Cox and R. R. P. Singh. *Colloquium*: The quest for high-conductance dna. *Rev. Mod. Phys.*, **76**, pp. 195–2014 (2004).
- [91] J. Repp, G. Meyer, S. M. Stojković, A. Gourdon and C. Joachim. Molecules on insulating films: Scanning-tunneling microscopy imaging of individual molecular orbitals. *Physical Review Letters*, **94**, p. 026803 (2005).
- [92] P. Liljeroth, J. Repp and G. Meyer. Current-induced hydrogen tautomerization and conductance switching of naphthalocyanine molecules. *Science*, **317** (2007).
- [93] T. T. Trinh, L. Oswald, D. Chan-Seng and J.-F. Lutz. Synthesis of molecularly encoded oligomers using a chemoselective “ab + cd” iterative approach. *Macromolecular Rapid Communications*, **35**, pp. 141–145 (2014).

Bibliography

- [94] S. Rauschenbach, F. L. Stadler, E. Lunedei, N. Malinowski, S. Koltsov, G. Costantini and K. Kern. Electro spray ion beam deposition of clusters and biomolecules. *Small*, **2**, pp. 540–547 (2006).
- [95] M. Pauly, M. Sroka, J. Reiss, G. Rinke, A. Albarghash, R. Vogelgesang, H. Hahne, B. Kuster, J. Sesterhenn, K. Kern and S. Rauschenbach. A hydrodynamically optimized nano-electrospray ionization source and vacuum interface. *Analyst*, **139**, pp. 1856–1867 (2014).
- [96] R. Seymour and C. Carraher. *Polymer chemistry*. CRC Press (2007).
- [97] L. Bartels, G. Meyer and K.-H. Rieder. Controlled vertical manipulation of single co molecules with the scanning tunneling microscope: A route to chemical contrast. *Applied Physics Letters*, p. 213 (1997).
- [98] P. Wahl. Local spectroscopy of correlated electron systems at metal surfaces. *PhD Thesis. University of Konstanz* (2005).
- [99] S. Sachdev. Quantum criticality: Competing ground states in low dimensions. *Science*, **288** (2000).
- [100] M. Vojta. Quantum phase transitions. *Reports on Progress in Physics*, **66**, p. 2069 (2003).
- [101] B. A. Jones, C. M. Varma and J. W. Wilkins. Low-temperature properties of the two-impurity kondo hamiltonian. *Physical Review Letters*, **61**, pp. 125–128 (1988).
- [102] N. J. Craig, J. M. Taylor, E. A. Lester, C. M. Marcus, M. P. Hanson and A. C. Gossard. Tunable nonlocal spin control in a coupled-quantum dot system. *Science*, **304**.
- [103] H. Jeong, A. M. Chang and M. R. Melloch. The kondo effect in an artificial quantum dot molecule. *Science*, **293** (2001).
- [104] J. Bork, Y.-h. Zhang, L. Diekhoner, L. Borda, P. Simon, J. Kroha, P. Wahl and K. Kern. A tunable two-impurity Kondo system in an atomic point contact. *Nature Physics*, **7**, pp. 901–906 (2011).
- [105] H. Prueser, P. E. Dargel, M. Bouhassoune, R. G. Ulbrich, T. Pruschke, S. Lounis and M. Wenderoth. Interplay between the Kondo effect and the Ruderman-Kittel-Kasuya-Yosida interaction. *Nature Communications*, **5** (2014).
- [106] E. Sela and I. Affleck. Nonequilibrium transport through double quantum dots: Exact results near a quantum critical point. *Physical Review Letters*, **102**, p. 047201 (2009).
- [107] A. Georges and Y. Meir. Electronic correlations in transport through coupled quantum dots. *Physical Review Letters*, **82**, pp. 3508–3511 (1999).

Acknowledgments

This thesis would have not been done in the way it is without contribution of many people, whom I want to acknowledge for their help and support:

- Prof. Klaus Kern, for giving me an opportunity to pursue my PhD under his supervision and to work in his lab on very exciting topics.
- Prof. Cécile Hébert for charing the exam, Prof. Jean-Philippe Ansermet, Prof. Peter Wahl and Prof. Jean-François Lutz for becoming part of the thesis committee.
- Dr. Uta Schlickum for supervising this thesis and her activities as group leader of the 4K STM.
- Dr. Stephan Rauschenbach for his personal support, inspiration and very interesting projects done together.
- Dr. Markus Ternes for his technical and scientific expertise, exciting discussions on shot noise and Kondo effect.
- Dr. Bogdana Borca for always being helpful, good working atmosphere and unforgettable time in the lab.
- Verena Schendel for being my good colleague and productive collaboration during 4 years.
- Dr. Rico Gutzler and Dr. Ludger Hanau for DFT/molecular dynamics calculations and fruitful scientific discussions.
- Technical team of the Kern department for their help and expertise: Wolfgang Stiepany, Peter Andler, Marco Memmler, Rafail Chaikévitch and Martin Siemers.
- All current and former members of the institute for the nice atmosphere and support during the last 4 years : Christian Dette, Sabine Abb, Matthias Muenks, Dr. Mostafa Enayat, Ramakrishna Aluru, Berthold Jäck, Dr. Tobias Herden, Dr. Carola Straßler,

Chapter 5. Acknowledgments

Christoph Große, Alex Hoyer, Dr. Pablo Merino, Jacob Senkpiel, Anna Roslawska, Tomasz Michnowicz, Dr. Doris Grumelli, Dr. Eva Pensa, Dr. Thomas White, Dr. Gordon Rinke, Dr. Sebastian Stepanow, Claudius Morchutt, Diana Hötger.

- Last but not least, I would like to thank my family and Anna for their understanding and encouragement.

Curriculum Vitae

Name: Ivan Pentegov
Date of birth: 20.10.1987
Nationality: Russian

2015 PhD Thesis: "*Local electronic properties and adsorption conformations of molecular nanostructures at surfaces*", EPF Lausanne, Switzerland. Thesis director: Prof. Klaus Kern.

2011-2015 Research Assistant in the Nanoscale Science Group at the Max-Planck-Institute for Solid State Research, Stuttgart, Germany.

2005-2011 Diploma studies in physics at the Moscow State Lomonosov University. Graduation with honors.

